IVW - Schriftenreihe Band 20

Institut für Verbundwerkstoffe GmbH - Kaiserslautern

Marc R. S. Huisman

Experimental and numerical investigations for the prediction of the crashworthiness of layered quasi-isotropic thermoplastic composites

Die Deutsche Bibliothek – CIP-Einheitsaufnahme

Experimental and numerical investigations for the prediction of the crashworthiness of layered quasi-isotropic thermoplastic composites / Marc R. S. Huisman. – Kaiserslautern : IVW, 2001
(IVW-Schriftenreihe ; Bd. 20)
Zugl.: Kaiserslautern, Univ., Diss., 2001
ISBN 3-934930-16-6

Herausgeber: Institut für Verbundwerkstoffe GmbH
Erwin-Schrödinger-Straße
Universität Kaiserslautern, Gebäude 58
67663 Kaiserslautern

Verlag: Institut für Verbundwerkstoffe GmbH

Druck: Universität Kaiserslautern
ZBT – Abteilung Foto-Repro-Druck

D-386

Als Manuskript gedruckt. Printed in Germany.

ISSN 1615-021X
ISBN 3-934930-16-6

Experimental and numerical investigations for the prediction of the crashworthiness of layered quasi-isotropic thermoplastic composites

Vom Fachbereich Maschinenbau und Verfahrenstechnik
der Universität Kaiserslautern
zur Verleihung des akademischen Grades

Doktor-Ingenieur (Dr.-Ing.)

genehmigte Dissertation

vorgelegt von
Ir. Marc R.S. Huisman
aus Zevenaar (NL)

D 386

Prüfungsvorsitz:	Prof. Dr.-Ing. Steinmann
Referent:	Prof. Dr.-Ing. Maier
Koreferent:	Prof. Dr.-Ing. Schweizerhof

Tag der mündlichen Prüfung: 10.05.2001

Preface

This thesis has been written between 1995 and 2001 during my work period as research associate at the Institut für Verbundwerkstoffe GmbH (Institute for Composite Materials) in Kaiserslautern, Germany.

I owe special thanks to Prof. Dr.-Ing. M. Maier for his support of this work and also for his responsibility as reviewer. I also thank Prof. Dr.-Ing. K. Schweizerhof for his critical comments as co-reviewer and Prof. Dr.-Ing. P. Steinmann for his chairmanship of the board of examiners.

Furthermore, I would like to thank all my colleagues at IVW GmbH who contributed to this thesis. Especially A. Dehn for his time and comments in the many discussions we had.

Maastricht, July 2001 Marc Huisman

Contents

Zusammenfassung

In der vorliegenden Arbeit wird das Verhalten von thermoplastischen Verbundwerkstoffen mittels experimentellen und numerischen Untersuchungen betrachtet. Das Ziel dieser Untersuchungen ist die Identifikation und Quantifikation des Versagensverhaltens und der Energieabsorptionsmechanismen von geschichteten, quasi-isotropen thermoplastischen Faser-Kunststoff-Verbunden und die Umsetzung der gewonnenen Einsichten in Eigenschaften und Verhalten eines Materialmodells zur Vorhersage des Crash-Verhaltens dieser Werkstoffe in transienten Analysen.
Vertreter der untersuchten Klassen sind un- und mittel-vertreckte Rundgestricke und glasfaserverstärkte Thermoplaste (GMT). Die Untersuchungen an rundgestrickten glasfaser-(GF)-verstärktem Polyethylentherephthalat (PET) waren Teil eines Forschungsprojektes zur Charakterisierung sowohl der Verarbeitbarkeit als auch des mechanischen Verhaltens. Experimente an GMT und Schnittfaser-GMT wurden ebenfalls zum Vergleich mit dem Gestrick durchgeführt und dienen als Bestätigung des beobachteten Verhaltens des Gestrickes.
Besonderer Aufmerksamkeit wird der Einfluß der Probengeometrie auf die Resultate gewidmet, weil die Crash-Charakteristiken wesentlich von der Geometrie des getesteten Probekörpers abhängen. Hierzu wurde ein Rundhutprofil zur Untersuchung dieses Einflußes definiert. Diese spezielle Geometrie hat insbesondere Vorteile hinsichtlich Energieabsorptionsvermögen sowie Herstellbarkeit von thermoplastischen Verbundwerkstoffen (TPCs). Es wurden Impakt- und Perforationsversuche zur Untersuchung der Schädigungsausbreitung und zur Charakterisierung der Zähigkeit der untersuchten Materialien durchgeführt.
Geschichtete TPCs versagen hauptsächlich in einem Laminat-Biegemodus mit kombiniertem intra- und interlaminaren Schub (transversaler Schub zwischen Lagen und teilweise mit transversalen Schubbrüchen in einzelnen Lagen). Durch eine Kopplung der aktuellen Versagensmodi und Crash-Kennwerten wie der mittleren Crash-Spannung, konnten Indikationen über die Relation zwischen Materialparameter und absoluter Energieabsorption gewonnen werden.
Numerische Untersuchungen wurden mit einem expliziten Finiten Elemente-Programm zur Simulation von dreidimensionalen, großen Verformungen durchgeführt. Das Modell besteht bezüglich des Querschnittaufbaus aus einer mesoskopischen Darstellung, die zwischen Matrix-zwischenlagen und mesoskopischen

Verbundwerkstofflagen unterscheidet. Die Modellgeometrie stellt einen vereinfachten Längsquerschnitt durch den Probekörper dar. Dabei wurden Einflüsse der Reibung zwischen Impaktor und Material sowie zwischen einzelnen Lagen berücksichtigt. Auch die lokal herrschende Dehnrate, Energie und Spannungs-Dehnungsverteilung über die mesoskopischen Phasen konnten beobachtet werden. Dieses Modell zeigt deutlich die verschiedenen Effekte, die durch den heterogenen Charakter des Laminats entstehen, und gibt auch Hinweise für einige Erklärungen dieser Effekte.

Basierend auf den Resultaten der obengenannten Untersuchungen wurde ein phänomenologisches Modell mit a-priori Information des inherenten Materialverhaltens vorgeschlagen. Daher, daß das Crashverhalten vom heterogenen Charakter des Werkstoffes dominiert wird, werden im Modell die Phasen separat betrachtet. Eine einfache Methode zur Bestimmung der mesoskopischen Eigenschaften wird diskutiert.

Zur Beschreibung des Verhaltens vom thermoplastischen Matrixsystem während „Crushing“ würde ein dehnraten- und temperaturabhängiges Plastizitätsgesetz ausreichen. Für die Beschreibung des Verhaltens der Verbundwerkstoffschichten wird eine gekoppelte Plastizitäts- und Schädigungsformulierung vorgeschlagen. Ein solches Modell kann sowohl den plastischen Anteil des Matrixsystems als auch das „Softening“ - verursacht durch Faser-Matrix-Grenzflächenversagen und Faserbrüche - beschreiben. Das vorgeschlagene Modell unterscheidet zwischen Belastungsfällen für axiales „Crushing“ und Versagen ohne „Crushing“. Diese Unterteilung ermöglicht eine explizite Modellierung des Werkstoffes unter Berücksichtigung des spezifischen Materialzustandes und der Geometrie für den außerordentlichen Belastungsfall, der zum progressiven Versagen führt.

Notation and Symbols

Notational conventions

Notation	Description
a_{xy}	Indices corresponding to directions xy, ij respectively wale-course directions for knitted fabrics
$a_{c,t}$	Indices corresponding to compression, tension
a^n	Parameter at time n
$\mathbf{a}$	Tensor
a	Scalar
$\underline{a}$	Vector
$\underline{\underline{a}}$	Matrix
$\dot{a}$	First time derivative of a
$\ddot{a}$	Second time derivative of a

Symbols

Symbol	Unit	Description
ρ	g/cm^3	Mass Density
E	MPa	Young's modulus
G	MPa	Shear modulus
ν	1	Poisson's ratio
σ	MPa	True stress
$\hat{\sigma}=(1-D)^{-1}\sigma$	MPa	Effective stress
ε	1	Strain
R_{iit}	MPa	Tensile strength in i-direction
R_{iic}	MPa	Compressive strength in i-direction
R_{ij}	MPa	Shear strength in ij-plane
D	1	Damage operator
ω	-	Damage function
σ_u	MPa	Matrix ultimate strength
ε_u	1	Matrix ultimate strain

σ_y	MPa	Matrix yield stress
E_{abs}	J	Absorbed energy
E_s	J/g	Mass specific absorbed energy
σ_s	MPa	Sustained crush stress
σ_{ss}	MPa	Specific sustained crush stress
AE	1	Crush force efficiency
L.U.	1	Load uniformity
S_e	1	Stroke efficiency
F_m	N	Mean crush force
F_{peak}, F_{max}	N	Force at first peak
x_{peak}	mm	Displacement at force peak
x_{max}	mm	Maximum displacement
F_m	N	Mean crush force
A_0	mm^2	Original cross-section
A_f	mm^2	Original cross-section of the flange of a crash element
L_0	mm	Original length of a crash element
ε_T	1	Transmitted longitudinal strain wave
ε_I	1	Compressive longitudinal strain wave
ε_R	1	Reflected longitudinal strain wave
v_I	m/s	Projectile impact velocity
c_0	m/s	Speed of sound in a material
K	%	Crystallinity degree
T_k	K	Temperature in Kelvin
T	ºC	Temperature in degree Celsius
T_g	ºC	Glass transition temperature
T_m	ºC	Crystallite melt temperature
ϕ_m	mW	Heat flow rate
θ	°	Fibre orientation angle
φ_f	1	Fibre volume fraction
ψ_f	1	Fibre weigth fraction
$\lambda_{w,c}$	1	Prestretching degree in wale and course direction

		respectively
$\rho_{w,c}$	1/mm	Linear loop density in wale and course direction respectively
t_i	mm	Thickness of i
w_i	mm	Width of i
D_{imp}	mm	Impactor diameter
F_{peak}	N	Force at first peak
E_i	J	Initiation energy, energy at peak force
E_{prop}	J	Propagation energy
E_{tot}	J	Total dissipated energy
E'_i	J	Normalized initiation energy
E'_{tot}	J	Normalized total dissipated energy
DI	1	Ductility index
β	1	Johnson-Cook proportionality coefficient
c	1	Proportionality coefficient

Abbreviation	Description
CLT	Classical Laminate Theory
FRP	Fibre Reinforced Plastic
TPC	Thermoplastic Composite
KFRP	Knitted Fibre Reinforced Plastic
WFRP	Woven Fibre Reinforced Plastic
SFRP	Short Fibre Reinforced Plastic
GMT	Glass Mat reinforced Thermoplastic
SMC	Sheet Moulding Compound
GF	Glass Fibre
AF	Aramide Fibre
CF	Carbon Fibre
UD	Unidirectional
MD	Multidirectional
TP	Thermoplastic
PA	Polyamide
PET	Polyethylene terephtalate
PC	Polycarbonate

PP	Polypropylene
PEEK	Polyetheretherketone
EP	Epoxy
VE	Vinylester
DSC	Differential scanning calorimetry
TG	Thermogravimetry
SHPB	Split-Hopkinson Pressure Bar

1 Introduction

1.1 Introduction and problem definition

The overall trend of lightweight cars demands the usage of new or enhanced materials. A class of these new materials are fibre-reinforced polymers (FRPs). Especially in the automotive industry numerical simulations serve within the design process of cars and car components to minimize the costly full scale crash tests. The numerical simulation of complex structures under dynamical loading made from these materials is also demanded in the increased usage of numerical tools.

However, the existing material models in common finite element codes to simulate 3D large deformations cannot predict the mechanical behaviour of crash-loaded FRPs sufficiently [32],[33],[54].

The reason for this situation is two-fold. First, the diversity of possible FRPs in crashworthiness applications is very large. It is not likely that one or two material models are able to predict the crashworthiness of all FRP-classes with their different macroscopic failure modes. Apart from the question of the classification, results of crashes are dominated by the strength behaviour of a FRP. Most failure criterions for the prediction of the strength of a FRP however, are restricted to unidirectional reinforcements. One should bear in mind that an UD-FRP is only one small class of possible FRPs. Also the matrix – thermoset or thermoplastic – influences the type of failure mode. No model exists that incorporates this distinction.

Second, the lack of knowledge in the quantitative relation between mechanical properties and behaviour of FRPs during a crash lead to material models for application in finite elements programs, which have non-physical parameters and thus cannot predict the crashworthiness without verification with the crash tests that one wants to simulate. A frequently occurring failure mode is lamina bending with central delamination, inter- and translaminar shear cracks and frictional effects, which are characteristic for the crashworthiness of most FRPs. The geometric deformation behaviour can principally not be represented with common 2D shell elements.

The lack of knowledge of the material behaviour lead to relative simple models, which do not satisfy the momentary simulation demands. Here, one should ask if the present relation between simulation accuracy and computing time is justified.

1.2 Objective and methodology of the present research

The objective of the present research is two-fold:

1. Gain insight in the failure and energy absorption mechanisms of thermoplastic composites to identify a quantitative relation between the principle mechanical material behaviour and structural crashworthiness,
2. Translate this knowledge into material model properties for the numerical prediction of crash response.

In order to achieve the first objective, experimental investigations are performed on materials from a representative class of thermoplastic composites. The chosen class is defined as layered quasi-isotropic TPCs. A laminate is called isotropic, if the structure behaves isotropic under in-plane extension [72]. In this thesis, the isotropic group of materials is extended to quasi-isotropy by the inclusion of orthotropic materials, which show relatively small deviations from the ideal isotropic case, see Figure 1.

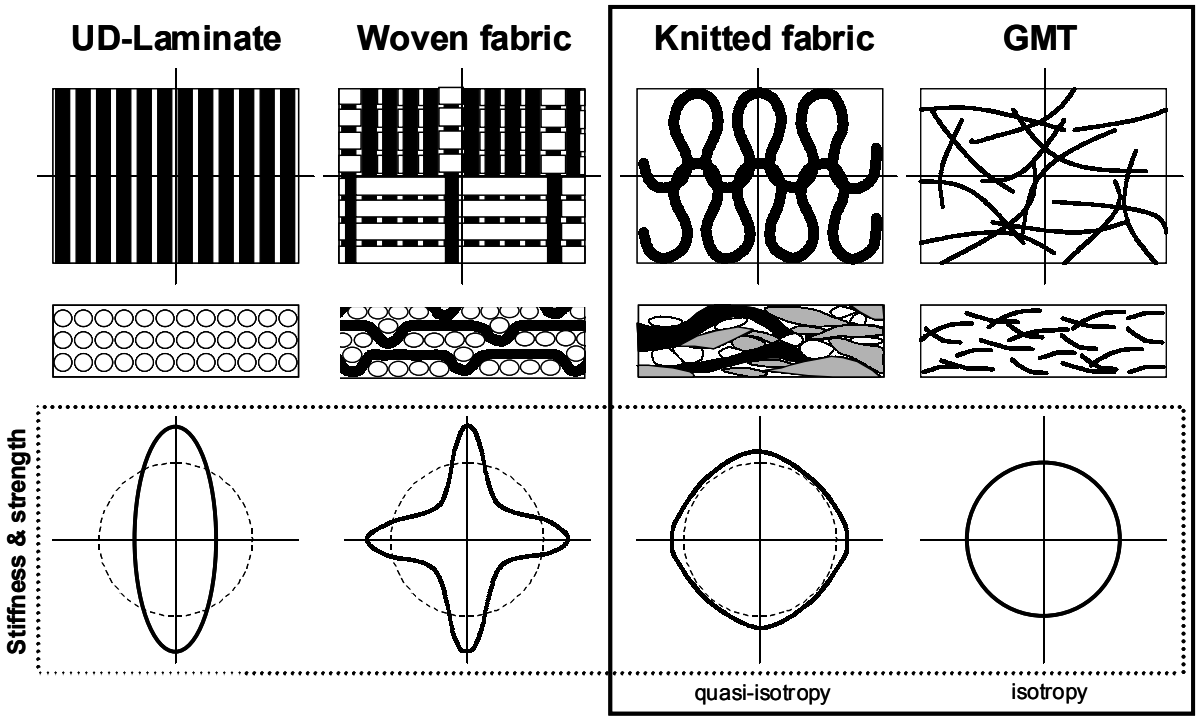

Figure 1: Classes of TPCS with different degrees of anisotropy

Utilization of continuous fibre reinforced composites in industrial applications is restricted by the price of the reinforcement and the limited shaping of a product. The lightweight structure advantages of these composites versus metals do not have the same ratio concerning costs. Knitted fibre reinforced polymers (KFRPs) offer versatile deployment possibilities due to structure specific properties like i.e. good drapability,

high damage tolerance and acceptable mechanical properties in combination with acceptable manufacturing effort. Therefore, weft knitted glass fibre reinforced glass fibre (GF) reinforced polyethylene terephthalate (PET) is chosen as representative material.

Random glass mat reinforced polymers (GMT) belong to a material group, which dominates mass production and cost-efficient materials. Typical applications of GMT with crashworthiness relevance are car frond-end, bumper beam, crash box or structural elements between longitudinal girder and bumper beam.

This last group is used to demonstrate the generalization potential of the identified failure mechanisms and other governing effects for KFRPs to general layered quasi-isotropic thermoplastic composites.

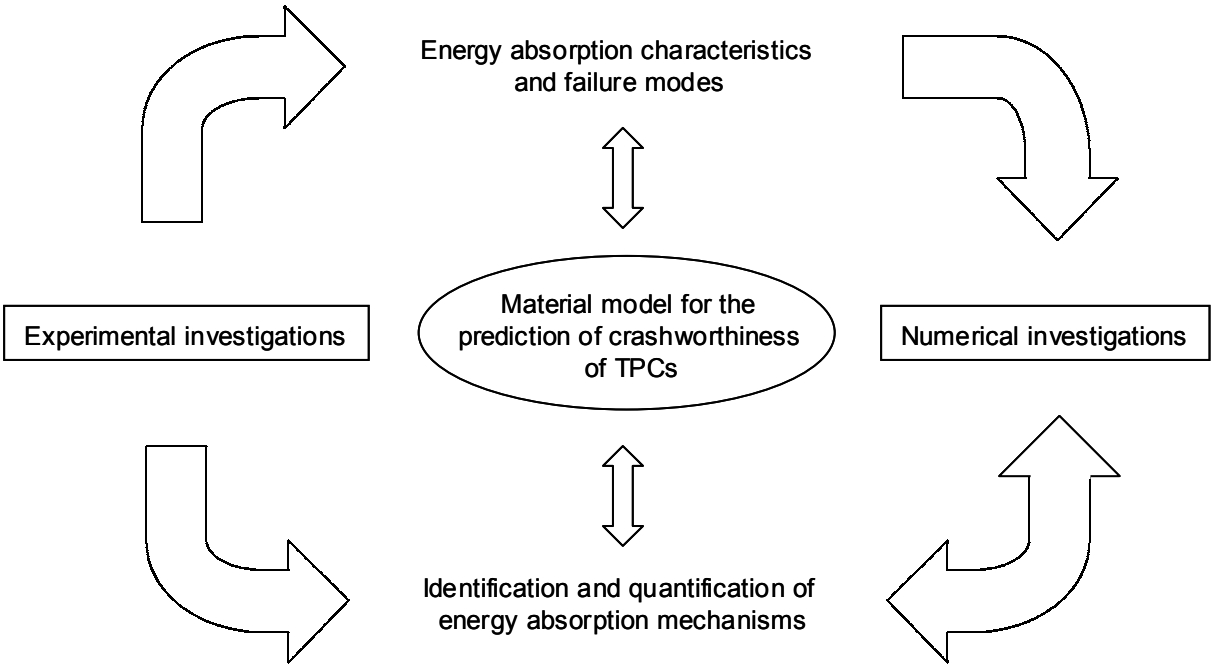

Figure 2: Structure of the present research

The performed experimental investigations serve to characterize the failure behaviour in energy absorption characteristics and failure modes. Based on the quasi-static and dynamic experimental results, a relation between crash characteristics, failure behaviour and properties is identified to create a validated material model to be used in numerical simulations (Figure 2).

A mesoscopic FE-model consisting of homogenized composite layers and matrix interplies serves to investigate and quantify the influence of the heterogeneity on the

energy absorption. Stress-strain distribution, force flow as well as delamination and frictional effects are investigated with this model.

The obtained information of both experiments and numerical simulations serves to choose and formulate a macroscopic material model with a priori material information for the prediction of the crashworthiness behaviour. Important features of the proposed material model are discussed concerning a proper prediction of energy absorption and mesoscopic stress-strain behaviour. Implementation and testing of the material model in a FE-code is not discussed since this would exceed the scope of the investigations. The proposed model requires at least the necessity to implement new elements and another method of identification of the crash front with varying through-the-thickness properties.

1.3 State of the art

1.3.1 Fundamentals of crashworthiness of fibre reinforced polymers

The crash behaviour of fibre reinforced polymers (FRP) is substantially different compared to metallic materials. Metals fail in a folding or local buckling mode, with plastic deformation occurs only in areas of major local bending. FRP almost fully fail by micro- and macro-mechanical fracture processes. The performance of FRP in terms of structural crashworthiness can be expressed by several phenomenological properties, such as the mass specific energy absorption or the sustained crush stress. Such crashworthiness characteristics are defined based upon the response of a tested component. A typical force-deflection diagram of a FRP can be divided into 3 phases (Figure 3) [34],[50]:

I Initiation phase: the initiation phase occurs in the area of initial contact between the impactor and the specimen and the first load peak F_{peak}. Here, the impactor damages the so-called trigger. This trigger is an inclination or a continuous reduction of the cross-section of the specimen, which initiates the beginning of crushing at a locally defined area and concludes in progressive crushing of the crash element.

II Main crush phase: the main crush phase lies between x_{peak} and x_{max}. The impactor contacts the full cross-section and the specimen is progressively damaged (progressive failure) by stable crushing or folding until the kinetic energy of the impactor is fully absorbed.

III Energy release phase: the non-failed part of the specimen returns it's elastic energy in a relaxation of deformation during the energy release phase.

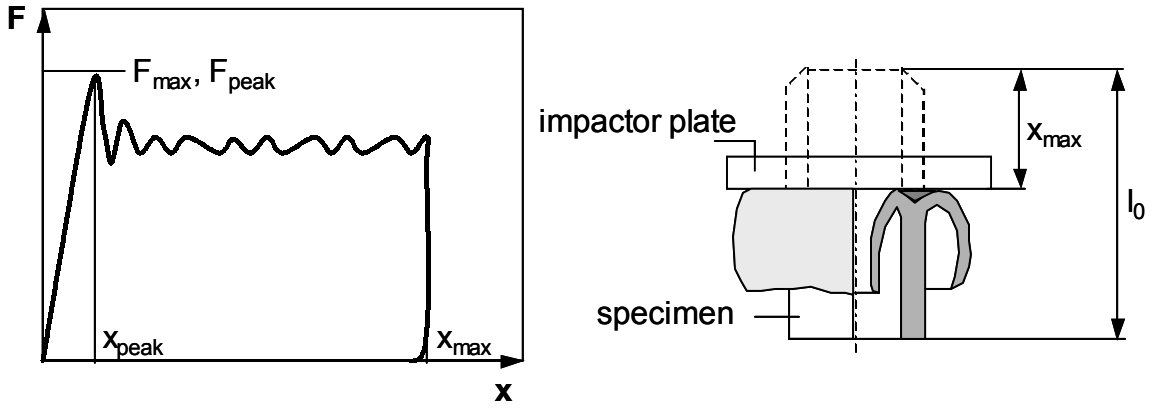

Figure 3: Force-deflection diagram and definition of force- and length-parameters for fibre reinforced polymer structures

The properties derived from this force-displacement diagram should be able to characterize and compare the energy absorption capability of FRP with other materials or structures. Thus, apart from absolute values, some specific properties are defined (Table 1).

Table 1: Crashworthiness characteristics to rate the energy absorption capability

Property	**Symbol**	**Unit**	**Determination**
Mean crush force	F_m	[N]	E_{abs} / x_{max}
Absorbed energy	E_{abs}	[J]	$_0\int^x F dx$
Specific energy absorption	E_s	[J/g]	$E_{abs} \cdot l_0 / (x_{max} \cdot M)$
Sustained crush stress	σ_s	[MPa]	F_m / A_0
Specific sustained crush stress	σ_{ss}	[J/g]	σ_s / ρ
Stroke or crush force efficiency	$S_e = AE$	[1]	F_m / F_{max}
Load uniformity	$LU = \frac{1}{AE}$	[1]	F_{max} / F_m

The most common characteristics concerning crashworthiness in the investigation of materials are the specific energy absorption, mean crush force and sustained crush stress. However, the mean force depends on the cross-section and the geometry of the respective tested component and is only usable for structures with constant geometries. By using the sustained crush stress, this disadvantage of variable cross-sections is overcome.

The specific absorbed energy is the absorbed energy divided by the crushed mass of the tested component. The sustained crush stress is the mean force divided by the component cross-section area. Thus, the specific absorbed energy is a mass specific property whereas the sustained crush stress is an area specific property.

Peak and maximum force values depend on test rig and measurement system properties and are thus qualitative and not quantitative properties. This is also valuable for crashworthiness properties, which are derived from this peak force, e.g. load uniformity and stroke efficiency.

The crashworthiness potential of thermoplastic composites (TPC) can easily be compared with the mass specific absorbed energy. The investigated knitted fabric for example, is positioned between random oriented composites like SMC and GMT and

oriented composites like woven fabrics (Figure 4). All elements consisted of half shells connected by the same joining technique, i.e. riveting.

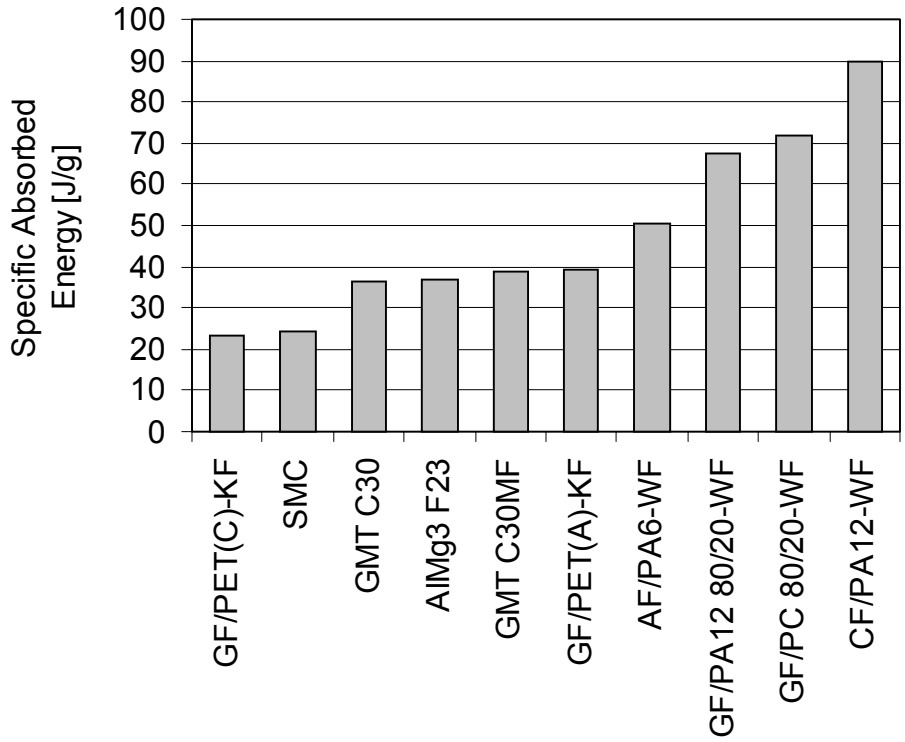

Figure 4: Specific absorbed energy for Aluminium and several composite materials (Abbreviations in Appendix 8.1, Table 19)

The failure behaviour of FRP can be described by the governing failure modes and mechanisms. Dependent on the separate components of the composite, matrix and fibre, and their distribution in the laminate, several failure mechanisms can occur. Most fibre reinforced polymers fail by one of three modes - or a combination of these modes - [36]:

I: Lamina bending,

II: Transverse shearing, and

III: Local buckling.

The division into these crushing modes are based upon crash tests on thermoset composites with oriented continuous fibres [34],[36],[39],[40]. Materials with other reinforcement or matrix systems fail by similar macroscopic modes, but on a microscopic level, with more complex failure mechanisms. Figure 5 shows typical macroscopic modes for thermoplastic composites.

(I) (II) (III)

Figure 5: Schematic diagram of macroscopic failure modes: lamina bending (I), transverse shearing (II) and progressive or local buckling (III)

From the energy absorption point of view, principle sources of energy dissipation for the governing failure modes are matrix deformation and cracking, fibre cracking, fibre-matrix interface failure and friction. These microscopic mechanisms are part of all failure modes but differ in magnitude and are indirectly represented by the different strengths of the composite.

The lamina bending mode (I) is characterized by delamination and bending of lamina due to the formation and growth of interlaminar and intralaminar cracks. The formation of longitudinal cracks in the outer laminae is based on a tensile load due to change in radius. These cracks generally are longitudinal but can also be parallel to the fibre bundles for small values of the fibre orientation θ (Figure 6).

The transverse shearing mode can be divided into two sub-modes based on the direction of the cracks. Mode II-a is dominated by the formation and growth of longitudinal cracks while mode II-b is dominated by translaminar cracks. Both sub-modes have a wedge-shaped cross-section at the crushing zone.

The progressive local buckling mode (III) can be compared with buckling and folding for ductile metals. In addition to the plastic deformation interlaminar cracks and fibre cracks at the tensile loaded side of a buckle dominate this failure mode (Figure 6).

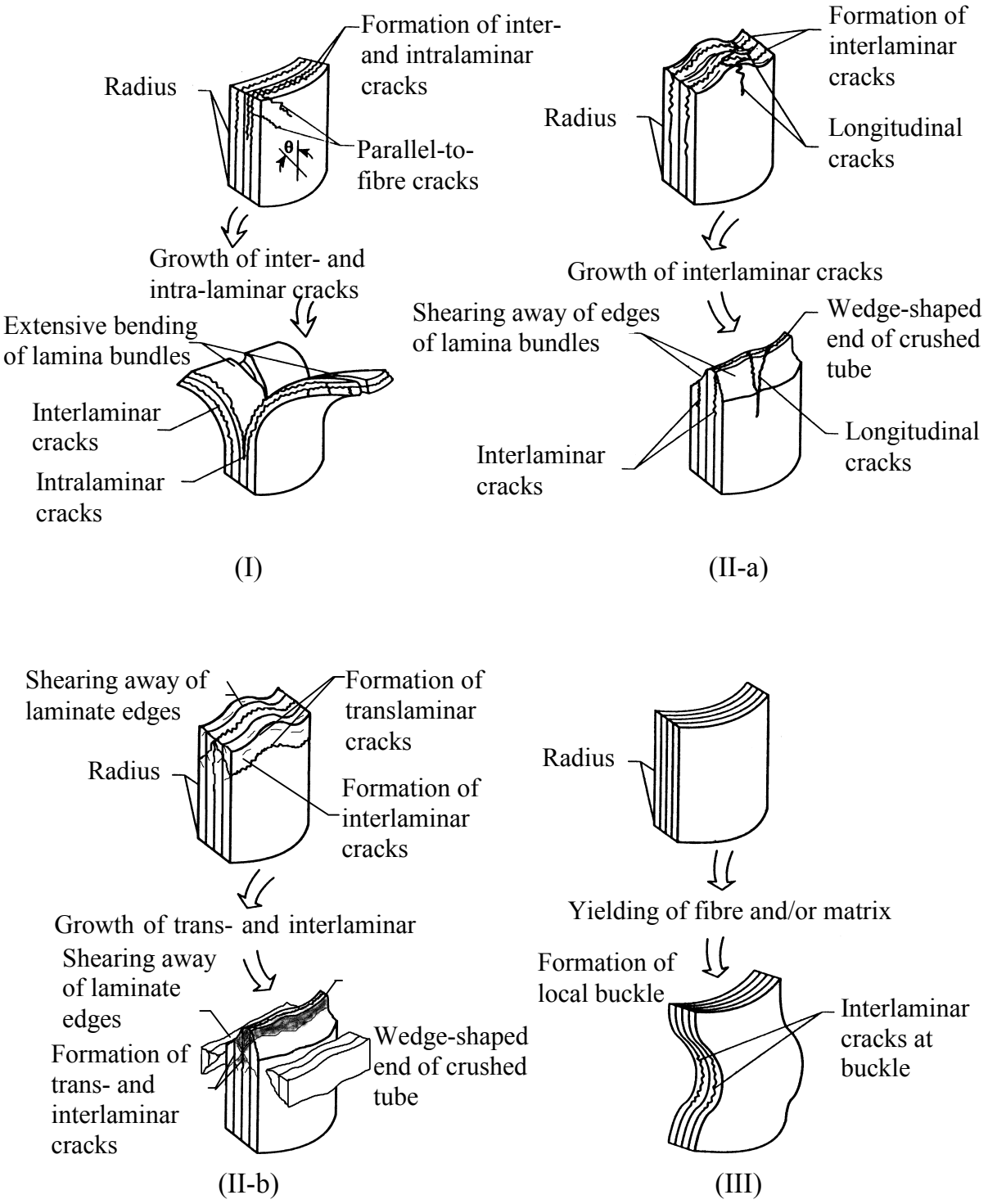

Figure 6: Failure mechanisms of the failure modes of FRP for lamina bending (I), transverse shearing (II-a,b), local buckling crushing mode (III)

1.3.2 Material models and numerical simulation of crash-loaded composites

The present-day material models in explicit finite element codes for the simulation of the mechanical behaviour of FRPs are mostly based on the classical laminate theory (CLT) [92] for the description of multilayered unidirectional reinforced composites. These CLT-models are extended with failure criteria to determine the location and onset of failure or the utility degree of FRP-components. However, for crash loading the material behaviour beyond failure mainly determines the quantitative crash response. First models - 2D and 3D - that took into account the post-failure behaviour were developed for filament wound GF/VE tubes as part of a joint research project [50],[51]. The 2D-model is a so-called crush-front model with stacked laminae based on the CLT and is bounded by a Chang-Chang [83],[82] or modified Tsai-Wu [81] failure criterion with determination of different failure modes. This model identifies four separate failure modes [52]:

I: Fibre tension
II: Fibre compression
III: Matrix tension
IV: Matrix compression

The governing failure mode specifies the modifications in the stiffness and strength constants in the post-failure region. Elements neighbouring eroded or failed elements are identified as crush front elements and are predamaged by a softening factor for the compressive strength. This approach enables progressive failure of uni-axial crushing.

A model for anisotropic damage to describe the elastic-brittle behaviour of unidirectional FRPs is developed by Matzenmiller et al. [48]. This model describes the damage as a smooth function of the strain with a typical softening behaviour for the post-strength region. However, the softening behaviour is not suitable for FRPs under compressive or crash loading. Schweizerhof et al. [54],[55] presented modifications and enhancements of both 2D crush-front models. The modifications mainly concern the failure and erosion criteria as well as the introduction of the crush strength for the composite damage model with a constant post-failure stress level.

The 3D-model was originally developed for crushing and later extended and modified for simulation of impact [56],[57],[50],[51]. This model covers the elastic anisotropic damage behaviour of composites, material failure with different failure modes and the description of the completely damaged or crushed material. Failure is detected by the 3D Tsai-Wu criterion with quadratic interaction terms. Normalized stress components determine the governing failure or damage mode with the following possible cases:

I: Fibre failure in tension or compression
II: In-plane matrix failure in tension or compression
III: Transverse matrix failure in tension or compression
IV-VI: Shear failure in three different planes

Also included is a switch to isotropic behaviour for disrupted, crushed material under compressive loading. This is achieved by modifications of the failure surface.

Another type of material model for crash-loaded FRPs is the so-called Bi-Phase model. This model and some models derived from the Bi-Phase model are discussed in [58], [59]. Within the Bi-Phase model, the matrix and fibre properties are treated separately. From the orthotropic elastic properties of a unidirectional ply and known fibre properties, the elastic matrix properties are deduced. A damage fracture law is available for modulus damage. The used isotropic law has a linear damage function and a strain-softening phase. The non-smooth damage function is divided into the following phases:

I: An initial linear region without permanent damage
II: A first damaging phase including a permanent and linearly varying stiffness reduction
III: A second damaging phase for a controlled unloading
IV: A fully damaged state

This is essentially nothing different from what is done else only with the name fragmentation to take into account damage and large deformations.

In general, independent of the FE-code used, a multi-layered composite can be modelled either by using two material phases, namely fibres and matrix, or by using one material phase, namely the matrix with orthotropic laminate properties. The first approach allows micro-mechanical 3D modelling of a UD ply or a simple laminate whereas the second approach uses the homogenized damage approach and allows more complex lay-ups with multiple layers or materials.

Studies to improve the FE capability to predict dynamic responses of composite crash absorbers resulted in a so-called enhanced composite material model for UDs and fabrics [60]. This model is basically similar to existing material models in other codes with changes in the formulation of the failure criterion. Here, dynamic sensitivity is accomplished by making the Tsai-Wu criterion and yield envelope strain rate dependent. One-element-tests generally show very good agreement with performed tension and compression tests. However, numerical simulations of crash-loaded components show poor agreement with the experimental counterparts due to the

complex crush behaviour controlled by friction and delamination that cannot be calculated with this model nor any model described above. This is documented in a critical review by Schweizerhof et al. [55]. The quasi-brittle behaviour of most FRPs cannot be modelled with the same quality as ductile FRPs, which fail in a buckling mode by yielding without extensive crushing.

1.3.3 Knitted fibre reinforced composites

Knitted fabrics form together with woven and braided fabrics the group of textile composites, which is generally classified by the textile forming techniques used for the reinforcement.

These materials are relevant for markets and products focussing on the combination of low costs with acceptable mechanical properties, low weight and corrosion tolerance. Application fields for glass fibre knitted fabrics are transport industry as well as aircraft and machining industry. Knitted carbon fibre structures were proposed for e.g. medical application in load bearing implants like bone plates [3], [24].

Knitted fabrics are characterised by their interlocking loops of yarns and can be divided into weft- and warp knitted fabric composites (Figure 7). The difference between both types lies in the method of knitting [1]. In the weft-knitted fabric, loops are formed by a single yarn, which runs in course direction (Figure 7, left). A warp-knitted fabric is formed by overlaps of alternative loops at alternate courses, which are produced with one yarn in wale direction. Depending on the type of warp knit, the yarn can cross one or more courses (Figure 7, right).

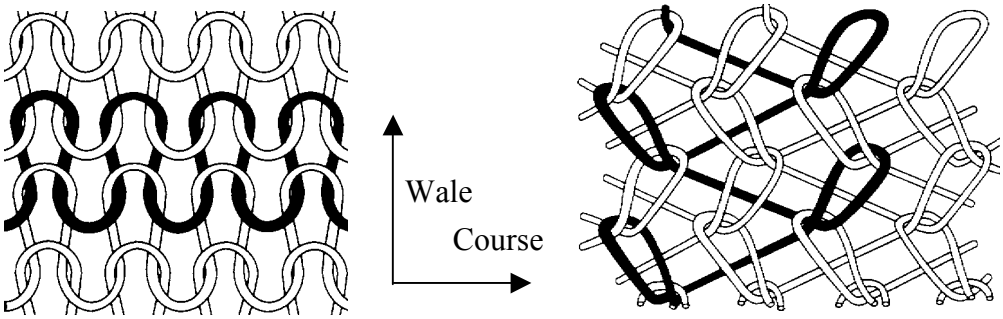

Figure 7: Typical weft-knitted fabric (left) and warp-knitted fabric (right) [10]

The major parameters influencing the mechanical properties of knitted fabrics are knit architecture, mechanical properties of wale and course yarns, matrix respectively resin

properties, fibre volume fraction and yarn orientation angle [4],[5],[28]. Several experimental studies were performed investigating these parameters.

Chou and colleages [22],[23] discussed the impact, tensile, flexural and fatigue behaviour of weft knitted and woven glass fibre reinforced epoxy laminates. The behaviour of rib stitched fabrics and plane weave fabrics were compared. The impact strength of the rib stitch reinforcement is much higher than that of the woven fabric. However, plane weaves have better tensile and flexural strengths.

Wu et al. [28] studied the mechanical properties of different types of warp knitted fabrics. They investigated the influence of the knit structure on the in-plane anisotropy as well as density and tensile properties. The tensile strength and modulus in course direction was higher than that of the wale direction. The absolute values are closely associated with the structure and density of the knit. Two fracture modes were observed: a) Fracture at resin rich regions and b) fracture due to stress concentration on the loop interlocking region.

Gommers et al. [26],[27],[7],[8] concentrated on warp knitted glass fibre reinforced epoxy resin. The dependence of the knit structure, fibre content, fibre orientation distribution and prestretching degree on stiffness and strength is studied. Figure 8 shows a polar plot of stiffness and strength for different materials to give an impression of the possible variation in anisotropy for different type of materials. The anisotropy of knitted fabrics can vary due to the structure of the knit but remains positioned between random mat and woven fabrics.

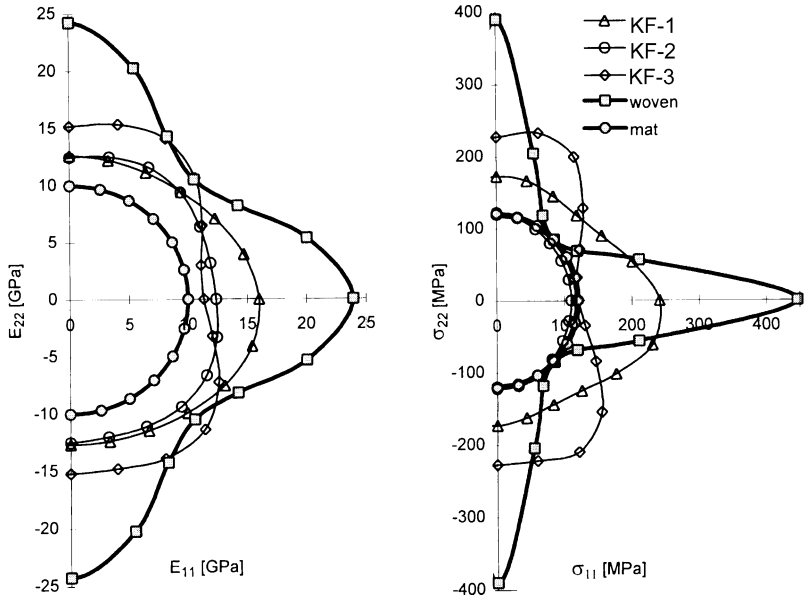

Figure 8: Polar diagrams of three types of knitted fabrics, a woven and random mat [8]

It was reported, that the stiffness has a clear linear relationship with the fibre volume content. Stretching the fabric before curing reorientates the loops and changes the mechanical properties of the fabric. Tensile stiffness and strength improve in stretch direction and decrease in the transverse direction. The fibre orientation distribution was represented by orientation tensors that allowed the description of a distribution function. Though there is a wide variety of orientation distribution within different types of knitted fabrics all investigated fabrics were at least triclinic. The stiffness and strength in tensile and shear loading were related to orientation tensor components. These relationships allowed evaluating a knitted composite with measurement of only the fibre content and orientation.

Karger-Kocsis, Mayer and coworkers [2] studied the mechanical behaviour, fracture mechanisms and fracture zones of glass and carbon fibre reinforced thermoplastics. The incorporation of knits in thermoplastic matrices cause a pronounced stiffness and strength anisotropy, which depends on loop density in wale and course direction [19]. They reported that the fracture toughness increased with the number of knitted layers due to a more homogeneous distribution of the loops. Other parameters influencing this property are the mesh size and yarn strength. The fracture zone is very diffuse for a single layer, but adopts a circular shape as a result of the homogeneous distribution for more layers. By using acoustic emission the following mechanisms rated for increasing damage were determined: matrix deformation, fibre-matrix debonding, fibre pull-out and fibre fracture [16],[17],[18],[20].

Some analytical and numerical models were presented for the prediction of the elastic behaviour of both warp and weft knitted fabrics under in-plane tension. The models for predicting the elastic properties can be divided in three categories based on their geometrical dimension [6],[14]. The simplest approach is a one-dimensional Krenchel model using an efficiency factor combined with a rule-of-mixtures method. The two-dimensional laminate approach uses plies in an imaginary laminate as basis of the loop respectively fibre orientations. The three-dimensional approach is based on the formulation of unit-cells of which the properties are described by averaging.

Rudd et al. [21] proposed a simple elastic model for the prediction of the mechanical properties of weft knitted glass fibre reinforced polyester laminates. In this model the tensile elastic properties were approximated by the rule-of-mixtures approach. Comparison of experimental results with predicted data showed reasonably accurate

stiffness behaviour but modifications concerning fabric relaxation appear to be necessary.

A similar model was developed by Ramakrishna and Hull [25],[13]. This model included elastic moduli as well as strength predictions. The elastic moduli were predicted by a modified rule-of-mixtures approach resulting in a reasonable agreement with experiments. However, predicted tensile strengths overestimated the experimental observations, probably due to the in-plane formulation and absence of bending stresses in the model.

Ramakrishna [9],[10],[11] also proposed a so-called “cross-over model”. This model considered the 3D orientation of the yarns by the crossing over of yarns of adjacent loops at the interlocking region. Elastic properties of the knitted fabric were determined by combining the effective stiffnesses of looped yarns with resin-rich regions in the laminated plate theory. This model also takes into account the fibre volume fraction and the presented model compared favourably with the experiments.

Ruan and Chou [15],[12] developed geometric models to correlate the preform microstructure with the composite elastic properties of weft knits. Here, an averaging method was used to obtain the elastic behaviour. The formulation of this analytical model assumed that an infinitesimal segment, which is formed by two parallel planes perpendicular to the warp direction, is subjected to a uniform strain. As a consequence, the conducted tensile and shear moduli were higher than the experimental values.

Investigations on the crashworthiness and the modelling of the energy absorption behaviour of knitted fabrics are limited to a small amount of studies. Ramakrishna and Hull [29] investigated the crush-zone morphology and the specific energy absorption of knitted carbon fibre reinforced epoxy resin tubes tested under axial compression. They considered the effects of fibre architecture and fibre content in order to optimize the reinforcement for maximum energy absorption capability. A similar study was performed with a knitted glass fibre reinforced epoxy resin, but included also the influence of the testing speed on the energy absorption capability and crush zone morphology [30]. The investigated knitted fabrics showed as expected a dependency of the test direction – warp or weft, respectively wale or course – on the crushing mode. The tubes tested in wale direction failed by fragmentation mode whereas the course tested tubes failed by splaying mode. This last mode displayed a higher energy absorption capability. This energy absorption decreased with increasing testing speed.

This last effect was also observed in a study from Huisman [31] on weft knitted glass fibre reinforced polyethylene terephthalate crash elements. Here, special attention was

given to the influence of the defined reference specimen geometry on the energy absorption behaviour. A comparison with other composites tested with the same geometry was made. A rise in the crashworthiness potential was observed with increasing fibre orientation respectively fibre content in test direction. This agrees with the observations of previous studies [29], [30].

In the frame of an European research project [2], which concentrated on the characterization of knitted fabrics, the potential and limitations to model the crash behaviour of such knitted fabrics was demonstrated. An anisotropic continuum damage model was developed, which takes into account the prestretching degree of the yarn loops, coupling of properties in wale and course direction due to the interlocking of yarns as well as a first approach to model the post-damage phase [32],[33],[48]. These studies also showed the limitations of the current numerical models and the standard finite element discretization with shell elements based on shell theory to simulate and predict the energy absorption behaviour of composites.

2 Experimental investigations

2.1 Investigated materials and manufacturing

2.1.1 Knitted glass fibre reinforced polyethylene terephthalate

For the experimental investigations Vetrotex Twintex R PET 730 is used. This is an intermingled yarn of both glass (GF) and polyethylene terephthalate (PET) fibres with a glass fibre volume content of 50%. These yarns are knitted on a 24" diameter wire-knitting machine resulting in tubes of circular plane weft knits (Figure 9).

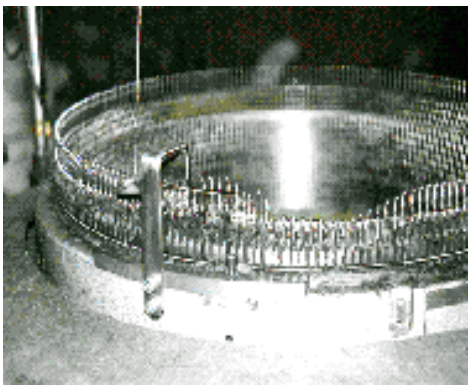

Figure 9: 24 Inches circular knitting machine (BUCK TSP, Bondorf, Germany)

The tubes are stacked to 4 double layers and impregnated to sheets on a double belt press [96],[97]. The knitted material is processed continuously between two steel belts. In the heating zone the thermoplastic matrix yarn melts and impregnates the fibres. In the cooling section the laminate consolidates under isobaric conditions. The produced sheets have a thickness of 1.4 mm and a width of 600 mm. Two sheets are stacked and clamped to a sledge, which moves into an IR heater field for contactless heating to a temperature of 295 °C. After reaching the melting temperature of the matrix, the sledge transports the laminate into the hydraulic press and the profile is pressed in a cold matched metal mould. Two profiled half shells are joined to a closed form, which represents the tested crash element geometry (Figure 10).

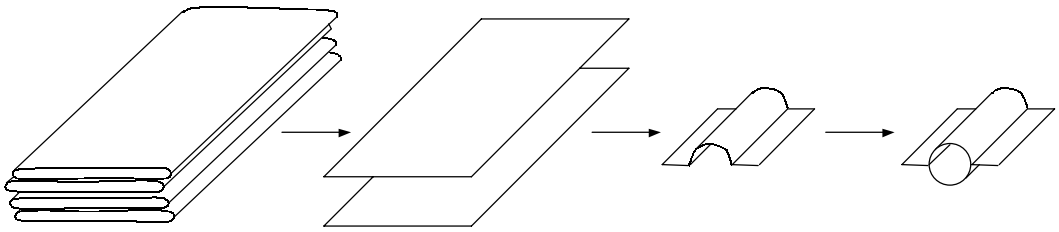

Figure 10: Schematic diagram of the manufacturing process of crash elements

During the forming process of knitted fabrics into more dimensional structures, the knits are stretched. This results in an increase of fibre orientation and i.e. in a higher Young's modulus and tensile strength. This behaviour is used to tailor the properties of the knitted structure and should thus be taken into account when characterising the material.

Parameters to quantify the structure of the knit are the loop densities ρ_c and ρ_w and the stretching degree λ_c and λ_w in course and wale direction respectively. The loop densities $\rho_{c,w}$ are defined as the number of loops per unit length. The investigated knitted fabric has a process dependent inherent stretching, which results in a loop size of 5 mm and 7 mm in course and wale direction respectively, while the unstretched situation would be 6 mm for both directions. In this most basic form $\rho_c = \rho_w = 0.167$ mm^{-1} and both prestretching degrees are $\lambda_c = \lambda_w = 1.0$. The prestretching degrees $\lambda_{c,w}$ are defined as the size of the loop relative to the original unstretched state coming from the knitting process. This definition allows for the assumption that knitted fabrics in the most basic form with equal loop densities and unstretched loops are isotropic [19].

The matrix system polyethylene terephthalate belongs to the group of thermoplastic polyesters. PET is a semi-crystalline thermoplastic, originally used for the fabrication of fibres but later also produced as sheets. The mechanical properties largely depend on the degree of crystallinity. Amorphous PET is preferred for transparency, high fracture toughness, good friction and wear behaviour and low shrinkage during processing [63]. Typical properties of the investigated PET are shown in Table 2.

Table 2: Typical properties of PET [71] (*: delivered state from manufacturer)

	Symbol	**Unit**	**Value**
Mass density	ρ	[g/cm^3]	1.32
Young's modulus	E	[MPa]	2600
Tensile strength	σ_u	[MPa]	57
Elongation at break	ε_u (K = 20)	[%]	130
Elongation at break	ε_u (K = 60)	[%]	50
Tensile yield strength	σ_y	[MPa]	55
Poisson's ratio	ν	[1]	0.43
Glass transition temperature	T_g	[°C]	70 - 80
Crystallite melting temperature	T_m	[°C]	245
Crystallinity degree	K	[%]	20*

Two states of PET are investigated. GF/PET(A) is the composite with the lower matrix crystallinity degree K(PET) = 27.5 % while GF/PET(C) has a matrix crystallinity degree K(PET) = 52.4 %. Taking into account the fibre volume fraction, the crystallinities are K(GF/PET(A)) = 17 % and K(GF/PET(C)) = 34 % respectively.
The first state comes from the before mentioned manufacturing press processes, while the second state is achieved by annealing the specimens at 130 °C for 12 hours additionally. The crystallinity is measured by the evaluation of samples from heat-flux Differential Scanning Calorimetry (DSC) and Thermogravimetry (TG) [64]. Coupling DSC with TG takes into account the fibre volume content. A peak in the measured heat flow rate ϕ_m curve occurs when the steady state is disturbed. This is realised by thermally activated heat production or consumption like recrystallization or melting of the polymer. Figure 11 shows the exotherm recrystallization peak at T_{rc} = 130 °C and the endotherm melting peak of the crystallites. The difference of the areas under both peaks determines the crystallinity degree K.

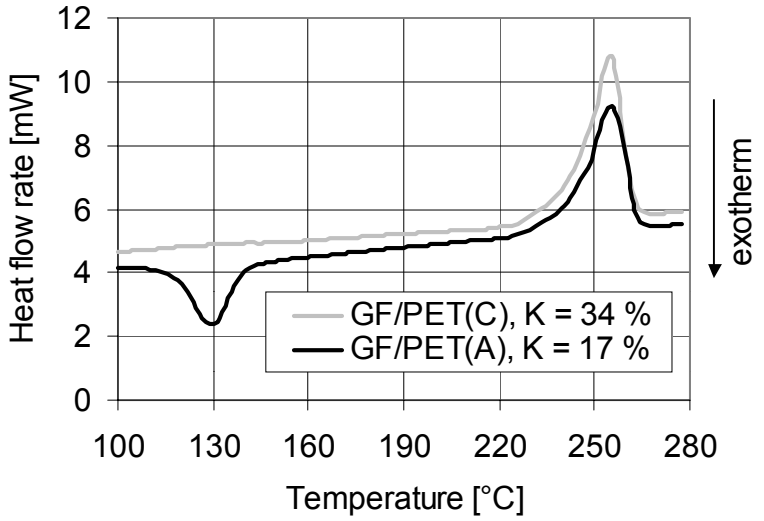

Figure 11: Heat flow vs. temperature of GF/PET(A) and GF/PET(C)

2.1.2 Chopped glass fibre reinforced polypropylene

The investigated glass fibre reinforced Polypropylene (PP) belongs to the group of glass mat reinforced thermoplastics (GMT). GMT usually comes in the form of thermoplastic sheets containing the fibres as a nonwoven random phase. These sheets are thermostamped to plates or halve shells to form the investigated specimens respectively crash elements. The investigated GMTs can be divided into two groups, i.e. chopped GMT and random mat GMT [65].

The matrix Polypropylene (PP) belongs to the group of synthetic plastics of polyolefines. PP is a semi-crystalline thermoplastic. Within the group of polyolefines PP has a relatively high strength, stiffness and crystallite melt temperature at a low density ρ of about 0.9 g/cm^3. The mechanical properties vary considerable depending on the typical composition - crystallinity, molecule structure and molecular mass - of the specific PP. The glass transition temperature is at about –10 - 0 °C. The crystallite melt temperature is at 160 - 165 °C. PP is often filled with talcum or other minerals, reduces the cost and increases properties like stiffness, strength, heat resistance and resistance against creep. Some basic properties of the tested GMTs can be seen in Table 3.

Table 3: Notation and basic properties of the investigated GMT

Material	**Random mat GMT**	**Chopped GMT**	**Mineral filled chopped GMT**
Notation	**PP/GF30R**	**PP/GF30C**	**PP/GF30C_MF**
Fibre length	~50 mm	~12.5 mm	~12.5 mm
Fibre content	30 wt-%	30 wt-%	~30 wt-%
Filler	-	-	~12 wt-%
Young's modulus	5000 MPa	4900 MPa	7100 MPa
Tensile strength	70 MPa	73 MPa	130 MPa
Mass density	1.15 g/cm^3	1.13 g/cm^3	1.28 g/cm^3

2.2 Experimental procedures

2.2.1 Crash tests

The experimental investigations on the crush behaviour are performed with a horizontal crash test rig, which is designed for experiments on larger specimens and structural parts [38]. Figure 12 shows a scheme of the mechanical assembly of the horizontal catapult system.

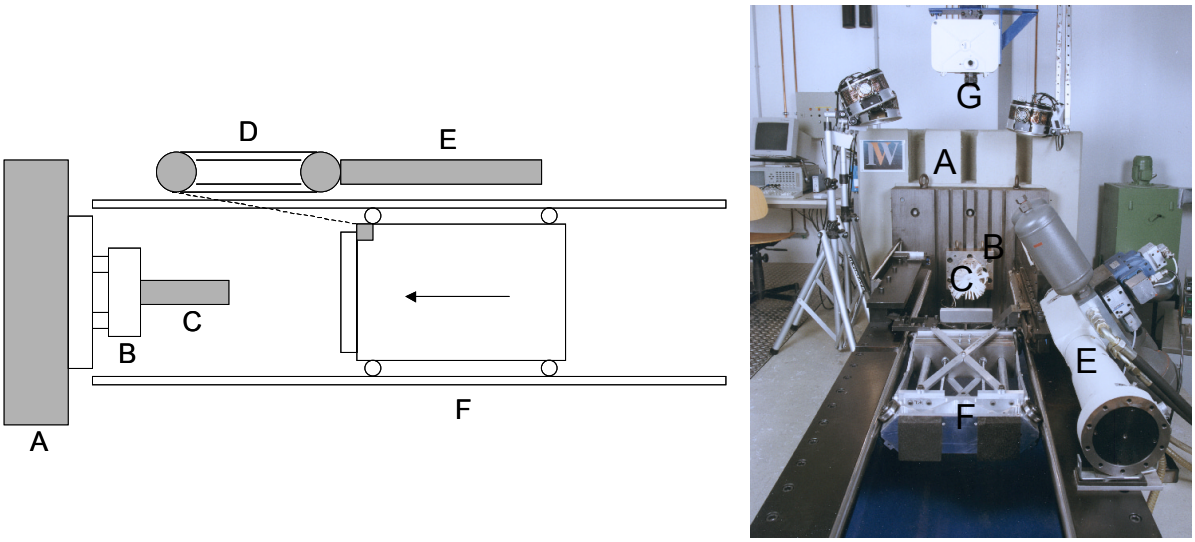

Figure 12: Principle and photograph of the horizontal catapult crash test rig: A) reaction mass, B) dynamo-meter, C) specimen, D) 1:9 pulley, E) hydraulic cylinder, F) impactor mass on carriage, G) high-speed camera

The test rig is based on the acceleration of a carriage with variable load by a hydraulic cylinder. The maximum crash energy is 15 kJ. The carriage velocity is adjustable

between 2 m/s and 24 m/s. The carriage traction rope is disengaged before the carriage reaches the specimen. This results in a specimen load exclusively based on the kinetic energy of the impactor mass. The specimen is clamped to the force measurement plate, which is equipped with four piezoelectric discs. Further measured parameters are the carriage displacement and the initial velocity at the onset of the crush event. A transient recorder with a sampling rate of 200 kHz is used for measurement data acquisition. All test results are filtered with a SAE 1000 Hz filter. Since the crash characteristics of a specific FRP depend on multiple factors, a test series is needed to obtain the quantitative influence of the different variables on the energy absorption behaviour. In literature a division into intrinsic and extrinsic variables is proposed [53]. Basically, intrinsic variables come from the material itself while extrinsic variables depend on the test conditions and specimen geometry (Figure 13).

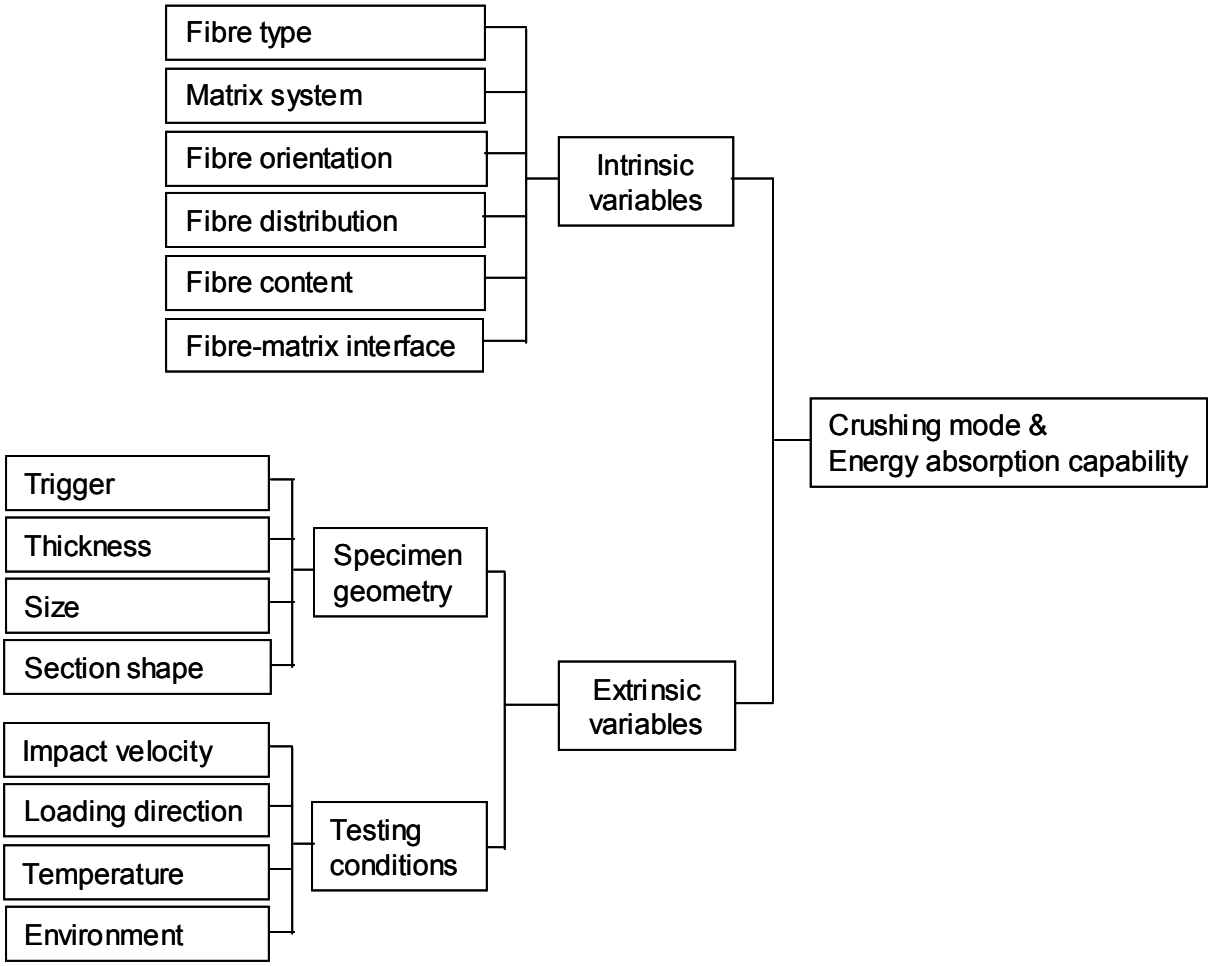

Figure 13: Variables influencing the crushing mode and the energy absorption capability of composites

As a result of this division, the intrinsic variables are determined by the choice of the investigated materials, i.e. knitted fabric reinforced PET and random mat reinforced PP. Concerning testing conditions, the impact velocity and temperature are subject to a parameter study, while loading direction and environment is kept constant, respectively axial loading and the surrounding humidity degree.

The geometry of the tested specimen has a large influence on the type of crush mode as well as the energy absorption capability. Many experimental studies showed that crash elements with a tubular cross-section are most efficient for energy absorption when failure occurs in a crushing mode [34],[35],[36],[37],[39],[40],[41],[42]. Therefore, a circular double hat profile as reference for the specimen geometry is defined. This shape is close to a tube, but has the advantage of manufacturability for a wide variety of composites. Especially crash elements made from thermoplastic composites can be manufactured by stamp forming under controlled process conditions. The almost ideal form of the force-displacement diagram of a typical tested crash element acknowledges the choice of the geometry of this crash element (Appendix, Figure 72).

All specimens were manufactured by these same consolidation and forming techniques (see also Chapter 2.1.1). The inner diameter D_i and the wall thickness t of the tubular part of the double hat profile depends on the stamp forming tool and has a nominal value of D_i = 50 mm respectively 2.3 mm (Figure 14). The flange width w is subject of a parameter study to obtain information on the division of energy absorption between flange and tubular part.

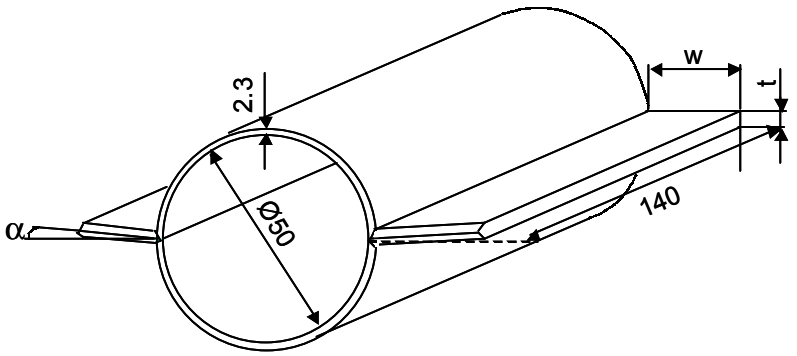

Figure 14: Geometry of a crash element (t_f: flange thickness, w_f: flange width, α: flange inclination)

To be able to compare the knitted fabric with other composites three methods of joining the flanges - vibration welding, riveting and adhesive bonding (PUR adhesive)-

are investigated. The flange thickness t depends on the respective joining method. The specimens are triggered by a 45° chamfer to create a local region of high stress, causing progressive damage of the material. A flange inclination $\alpha > 0^{o}$ reduces the peak force and guarantees the initiation of stable crushing at the tubular section. This inclination does not have a negative effect on the energy absorption. The sustained crush stress remains constant for all tested variants, while the stroke efficiency is constant and higher for non-zero inclinations α (Figure 15).

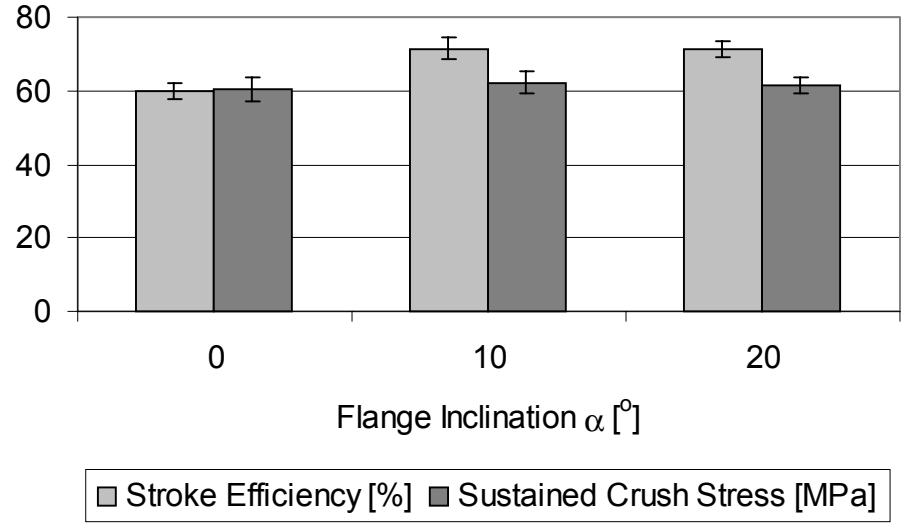

Figure 15: Stroke efficiency and sustained crush stress for different flange inclinations α

2.2.2 Impact and perforation tests

Impact tests on square plates of knitted fabric and chopped fibre mats (150 x 150 x thickness mm^3) were performed with a square support of 120 x 120 mm^2. The quasistatic tests were performed on a Zwick 1485, while dynamic tests were performed on an instrumented falling weight impact test machine (Fractovis of Ceast). The main material axes corresponded with the sides of the support. The plates were impacted by a metal cylinder with a diameter of 32 mm tipped with a hemisperically formed dart with a diameter of 45 mm (Appendix 8.3).

Measured parameters for both set-ups are force respectively acceleration, time and displacement of the impactor. The purpose of these tests is to demonstrate the size and shape of the damaged zone as well as investigate damage mechanisms for combined impact and bending loads perpendicular to the material plane. In order to compare the

impact behaviour of different materials the following characteristic parameters are defined (see also Figure 16):

F_{peak}:	Force at first peak	(2.1)
E_i:	Initiation energy, energy at peak force	(2.2)
E_{prop}:	Propagation energy	(2.3)
E_{tot}:	Total dissipated energy	(2.4)
$DI = E_{prop} / E_{tot}$:	Ductility index	(2.5)

The total dissipated energy E_{tot} can be divided into initiation energy E_i and propagation energy E_{prop}. The initiation energy is determined as the energy dissipated at the first peak force F_{peak}, while the propagation energy is the energy dissipated from this point until complete perforation. The ductility index DI indicates the ductile-brittle behaviour of the investigated material. The propagation energy and thus the ductility index increases with increasing ductility of the composite.

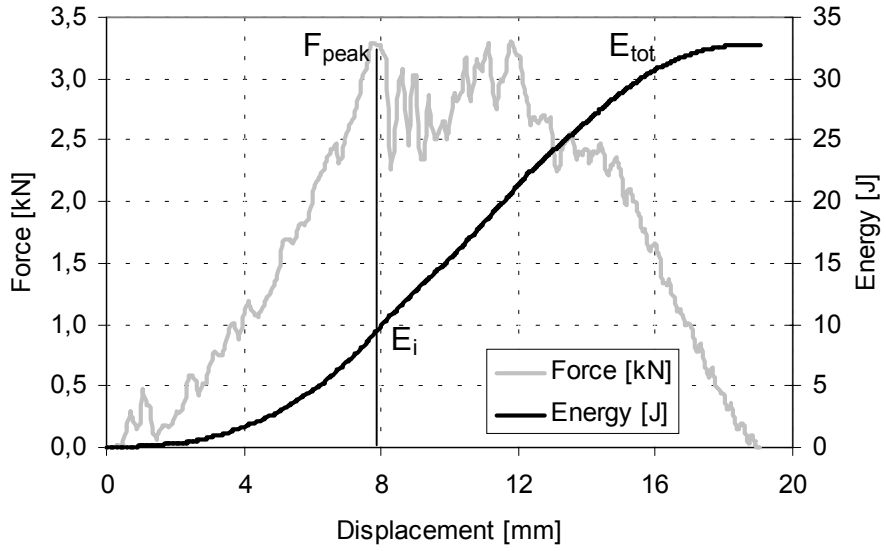

Figure 16: Typical force- and energy-displacement diagrams for perforation impact testing

Tests on mineral filled chopped GMT are performed at various impact velocities with a perforation assembly adopted to be used on both a hydraulic machine (Zwick) as well as a Split-Hopkinson Pressure Bar (SHPB). For this test, material with a larger thickness is needed, limiting the choice of material to GMT. Two different perforation supports with respective internal diameters D_{int} = 11 mm and 40 mm are used

(Appendix, Figure 74). Circular specimens for this investigation are cut from plates, which are manufactured like the chopped GMT double hat profiles used for crash testing with a flat stampforming tool.

The principle of measurement with a SHPB, e.g. [67], [109], is demonstrated in Figure 17. A projectile impacts the incident bar, which causes a compressive strain wave $\varepsilon_I(t)$ in the incident bar. A fraction of this wave - $\varepsilon_T(t)$ - transmits through the specimen and propagates into the transmitter bar. Another fraction - ε_R (t) - reflects at the interface between specimen and incident bar. Based on these strain-time histories and the theory of one-dimensional wave propagation the stress, strain and strain-rate are determined.

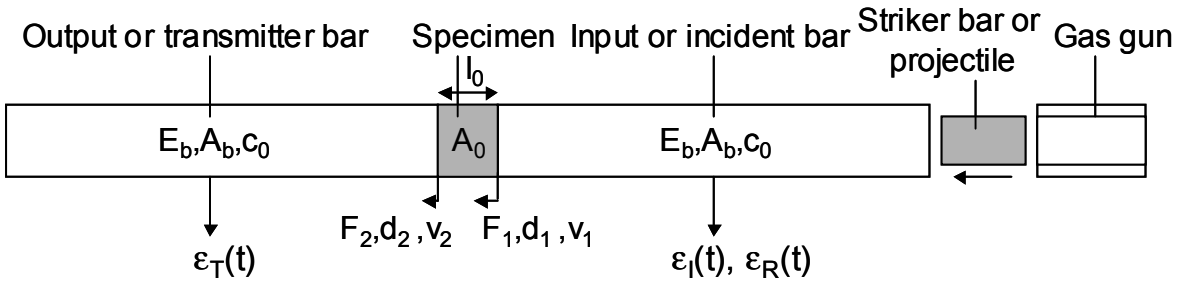

$$\varepsilon_{specimen}(t) = \frac{d_1(t) - d_2(t)}{l_0} = \frac{c_0}{l_0}\int_0^t (\varepsilon_I - \varepsilon_R - \varepsilon_T)dt$$

$$\sigma_{specimen}(t) = \frac{F_1 + F_2}{2A_0} = \frac{1}{2} E_b \frac{A_b}{A_0}(\varepsilon_I + \varepsilon_R + \varepsilon_T)$$

$$\dot{\varepsilon}(t) = \frac{v_1 - v_2}{l_0} = \frac{c_0}{l_0}(\varepsilon_I - \varepsilon_R - \varepsilon_T)$$

Figure 17: Principle of the Split-Hopkinson-Pressure-Bar (d,v: displacement, velocity).

In order perform shear impact, the SHPB-set-up is modified for direct impact [68],[69]. Here, the projectile directly impacts the specimen with known impact velocity $v_I(t)$. The axial force F(t) transmitted by the axisymmetric perforation support into the output tube can than be determined from the transmitted longitudinal elastic wave $\varepsilon_T(t)$. In case of the small internal support diameter D_{int} = 11 mm, an estimation of the shear strength τ_{max} can be made by the quotient of maximum axial force and middle circumferential cross-section:

$$\tau_{max} = \frac{F_{max}}{2\pi r_m \cdot t_{specimen}} \qquad (2.6)$$

The quasi-static tests were performed on a hydraulic machine (Zwick). In this case, the projectile is clamped and moved by the machine, while for high rates at the modified SPHB the projectile is moved by a gas gun. The purpose of these tests is to establish a transverse shear characterization as a function of strain rate and determine a possible rate sensitive transition.

2.3 Crashworthiness characteristics and energy absorption mechanisms

2.3.1 Knitted glass fibre reinforced PET

All tested crash elements failed by stable progressive crushing. The macroscopic appearance of the crushing zone is dominated by lamina bending with delamination of the laminate at the centre of the wall cross section and translaminar shear cracks in the laminae (Figure 18).

Figure 18: GF/PET(A) crash elements showing the macroscopic failure behaviour

The different joining techniques - riveting, adhesion and welding - satisfy their bonding function of the two crash element halves. The crash elements with halves

joined by vibrational welding show an almost ideal force-displacement diagram (Figure 19). Welding as joining technique of knitted thermoplastics has several advantages. Both element parts are joined continuously instead of discontinuously as is the case with riveting. Due to the three- dimensional structure of the knit, the laminae are strongly interlocked. This results in relative high transverse mechanical properties and has a positive effect on bonding by vibrational welding. Riveting results in a more pronounced fluctuation in the force level during crushing as a result of the discontinuous flange connection (Figure 19). This fluctuation however, has a negligable influence on the absorbed energy (Figure 20).

Compared to adhesive bonding, the flange width can be smaller when welding. For adhesive bonding a wider flange is needed to prevent separation of the halves during the crash event. The additional weight of the broader flange, the adhesive respectively the weights of the rivets have a negative influence on mass specific crash properties.

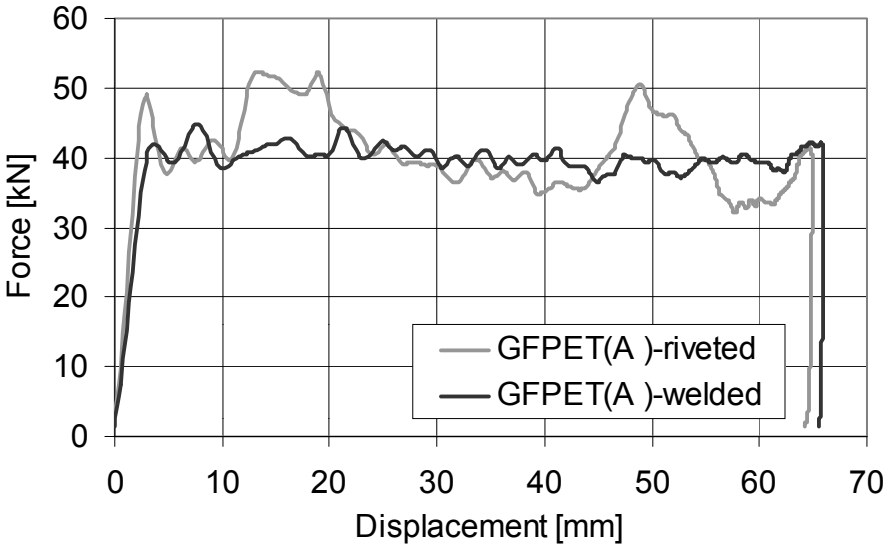

Figure 19: Force-displacement diagram for riveted and welded GF/PET(A) crash elements

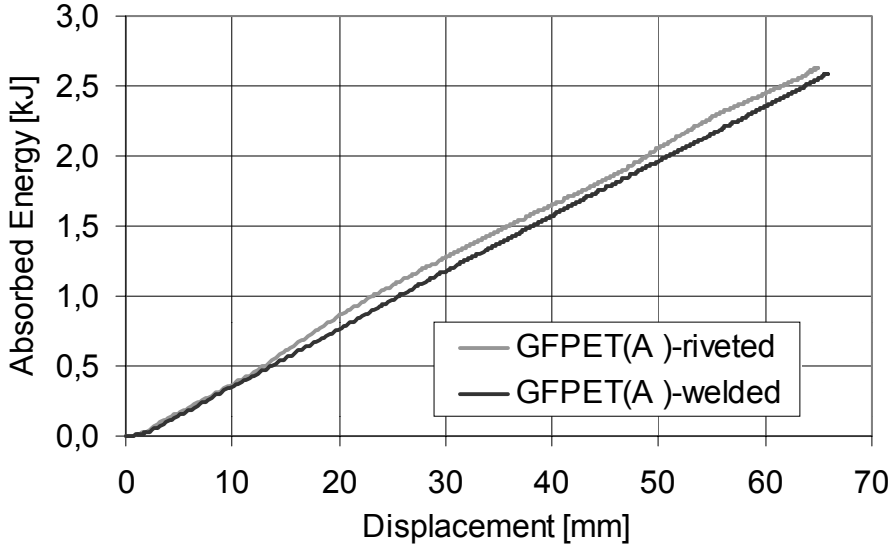

Figure 20: Energy-displacement diagram for riveted and welded GF/PET(A) crash elements

A test series with riveted flanges of different widths shows a decrease in specific absorbed energy with increasing flange width (Table 4). Here, only the parts with the smallest flange fail by progressive crushing over the whole cross section. The elements with wider flanges show a similar crushing behaviour for the tubular part but the flanges fail in a laminate bending mode with less translaminar cracks, which absorbs less energy. This acknowledges, that the tubular part of the crash element is better suited for energy absorption than the flange.

Table 4: Crash characteristics for GF/PET(A) crash elements (mean ± standard deviation)

Specimen series (n=5)				**F_m**	**E_s**	**σ_s**
Notation	**Bonding**	**α**	**w**	**[kN]**	**[J/g]**	**[MPa]**
A	Rivet	0°	30 mm	42.78 ± 1.73	30.65 ± 1.17	60.40 ± 3.25
B	Rivet	10°	30 mm	42.08 ± 1.38	30.30 ± 0.77	62.29 ± 3.05
C	Rivet	20°	30 mm	42.87 ± 1.31	31.26 ± 0.94	61.55 ± 2.18
G	Adhesive	10°	30 mm	45.65 ± 0.55	35.16 ± 0.43	60.67 ± 1.92
H	Weld	10°	15 mm	38.34 ± 0.96	39.37 ± 1.38	75.36 ± 2.79
V	Rivet	10°	15 mm	39.12 ± 1.40	34.71 ± 1.52	69.75 ± 2.47
U	Rivet	10°	20 mm	39.07 ± 1.30	31.95 ± 1.11	65.05 ± 3.71
B	Rivet	10°	30 mm	42.08 ± 1.38	30.30 ± 0.77	62.29 ± 3.05

Standard deviations of the results of the crash experiments are smaller than expected from the inhomogenity of the knitted structure. Small differences between adjacent loops and knits resulting from the knitting process do not have a significant influence on the crash behaviour.

To investigate the influence of the flange inclination on the peak force at the onset of load, the angle α of the flanges is varied. When $\alpha = 0°$, the impactor contacts the full crash element cross section. This results in the presence of a pronounced peak force. For inclinations greater than 0°, i.e. $\alpha = 10°$ or 20°, the peak is almost absent. This change in the geometry of the flange inclination, respectively the presence or absence of a peak force, does not influence properties like the specific absorbed energy or sustained crush stress (Table 4), since the additional area under the peak is relatively small.

The PET matrix state has an especially high influence on the size of the central delamination. The increased brittleness, micro-cracks and a decrease in fibre-matrix adhesion in the crystalline phase are responsible for the distinctive central delamination within the GF/PET(C) crash elements. These effects result in considerably lower crash characteristics (Table 5 and Appendix 8.2, Figure 70 and Figure 71).

Table 5: Crash characteristics for GF/PET(A&C) crash elements with different crystallinity K(PET), (mean ± standard deviation)

Specimen series (n=5)				**F_m**	**E_s**	**σ_s**
Notation	**K**	**α**	**w**	**[kN]**	**[J/g]**	**[MPa]**
U	27.5 %	10°	20 mm	39.07 ± 1.30	31.95 ± 1.11	65.05 ± 3.71
M	54.5 %	10º	20 mm	28.12 ± 3.83	23.53 ± 2.96	51.55 ± 7.21

Tests with varying initial impact velocities on crash elements with different crystallinity degrees clearly demonstrated the influence of the PET-state on the crash behaviour. For increasing impact velocities, the crush response decreases (Figure 21). This behaviour is stronger for higher crystallinity degrees K of the matrix system.

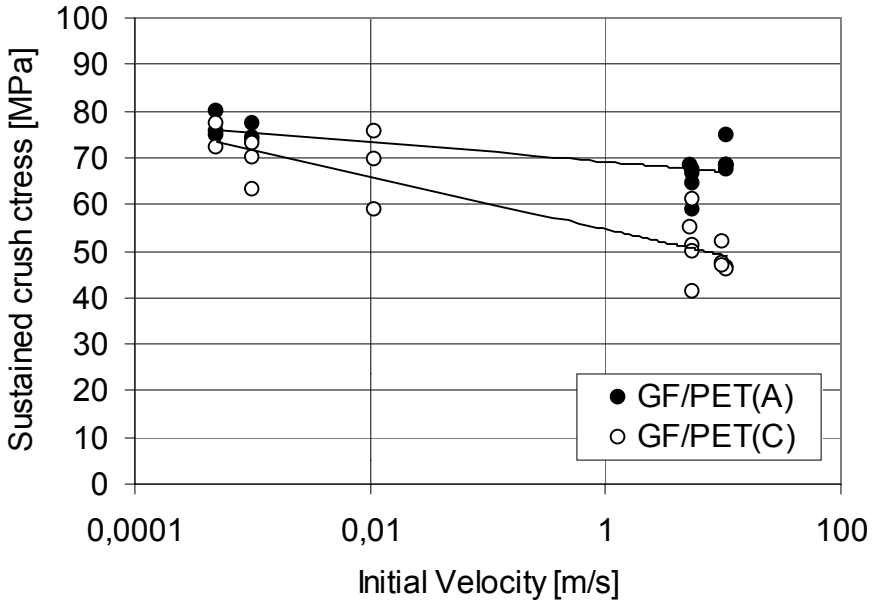

Figure 21: Sustained crush stress σ_s vs. initial velocity v_0 for GF/PET(A) and GF/PET(C)

This seems to be in contradiction to typical measured strain rate behaviour with increasing strength response for higher rates. However, the governing failure mechanisms in the crush zone differ from the failure behaviour in usual strain rate characterizations. Crack propagation of the central delamination and delaminations due to transverse shear dominate the crush response, while usual rate tests are tensile tests with fibre fracture and fibre pull-out. The mechanism responsible for the rate dependent behaviour is the visco-elastic character of the thermoplastic matrix system of the composite. Here, the crystallinity degree of the PET-polymer has a large influence on the ductility of the matrix [66].

An additional effect during crash testing is a temperature increase at the crash front and on the surface of the fronds up to at least 140 ºC, measured by an infrared thermocamera [103]. The fact that for some tests parts of the debris wedge are welded to the impactor acknowledges at least these high temperatures at the contact surface. Furthermore, observations of micrographs show the existence of a small zone of material which forms a transition film between polymer respectively debris and the laminate (Figure 22). The thermal activity at the surface of the fronds is assumed to be bounded to this very thin film at the contact region with the impactor and only influences the coefficient of friction between impactor and crash element.

The dominating macroscopic failure mode determining the appearance of the crush zone is lamina bending. The irregular structure of the knit causes local deformation

mechanisms like kinking of part of loops, transverse shear cracks within laminae and local delaminations of separate loops and fibre bundles. Due to the typical property of the knitted structure of allowing some stretching of partially damaged loops and fibre bundles, longitudinal cracks forming separate outer fronds hardly occur.

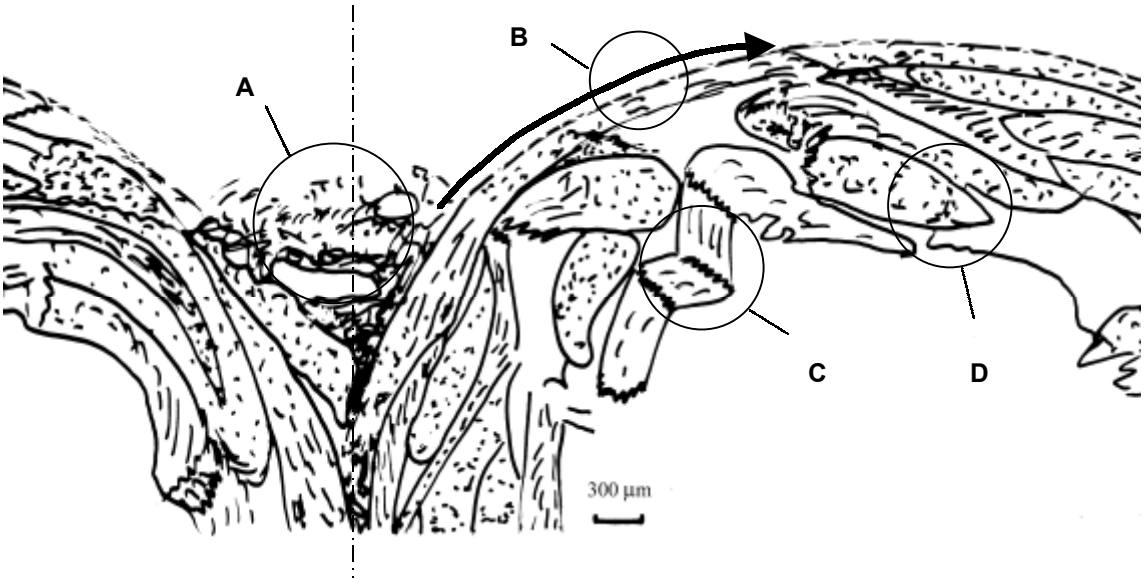

Figure 22: Schematic illustration of the crush zone of knitted GF/PET(A); A: partial wedge of debris, B: layer with a smooth transition between debris and adjacent loops and matrix, C: kinking of loops, D: transverse shear of loops.

In order to associate mechanical properties to the crush response of the tested materials, a differentiation of the crash elements in results for the flanges and the tubular part is needed. The test series on GF/PET crash elements with different flange widths allow a normalization of the double hat profile geometry to a circular cross-section with definitely one governing failure mode.

Here, the normalized cross-section A_n is defined as quotient of flange area A_f and original profile area A_0. This definition and the presence of only one type of failure mode at the tube part, enables the scaling of the sustained crush stress to the tubular section of the double hat profile by extrapolation of the data to $A_n = 0$ (Figure 23). The value $A_n = 0$ represents a perfect tube. In combination with the observed governing failure mode and the dependency on the impact velocity, the extrapolated sustained crush stress can be identified with the transverse shear strength. Under the assumption that this extrapolation can be made for all velocities, parallel extrapolations give an indication of the rate sensitivity of the shear strength.

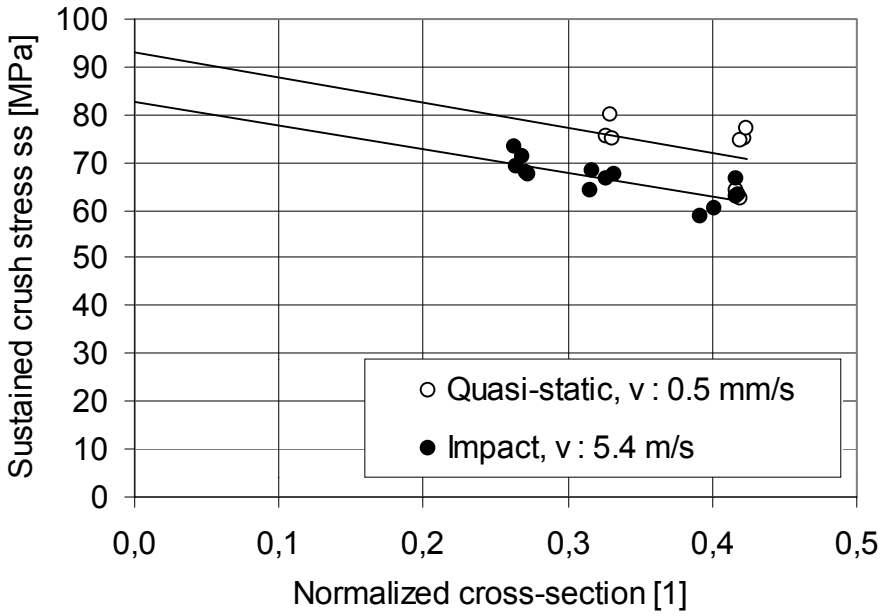

Figure 23: Sustained crush stress σ_s vs. normalized cross-section A_f/A_0

2.3.2 Chopped glass fibre reinforced PP

All crash elements, independent of the GMT type, fail by progressive crushing. Similar as for the knitted fabric, the laminate is divided into two fronds by a central delamination zone (Figure 24). One frond bends to the inner side of the crash element while the other bends to the outer side of the element. While bending to the outside, the radius changes and causes radial stresses resulting in longitudinal cracks.

The fronds of the chopped GMTs show delamination at the inherent layers coming from manufacturing. The test series on the random mat GMT with fibre lengths of about 50 mm show less delaminations within the bended fronds. Due to the longer fibres, the interaction between the layers is stronger. This also explains the slightly higher energy absorption capability. The resulting crash characteristics for the different GMT types are summarized in Table 6.

Figure 24: Crash elements of PP/GF30C (left), PP/GF30C_MF (front) and PP/GF30R (right)

Table 6: Crash characteristics for GMT crash elements (mean ± standard deviation)

Specimen series (n = 3 - 4)			**F_m**	**E_s**	**σ_s**
Notation	**Material**	**V_0 [m/s]**	**[kN]**	**[J/g]**	**[MPa]**
C	PP/GF30R	4.3	40.61 ± 3.11	41.09 ± 3.32	50.20 ± 4.17
G	PP/GF30C	4.3	31.04 ± 2.78	36.44 ± 3.22	47.70 ± 3.49
K	PP/GF30C_MF	4.3	44.61 ± 0.59	39.03 ± 0.38	53.96 ± 0.79
D	PP/GF30R	9.5	36.97 ± 2.28	37.91 ± 1.81	46.72 ± 3.10
H	PP/GF30C	9.5	29.18 ± 0.15	34.24 ± 0.82	43.34 ± 1.33
L	PP/GF30C_MF	9.5	42.39 ± 1.73	37.37 ± 1.19	51.66 ± 3.29

Interesting is the state of the contact surface of the separate fronds. Here, a thin film with fibres, mainly reoriented in longitudinal direction, indicates a thermal increase during crushing, which reaches melting temperature of the PP-matrix (Figure 25, B). Each frond of the chopped GMT is delaminated with fibre bridging between the layers (Figure 25, C). The fracture surface between the longitudinal cracks of the outer fronds is dominated by fibre pull-out in radial direction.

Investigations on the crash velocity show a similar tendency as observed for the KFRP (Figure 26). However, the slopes of the curvatures are different. For the mineral filled variant of the investigated GMTs, the effect can even be neglected.

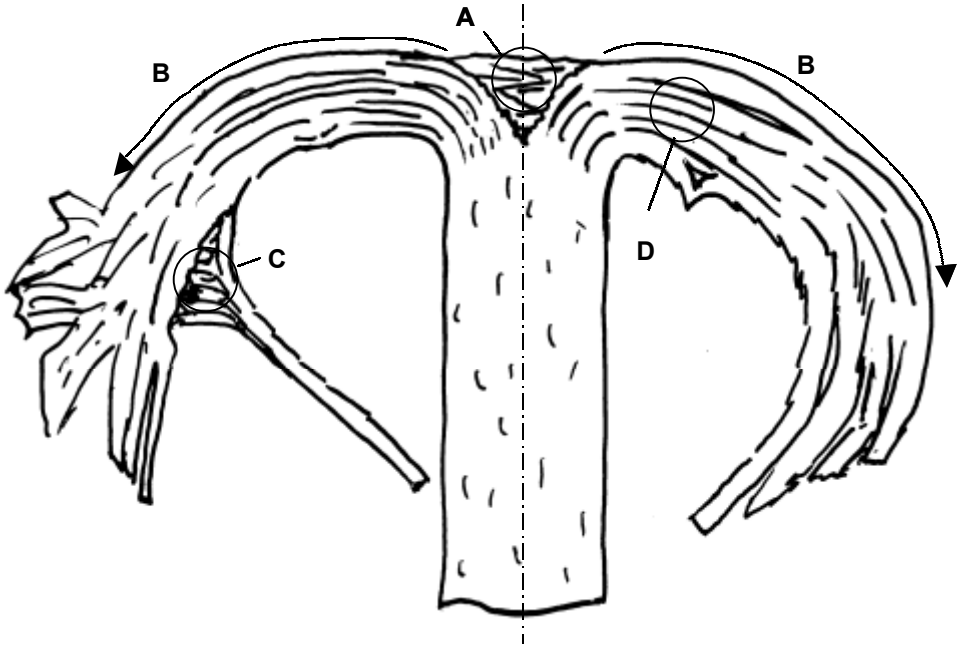

Figure 25: Schematic illustration of the crush zone of chopped GMT; A: wedge of debris, B: film of PP-matrix, C: fibre bridging, D: delaminations.

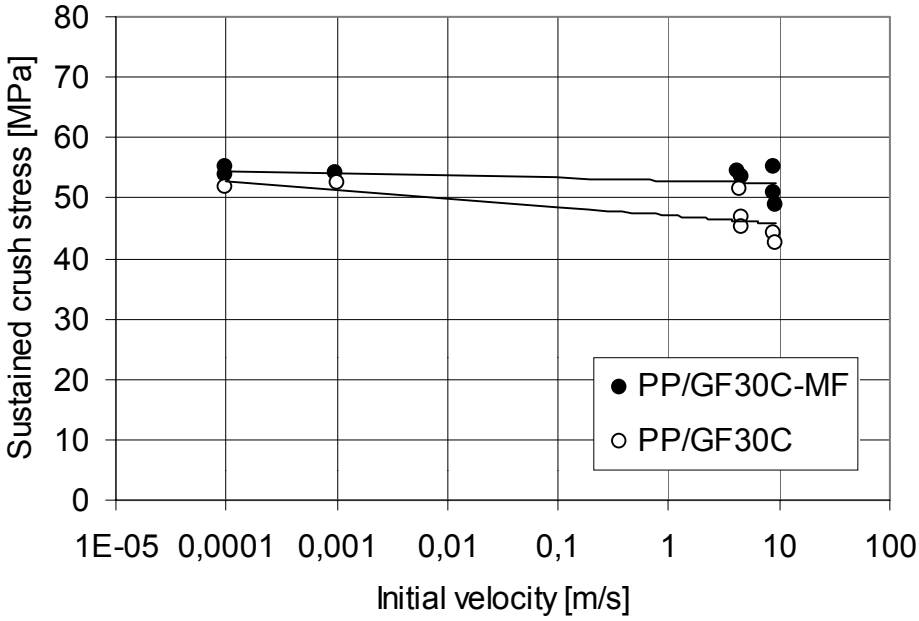

Figure 26: Sustained crush stress σ_s vs. initial velocity v_0 for chopped GMT (PP/GF30C) and mineral filled chopped GMT (PP/GF30C-MF)

2.4 Impact and perforation behaviour

2.4.1 Knitted glass fibre reinforced PET

Impact tests with impactor diameter D_i = 32 mm show the effect of the plate thickness on the ductility (Table 7). However, the difference in the ductility index DI is caused by the occurrence of additional elastic bending of the plate with the smaller thickness. This demonstrates the difficulty of the interpretation of the quantitative results since DI is no real ductility index, but also contains elasticity, impactor and specimen geometry dependent properties. Therefore, the resulting governing failure mechanisms and values for DI obtained with D_i = 32 mm can only be limited compared.

Table 7: Impact characteristics for knitted GF/PET(A)

D_{imp} [mm]	Material	t [mm]	v [m/s]	F_{peak} [N]	E_{tot} [J]	E_i [J]	E'_{tot} [J/mm]	E'_i [J/mm]	DI [1]
32	GF/PET(A)	1.42	0.0005	4015	76.2	18.9	53.7	13.3	0.74
32		3.30	0.0005	9696	133.9	52.5	40.6	15.9	0.61
20	GF/PET(A)	1.42	3.65	3226	20.3	10.5	14.3	7.39	0.48
20		1.42	4.44	3143	29.6	13.8	20.9	9.68	0.54
20		1.42	4.83	3311	32.8	12.5	23.1	8.80	0.62

Experiments with an impactor diameter D_i = 20 mm show less bending behaviour and material failure by perforation. Tests with varying initial impact velocities demonstrate the rate sensitivity with the ductility index. The increasing ductility index with increasing test speed of this material indicates a shift to the left for the location of the force peak in the force-deflection diagram. This does not automatically mean an increase in ductility as could be concluded from the ductility index.

Nevertheless, these tests can still be used for the investigation of the propagation of damage within the material. Figure 27 shows the damaged state of knitted GF/PET(A) at three stages of impact energy. The photograph of the damage zone just before perforation demonstrates presence of an anisotropic predamaged zone, which follows the prestretched state of the loops. These pictures also show the order of damage and failure mechanisms. While at 20 J the main damage occurs in the matrix and at the fibre bundle and matrix interface, at 30 J failure is dominated by fibre bundle separation form the laminate. When increasing the impact energy further to 35 J, the

interlocking property of the meshed bundles, allow some visible stretching of the knitted loops before final bundle failure.

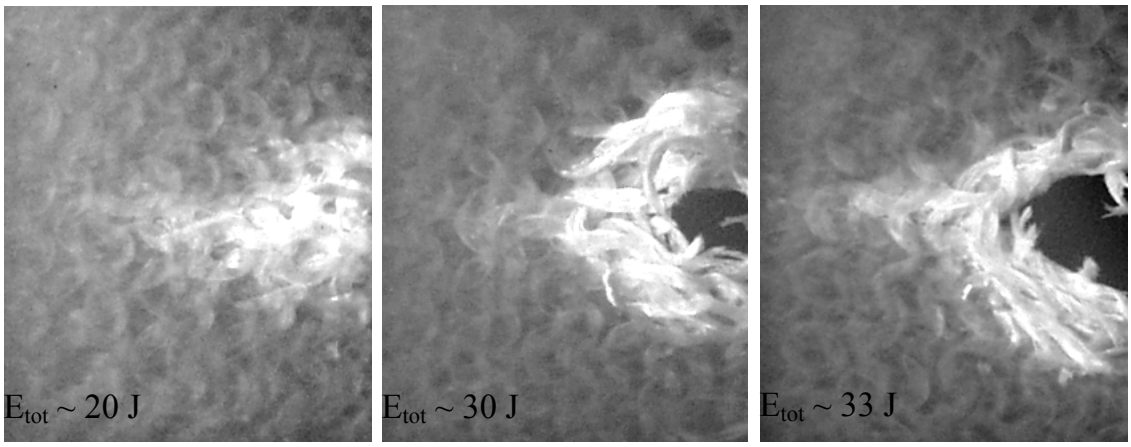

Figure 27: Damage development in knitted GF/PET(A) at 20J, 30J and 35J impact energy

2.4.2 Chopped glass fibre reinforced PP

Results of impact tests on the different types of GMT show the same influence of the thickness on the ductility index and failure behaviour as for the investigated knitted fabric (Table 8). However, when comparing the velocity, the differences between the ductility indexes DI show a reversed behaviour. This would respond to the expectations of decreasing ductility with increasing test speeds. In combination with the observed failure behaviour of the knitted fabric and the heterogeneous failure by separation of larger parts of laminae, these indexed ductility results only give a first indication of the capacity of the materials. Deducing material behaviour of these tests is not possible.

Table 8: Impact characteristics for different GMTs

Material	**t [mm]**	**v [mm/s]**	**F_{peak} [N]**	**E_{tot} [J]**	**E_i [J]**	**E'_{tot} [J/mm]**	**E'_i [J/mm]**	**DI [1]**
PP/GF30CMF	3.00	0.5	2177	37.2	8.50	12.4	2.83	0.77
	3.00	5.0	2248	34.7	9.53	11.6	3.18	0.73
	5.03	0.5	4450	53.8	22.3	10.7	4.44	0.58
	5.03	5.0	5040	63.9	29.7	12.7	5.90	0.54
PP/GF30R	5.00	0.5	3706	66.4	25.2	13.3	5.03	0.61
PP/GF30C	5.00	0.5	5712	110.8	47.0	22.2	9.41	0.57

The direct shear perforation tests on the SHPB however, distinguish clearly between energy absorption due to transverse shear and a combination of shear and bending as a result of the support. The maximum forces obtained with the perforation support with a small internal diameter (D_i = 11 mm) are higher than those obtained with D_i = 40 mm (Figure 28).

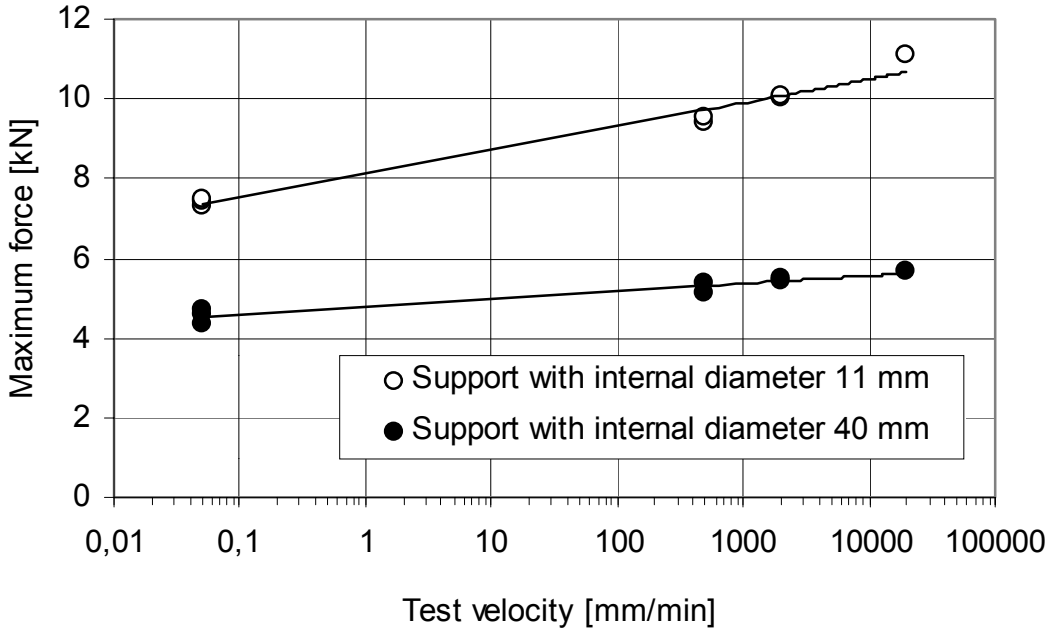

Figure 28: Influence of impactor velocity on the maximum force

An approximation of this diagram can be made in terms of a Johnson-Cook-type estimation:

$$F_{max} = F_0 + \beta \ln(\frac{v_i}{v_0}) \qquad (2.7)$$

with

F_0 : Reference maximum force for tests performed at v_0 ($F_0(D_{11})$ = 4.76 kN, $F_0(D_{40})$ = 8.11 kN),

v_0 : Reference velocity for quasi-static testing (v_0 = 1.0 mm/min), and

β : Proportionality coefficient ($\beta(D_{11})$ = 0.0834 kN, $\beta(D_{40})$ = 0.259 kN)

For the perforation set-up with the small internal diameter, the governing failure mode is directly determined by the transverse shear properties of the material. This allows a

transformation of the force-velocity curvature into strength and strain rate. Equation (2.7) becomes with equation (2.6) and rewritten in the following form:

$$R_{i3} = R_{i3,0}\left[1 + c\ln\left(\frac{\dot{\varepsilon}_i}{\dot{\varepsilon}_0}\right)\right] \qquad (2.8)$$

with

R_{i3} : Transverse shear strength for tests performed at $\dot{\varepsilon}_0$ ($R_{i3,0}$ = 47.92 MPa),

$\dot{\varepsilon}_0$: Reference strain rate for quasi-static testing ($\dot{\varepsilon}_0 = 10^{-2}\ s^{-1}$), and

c : Proportionality coefficient (c = 0.032).

The differentiation between the quasi-static region and dynamic region is more exposed in terms of dissipated energy (Figure 29). These results present clearly a sensibility for testing at two regions, i.e. quasi-static and dynamic. The static-dynamic transition for this type of test is at the test velocity of 500 mm/min respectively a strain rate of $\dot{\varepsilon} = 5 \times 10^{0}\ s^{-1}$. Since the strength shows a linear relationship with respect to the test velocity, the division of the energy response into a static and dynamic region is caused by the ultimate strain. A change in failure mode may be the cause of the difference in maximum strain, but further research is needed to specify the failure behaviour in terms of dissipated energy more clearly.

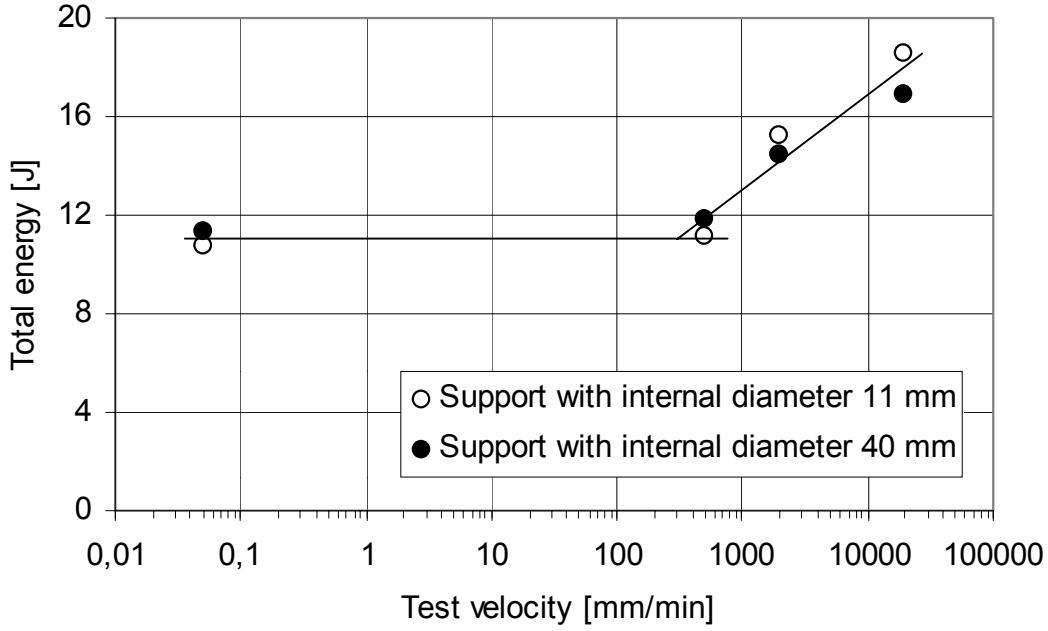

Figure 29: Influence of impactor velocity on the total energy

The coupling of this test and failure with progressive crushing is demonstrated by block compression tests. Here, a simple 10 x 10 x thickness cutout of a flat specimen is compressed between two flat planes. The compressive stress drops to a constant level after reaching the strength and failure proceeds by progressive crushing (Figure 30). This is caused by a change in failure mode from compressive failure to transverse shear failure. Measurements of the transverse shear strength on a SHPB acknowledge the magnitude of this level to be dominated by transverse shear properties and the possibility to characterize the dynamic transverse properties with a simple coupon test.

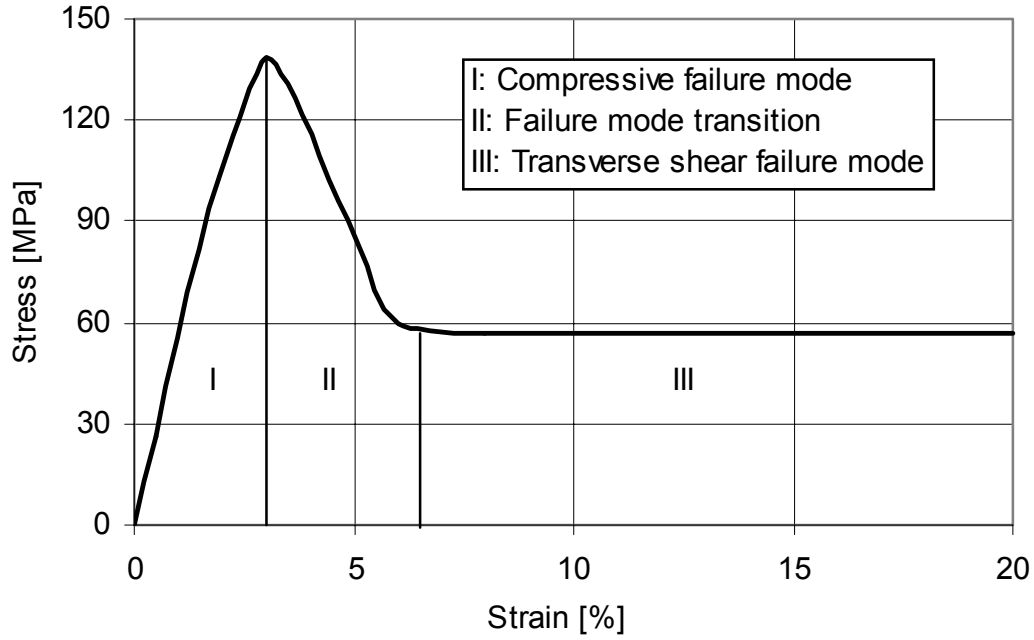

Figure 30: Typical compressive stress-strain diagram for block compression of PP/GF30CMF

3 Numerical investigations

3.1 The finite element model

3.1.1 The explicit finite element method

The Finite Element Method (FEM) is chosen as spatial discretization tool for the transient analysis and as platform to investigate constitutive laws for thermoplastic composites. The discretized non-linear equation of motion is defined in matrix notation as:

$$\underline{\underline{M}}\,\underline{\ddot{x}}(t) = \underline{F}^{ext}(t) - \underline{F}^{int}(t) + \underline{H}\ (t) \tag{3.1}$$

Here, $\underline{\underline{M}}$ represents the mass matrix, $\underline{\ddot{x}}$ the vector with accelerations of the degrees of freedom, $\underline{F}^{ext}$ the external nodal forces, $\underline{F}^{int}$ the internal nodal forces and $\underline{H}$ the hourglass resistance as a function of time t. To solve the non-linear equation of motion the central difference method is used [47]. This method calculates the acceleration, velocity respectively displacement by:

$$\underline{\ddot{x}}_n = \underline{\underline{M}}^{-1}(\underline{F}_n^{ext} - \underline{F}_n^{int} + \underline{H}_n) \tag{3.2}$$

$$\underline{\dot{x}}_{n+\frac{1}{2}} = \underline{\dot{x}}_{n-\frac{1}{2}} + \underline{\ddot{x}}_n \Delta t_n \tag{3.3}$$

$$\underline{x}_{n+1} = \underline{x}_n + \underline{\dot{x}}_{n+\frac{1}{2}} \Delta t_{n+\frac{1}{2}} \tag{3.4}$$

Here, the time step at time n+½ is defined by:

$$\Delta t_{n+\frac{1}{2}} = \frac{(\Delta t_n + \Delta t_{n+1})}{2} \tag{3.5}$$

The geometry is updated by adding the cumulative displacement increments to the initial geometry. The explicit time integration is called explicit since properties at time n+1 are exclusively determined from known properties at time n and time n+½.
The constitutive law of interest is implemented in the FEM-code with as input the strain and strain rate (or velocity) increments, $\Delta\varepsilon_n$ respectively $\Delta\dot{\varepsilon}_n$. As output the

material model calculates the stress increments $\Delta\sigma_n$, which are added to the cumulative stress of the last time step n-1 to form the new stress state at time n (Figure 31). More information on FEM-theories is available in [44],[45],[46].

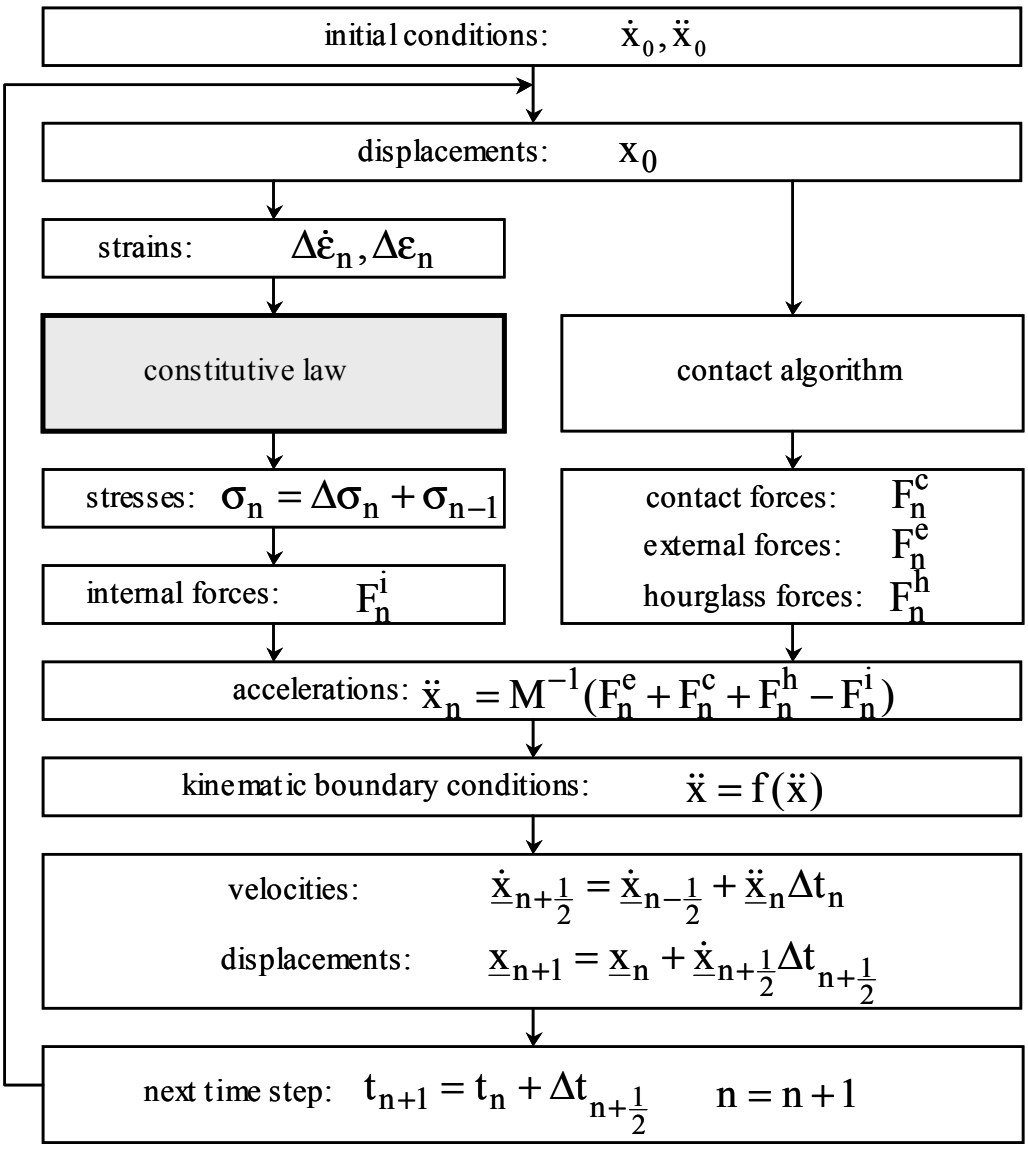

Figure 31: Schematic diagram of the explicit finite element method

3.1.2 The numerical set-up

A 3D model of a double hat profile is proposed to investigate and qualify the crushing mechanisms. The reduction of the flange geometry to a circular geometry with one governing failure mode allows the investigations of the tubular part only. A longitudinal segment from the tubular part of the profile is used as basis for the FE-model (Figure 32). Preliminary simulations of a 1°-slice to take into account the radial

elongation of the tubular cross-section showed numerical vibrations perpendicular to the loading direction in the symmetry plane. These vibrations prevented a stable progressive crushing. A simplification of the model with parallel cut symmetry planes as quasi-radial boundary introduces a plane consideration with suppressed radial strains.

The trigger region should be meshed with a very fine mesh to accomplish the onset of stable progressive crushing [61]. This would lead to unacceptable computing times, even for this simplified model. However, the main interest lies with the quantification of the mean crush force respectively the sustained crush stress after the onset of crushing. Therefore, the trigger is modelled as partially crushed with debris wedge, which allows a relative coarse mesh. Modelling the trigger this way, guarantees a numerical kinematic defined mechanism. The shape and size of the wedge is obtained from micrographs of crushed specimens of the investigated material (e.g. Figure 70, Appendix).

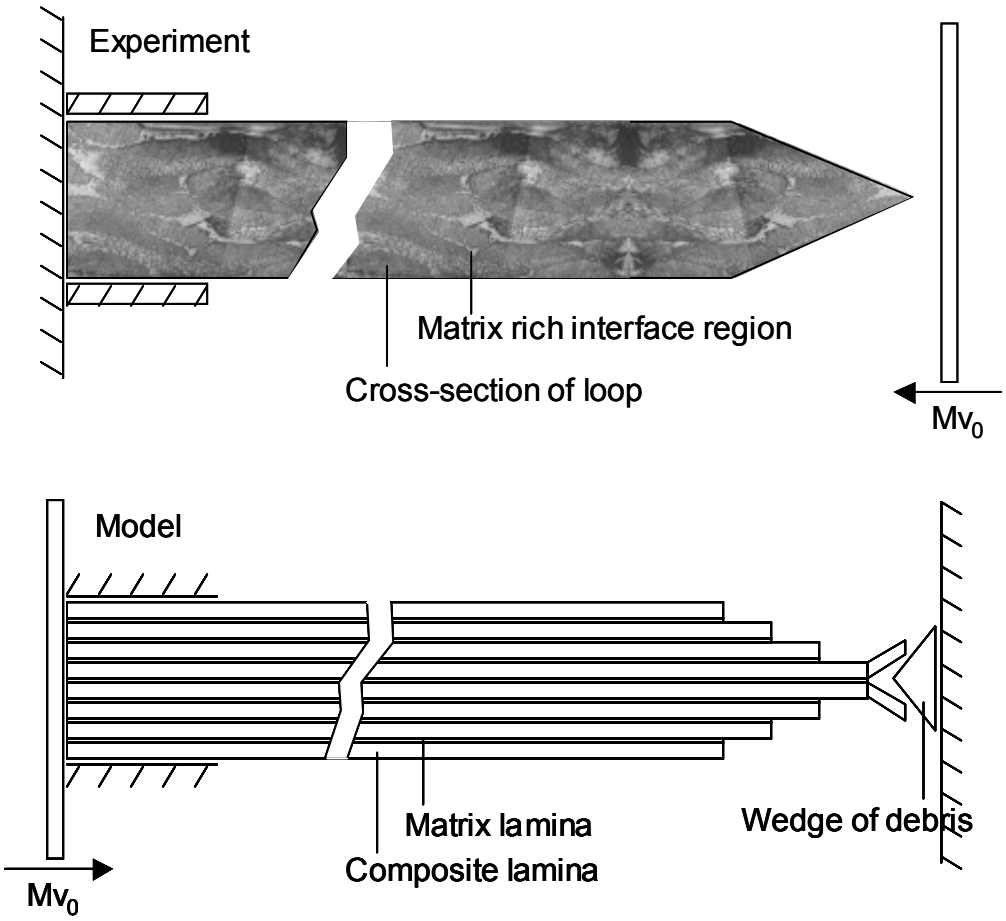

Figure 32: Experimental basis and FE- model of a longitudinal double hat profile segment

The mesoscopic model represents an idealized composition of the experimentally investigated materials and consists of 8 homogenized composite laminae separated in thickness or z-direction by 7 matrix interphase laminae. The composite laminae have a thickness t_l = 0.275 mm and the interphase laminae t_m = 0.0138 mm such that the thickness of the experimentally tested composite of t_L = 2.3 mm is obtained. The segment has a depth of 1 mm in y-direction and a length of 25 mm in x-direction.
The load is introduced by a moving rigid wall with mass M and impact velocity v_0 at the backside of the segment. The impactor mass M is chosen very high to obtain an almost constant impactor velocity over the crushed length. A non-moving rigid wall in front of the segment delivers the reaction forces. The symmetry conditions prevent moving in y-direction for all elements. The z-movement of the elements near the moving wall is suppressed by a fixed boundary to represent the experimental clampings. Furthermore, contact is defined between standing rigid wall, composite and wedge, wedge and composite as well as within the composite as a result of delamination (Figure 33). The first contact is of a kinematic type, while the rest are penalty types with new contact surface generation for eroded elements.

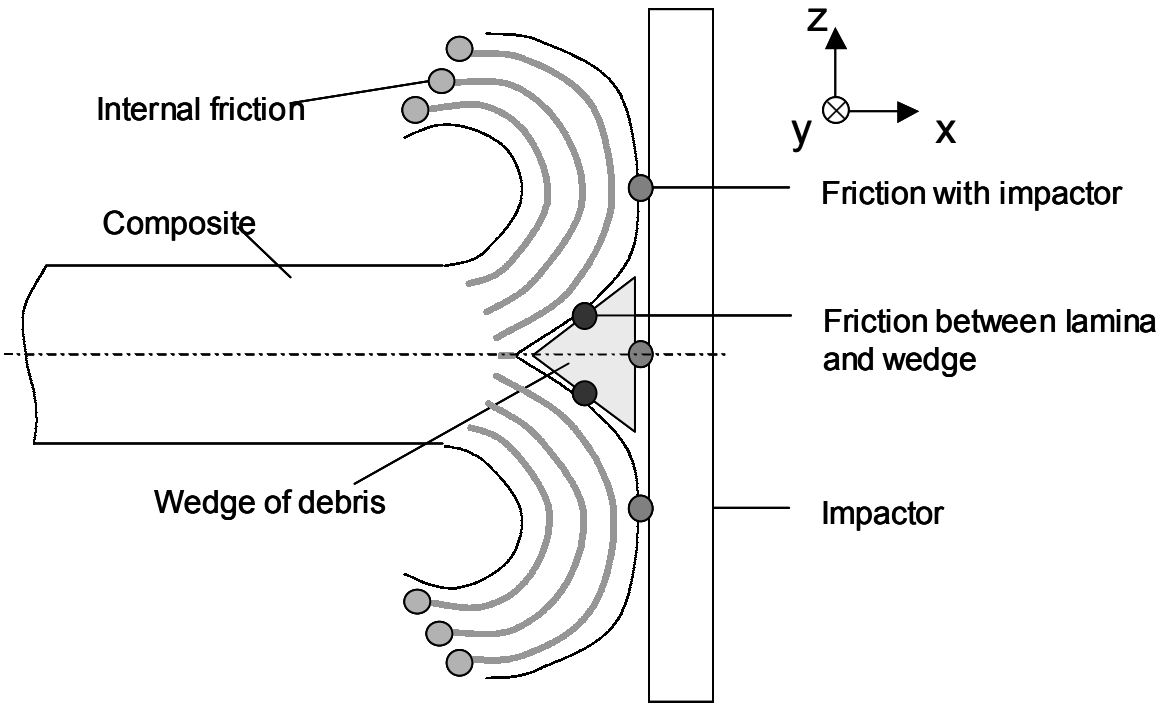

Figure 33: Occurrence of friction in the FE-model

3.2 Material models and properties

3.2.1 Matrix interphase laminae

The thermoplastic matrix is modelled with an isotropic elasto-plastic model with properties based on the two states of PET with different crystallinity degrees (Table 9). The crystallinity has influence on the Young's modulus as well as on the ultimate strain, while changes in strength or yield stress are neglectable and are kept constant [98],[99]. When reaching the ultimate strain, the element is eroded from the simulation. This serves to simulate the delamination of the laminae. For the simulations including the rate properties of PET values of C = 11.4 and p = 8.33 are incorporated in the model of Cowper-Simonds [91].

Table 9: Mechanical properties and parameters for PET-model

Property	**Symbol**	**Unit**	**PET(A)**	**PET(C)**
Crystallinity degree	K	[%]	27.5	52.4
Young's modulus	E	[MPa]	2766	3745
Poisson's ratio	ν	[1]	0.43	0.43
Initial yield stress	σ_y^0	[MPa]	54.5	54.5
Tangent modulus	E_T	[MPa]	3.073	5.489
Failure strain	ε_u	[1]	0.81	0.45
Strain rate parameter	C	[MPa]	- / 11.4	-
Strain rate parameter	p	[1]	- / 8.33	-

3.2.2 Wedge of debris

The wedge of debris consists of matrix and fibre fragments in a more or less random oriented state. Preliminary simulations showed numerical instable behaviour due to wedge deformation for low modulus and low strength properties. Therefore, the wedge material behaviour is assumed to be isotropic elasto-plastic with the Young's modulus $E_{wedge} = 2E_{composite}$, Poisson's ratio $\nu = 0.3$, yield stress $\sigma_y = 300$ MPa and a tangent modulus $E_T = 0.1E_{wedge}$. Rate effects and strain failure are not considered.

3.2.3 Composite laminae

The composite laminae are assumed homogeneous and isotropic within this mesoscopic model [19]. Since thermoplastic composites consist of both a ductile phase - the matrix - and a brittle phase - the fibres -, a CDM model with coupled damage and plasticity is chosen for simulation [93],[94]. This model decomposes the strain tensor ε as

$$\varepsilon = \varepsilon_e + \varepsilon_p \tag{3.6}$$

with ε_e the elastic strain tensor and ε_p the plastic strain tensor. Common strains at break for TPCs are in the order of magnitude of 0.05 allowing the above decomposition of strains. Damage is introduced within the relationship between effective stress $\hat{\sigma}$ and true stress σ with the damage operator D as follows

$$\hat{\sigma} = \frac{\sigma}{1 - D} \tag{3.7}$$

Thus, defining the elastic stress-strain relation as

$$\sigma = (1 - D)C : \varepsilon_e \tag{3.8}$$

where C is a fourth order tensor with elastic constants. The yield function reads with the equivalent von Mises stress σ_{eq}, the initial yield stress σ_y^0 and the isotropic strain-hardening parameter R

$$f(\sigma, R, D) = \frac{\sigma_{eq}}{1 - D} - (\sigma_y^0 + R) \tag{3.9}$$

The uniaxial stress-strain curve is divided into plastic and viscous parts in the following form

$$\sigma(\varepsilon_p, \dot{\varepsilon}_p) = \sigma_y^0 + Q_1(1 - \exp(-C_1\varepsilon_p)) + Q_2(1 - \exp(-C_2\varepsilon_p)) + V_k(\dot{\varepsilon}_p)^{V_m} \tag{3.10}$$

with Q_i and C_i the isotropic hardening parameters, V_k and V_m the effective plastic strain rate parameters, ε_p the effective plastic strain and $\dot{\varepsilon}_p$ the effective plastic strain rate. Figure 34 gives a graphical representation of the influence of the parameters on the CDM-model.

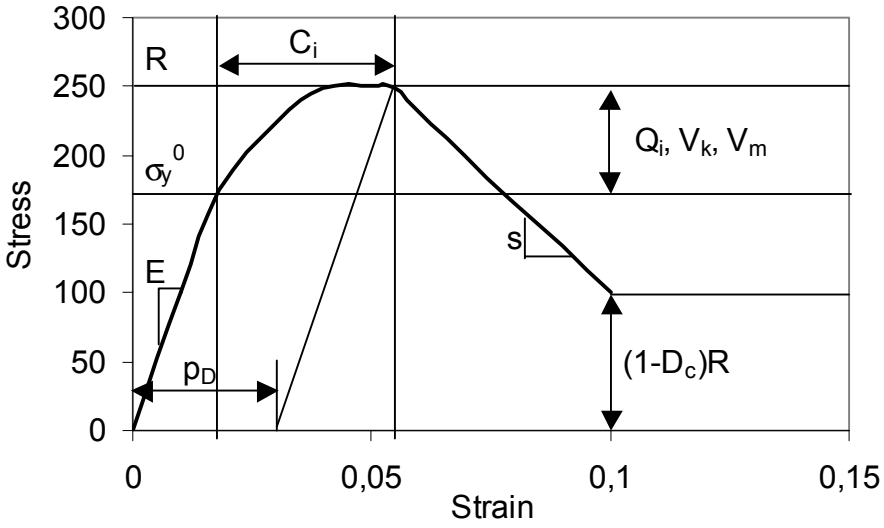

Figure 34: Graphical representation of the CDM-model to describe the composite laminae

The implemented formulation of a failure criterion after Hill [79] reads

$$\sigma(\varepsilon_p,\dot{\varepsilon}_p) = F(\hat{\sigma}_{22}-\hat{\sigma}_{33})^2 + G(\hat{\sigma}_{33}-\hat{\sigma}_{11})^2 + H(\hat{\sigma}_{11}-\hat{\sigma}_{22})^2 + 2L\hat{\sigma}_{23}^2 + 2M\hat{\sigma}_{31}^2 + 2N\hat{\sigma}_{12}^2 \tag{3.11}$$

in which F up to N are anisotropic strength parameters and $\hat{\sigma}_{ij}$ the effective stress components.

Parameters for this model are based on the extrapolation of experimental investigations on anisotropic knitted fabrics to the isotropic non-stretched state of knitted GF/PET with equal loop density, e.g. $\lambda_w/\lambda_c = 1/1$ and $\rho_w/\rho_c = 0.167/0.167$. For the isotropic case the compressive and tensile strengths are assumed to be identical. Strength parameters that could not be obtained from the available experimental data, where chosen to agree with the ideal isotropic situation. The damage threshold and resistance parameters p_D and s are subject of the investigations. The strength R is also varied with changes in the hardening parameter Q1.

Table 10: Mechanical properties and model parameters for knitted GF/PET(A) (LS-DYNA 950 Material "elasto-visco-plasticity with damage")

			GF/PET(A)
Property	**Symbol**	**Unit**	**λ_w/λ_c = 1/1**
Young's modulus	E	MPa	15600
Poisson's ratio	ν	1	0.30
Initial yield stress	σ_y^0	MPa	175
Isotropic hardening parameters	Q1	MPa	25
	C1	1	250
Damage threshold	$\dot{\varepsilon}_p^D = p_D$	1	0.035
Damage resistance	s	1	0.50
Critical damage	D_c	1	0.90
Viscous parameters	V_k	MPa s	0
	V_m	1	0
Yield criterion parameter	F,G,H	MPa^{-2}	0.5
Yield criterion parameter	L,M,N	MPa^{-2}	1.5

3.3 Results

3.3.1 Geometrical aspects of the crush zone

The appearance of the crushed FE-model is governed by bending and delamination of the laminate into internal and external parts or fronds. A central crack (mode I crack opening) of length l_c is located in the centre of the laminate anticipating the wedge. Delamination of the subsequent laminae is caused by transverse shear (mode II crack opening) of the interphase matrix. Deformation sequences of two states of the composite laminae at the time t = 0, 0.3, 0.6 and 0.9 ms respectively, can be seen in Figure 35 and Figure 36.

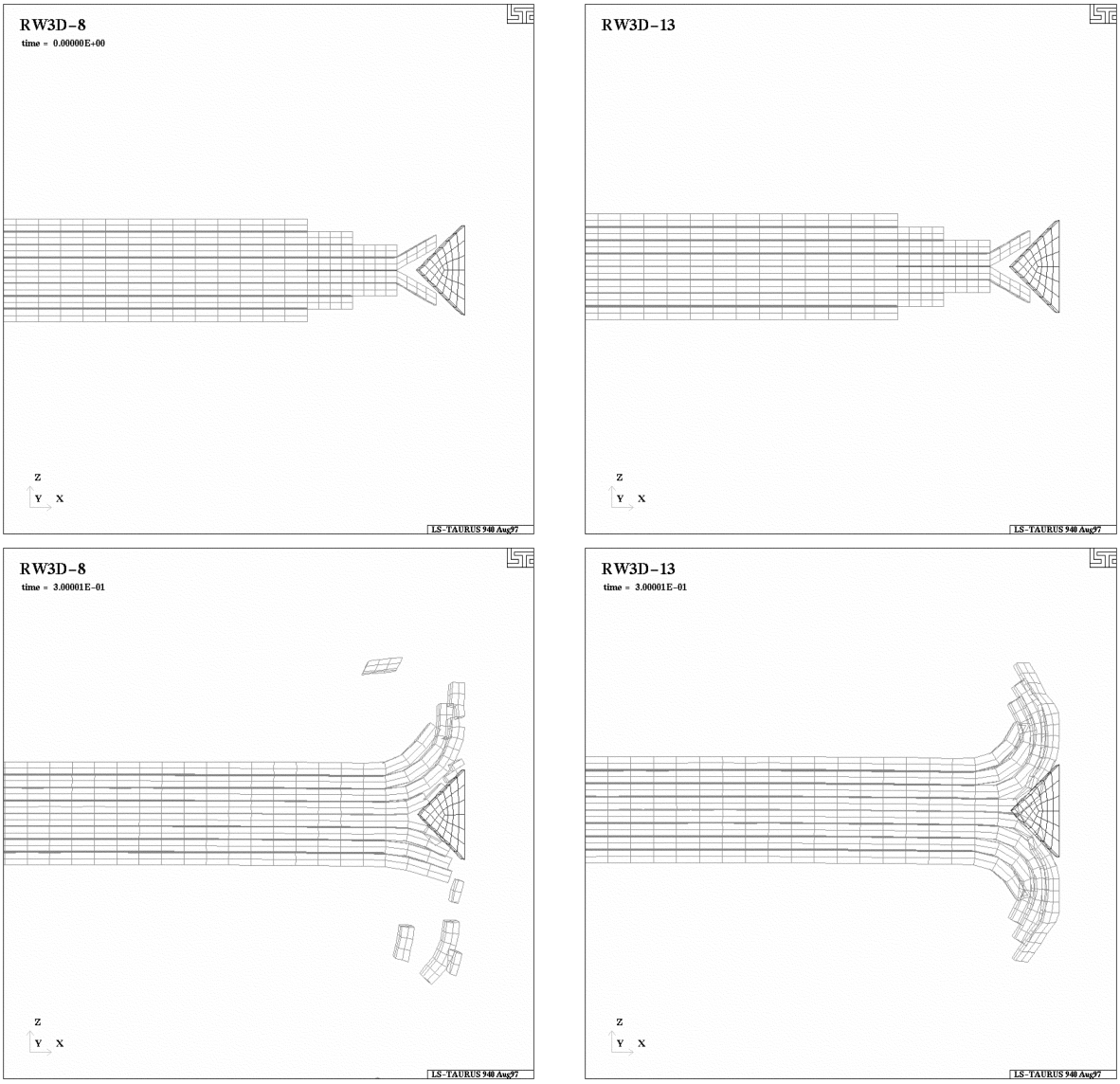

Figure 35: Deformation sequences of damage dominated (left) and a plasticity dominated (right) material at t = 0 ms and t = 0.3 ms

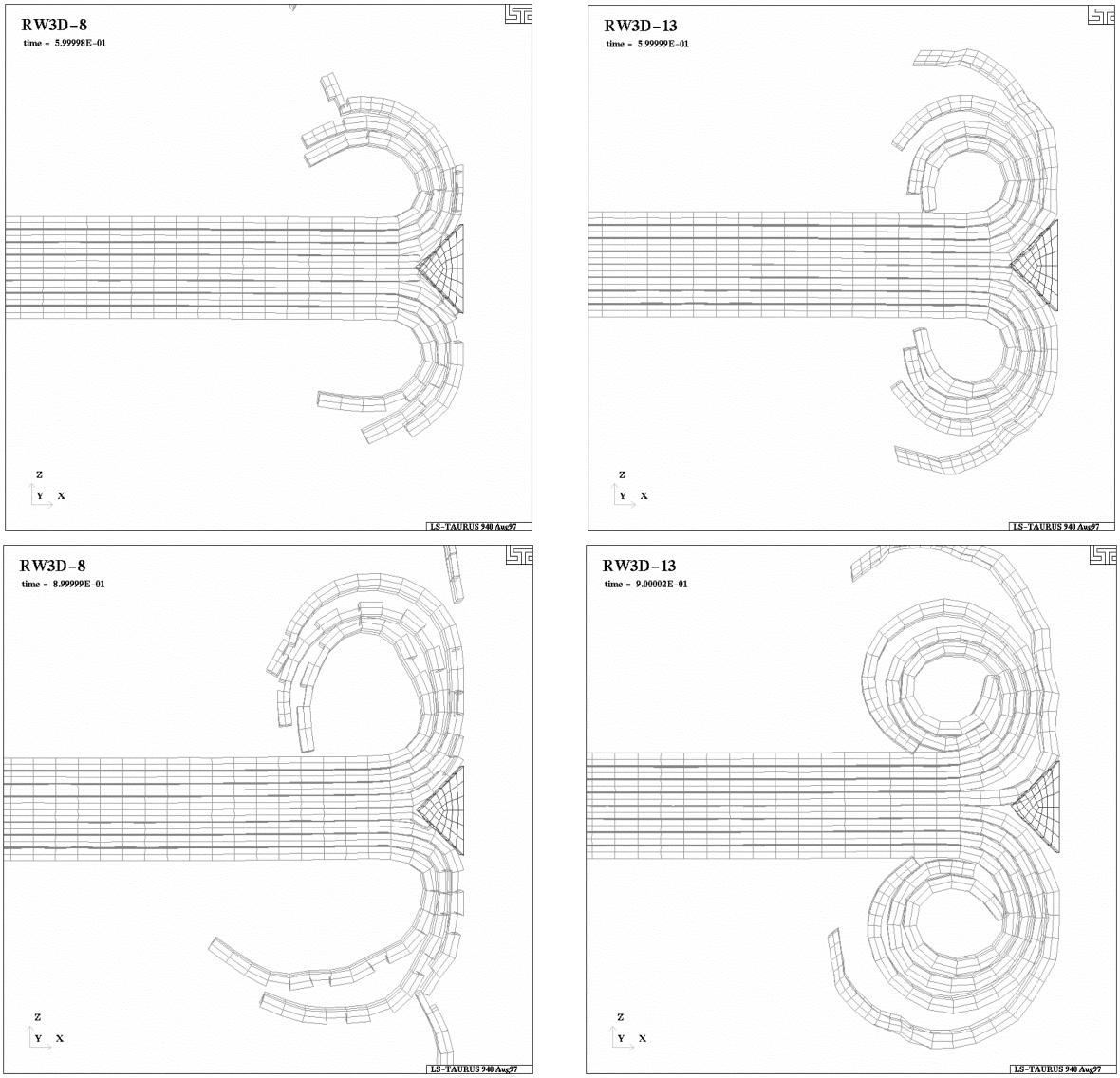

Figure 36: Deformation sequences of damage dominated (left) and a plasticity dominated (right) material at t = 0.6 ms and t = 0.9 ms

These states are defined as damage respectively plasticity dominated depending on the onset of damage with the definition of the damage threshold $\dot{\varepsilon}_p^D$ = 0.035 respectively 1.0. The damage dominated state represents the isotropic extrapolation of realistic material data with a strong softening after reaching the strength, while the latter state can be interpreted as the ductile variant with near elastic-ideal plastic behaviour.

The ductility respectively the amount of permanent strain determines the behaviour after relaxation of the delaminated laminae. The fronds of the damage-dominated state are more or less inversed while fronds of the plasticity dominated state roll up (Figure 37).

The ductility of the fronds also determines the size of the zone with maximum shear and thus the onset of delamination respectively the initiation of the central crack. The matrix interfaces fail near the crack tip region. The shear stress is distributed in a v-shaped zone with a tendency to pronounce for less ductile materials due to the more concentrated bending zone at the subsequent crack tips. However, the initiation of delamination respectively the central crack remains within the same zone anticipating the wedge of debris.

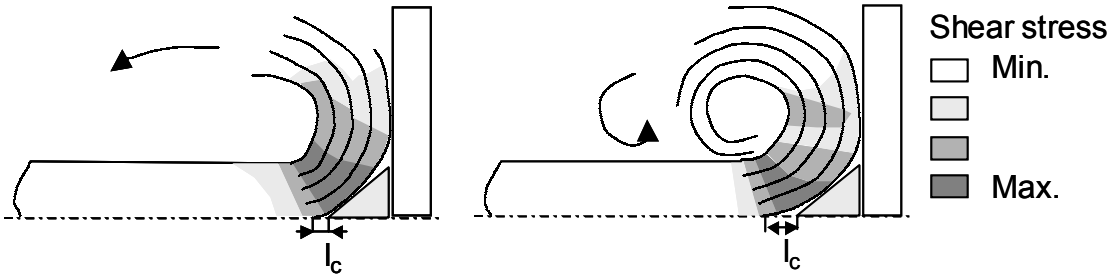

Figure 37: Schematic diagrams of the deformation appearance and shear stress distribution for a damage (left) and a plasticity (right) dominated material.

The experimental wedge is a result of excessive wear of material within the trigger region. In this FE-model the wedge is present from the beginning of the simulation. As soon as the internal and external fronds contact the rigid wall the difference with the experiment fade away and a comparison with the experimental progressive crushing can be made. Therefore, evaluations of the mean crush force and sustained crush stress do not consider simulation results before each lamina contacts the impactor at 0.3 ms (for v_0 = 10 m/)s.

Simulations with smaller wedge opening degrees show minor influence on the results. However, a choice of a very broad wedge decreases the obtained sustained crush stress. This is explained by the leverage of the wedge on the fronds. In reality the shape of the wedge is a function of the mechanical behaviour of the separate fronds and not vice versa thus the leverage is limited.

The difference in the post-failure behaviour of the laminae determines the distribution of the force flow over the fronds and the wedge (Table 11). In general it can be stated that the proportion of the fronds reaction forces on the impactor increase for higher remaining post-failure properties. This can be the ultimate strain, the magnitude of the strength as well as the stress course after reaching the maximum strength. However, the stiffness or remaining stiffness after failure cannot be neglected since it determines

the resistance against bending and thereby the force distribution in the crush zone. The equal frond-wedge distribution seen for brittle variants is also experimentally acknowledged for thermoset matrix composites [43].

Table 11: Load division between fronds and debris wedge for plasticity and damage dominated material model settings

Material setting	**E** [MPa]	**R** [MPa]	**p_D** [1]	**s** [1]	**Frond force** [N]	**Wedge force** [N]	**Frond proportion** [1]	**Wedge proportion** [1]
Brittle	15600	200	0.035	0.25	29.4	35.1	0.46	0.54
↕	15600	200	1.0	0.25	54.7	39.4	0.58	0.42
	15600	250	1.0	0.25	61.9	37.6	0.62	0.38
Ductile	20855	330	1.0	0.25	86.9	25.7	0.77	0.23

The governing stress state of the material respectively laminae located near the centre of the laminate is subject to a combination of shear and compressive stresses, while the behaviour of the other laminae is dominated by transverse shear stresses. The time shift in the strain-time diagram of these laminae clearly demonstrates the wedge or v-shaped form of initiation of the crush zone (Figure 38). This shift has no further influence on the maximum effective plastic strain or strain rate (Figure 39).

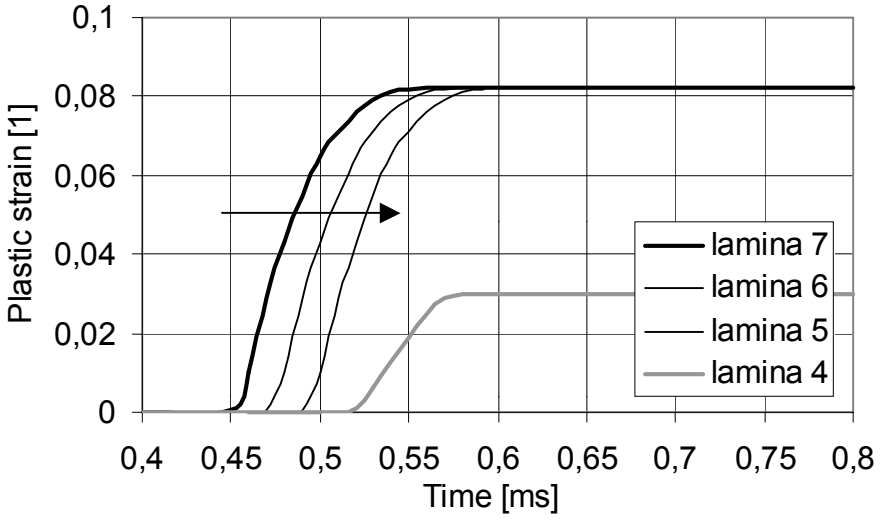

Figure 38: Plastic strain over time for different through the thickness positions within the composite laminae

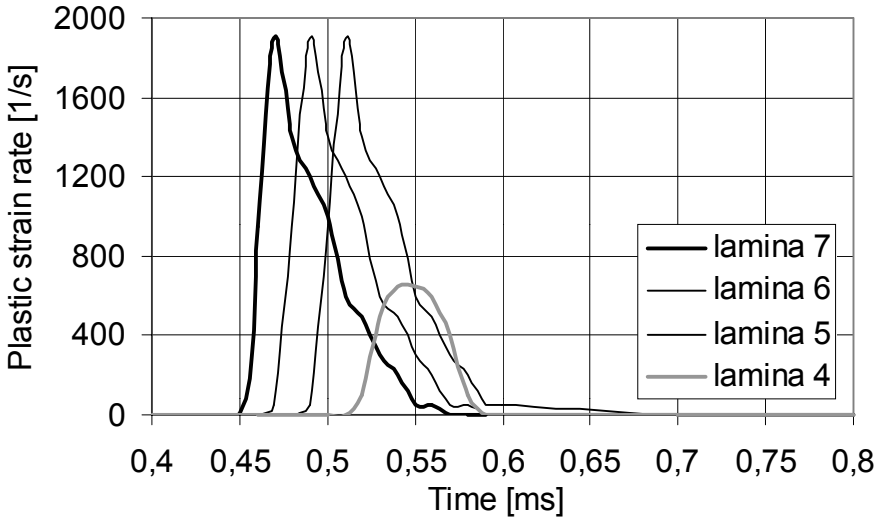

Figure 39: Plastic strain rate for different through the thickness positions within the composite laminae

Similar diagrams can be made for the matrix interface laminae. The major difference with the strain behaviour of the composite laminae is the fact that the matrix laminae reach the ultimate strain for all simulations. This maximum deformation is identified as transverse shear and is located within the thin matrix interphase laminae. The heterogeneous character of the strain distribution also explains the difference of the order of magnitude for the plastic strain rate of the matrix phase (Table 12).

Table 12: Order of magnitude of the governing plastic strain rates for the composite and matrix laminae at a constant impact velocity of 10 m/s

		Position	**Composite**	**Matrix**
$\dot{\varepsilon}_p^{max}$	[1/s]	Centre of laminate	~ $1.0\text{-}2.0_{10}^{3}$	~2.0_{10}^{3}
$\dot{\varepsilon}_p^{max}$	[1/s]	Intermediate	~$1.8\text{-}2.8_{10}^{3}$	~1.4_{10}^{4}
$\dot{\varepsilon}_p^{max}$	[1/s]	Outside	~$1.8\text{-}2.8_{10}^{3}$	~1.4_{10}^{4}

3.3.2 Identification of the material state in the crush zone

Two typical force-time diagrams and the shear stress plots at 1.0 ms are shown in Figure 40 to Figure 43. Results of the numerical investigation are compared and evaluated using the crash characteristics sustained crush stress and absorbed energy. The sustained crush stress is determined after finishing the initiation phase at t = 0.3 ms for the time interval 0.3 ms < t < 1.8 ms, which shows a constant force level.

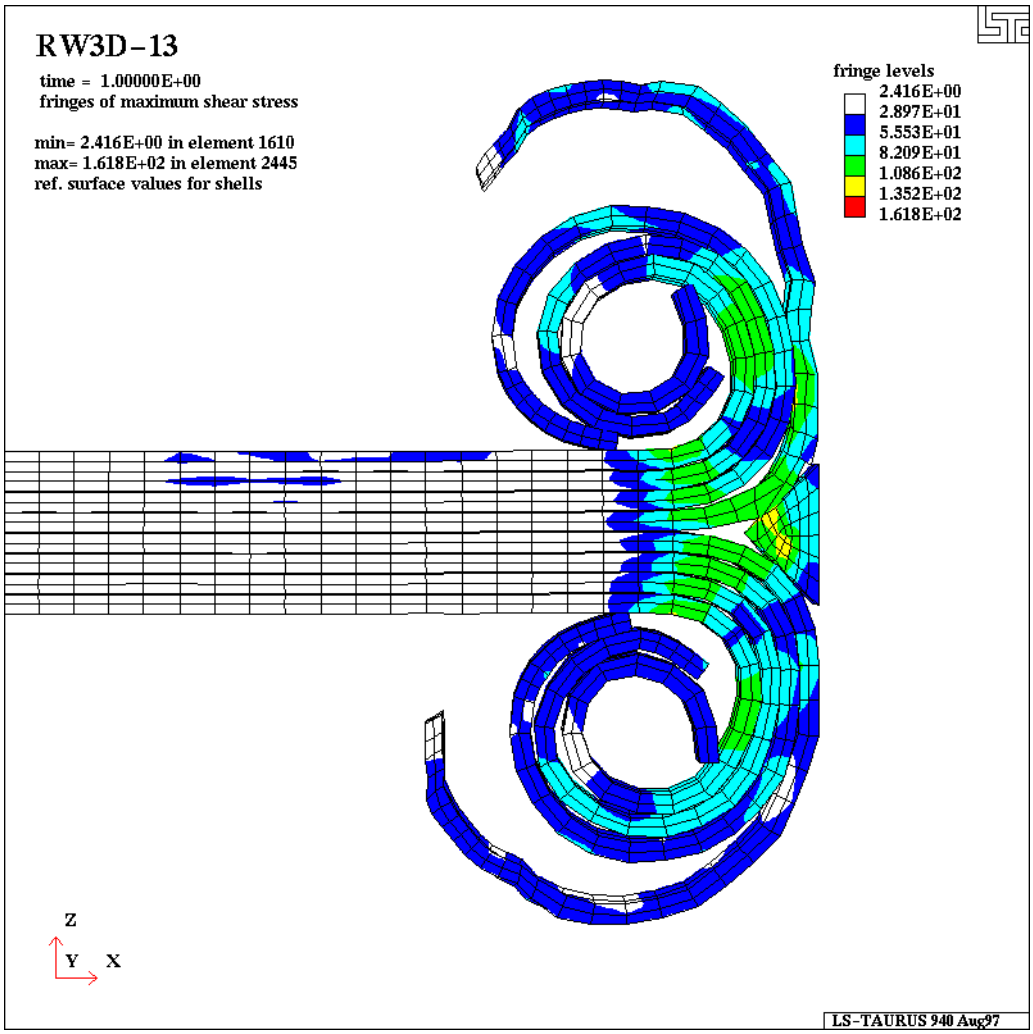

Figure 40: Shear stress at 1 ms for a plasticity dominated material

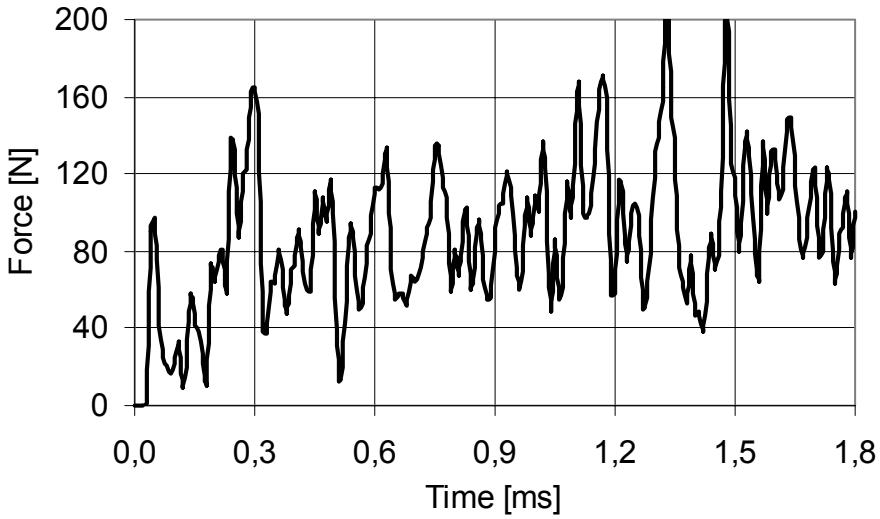

Figure 41: Force-time diagram for a plasticity dominated material

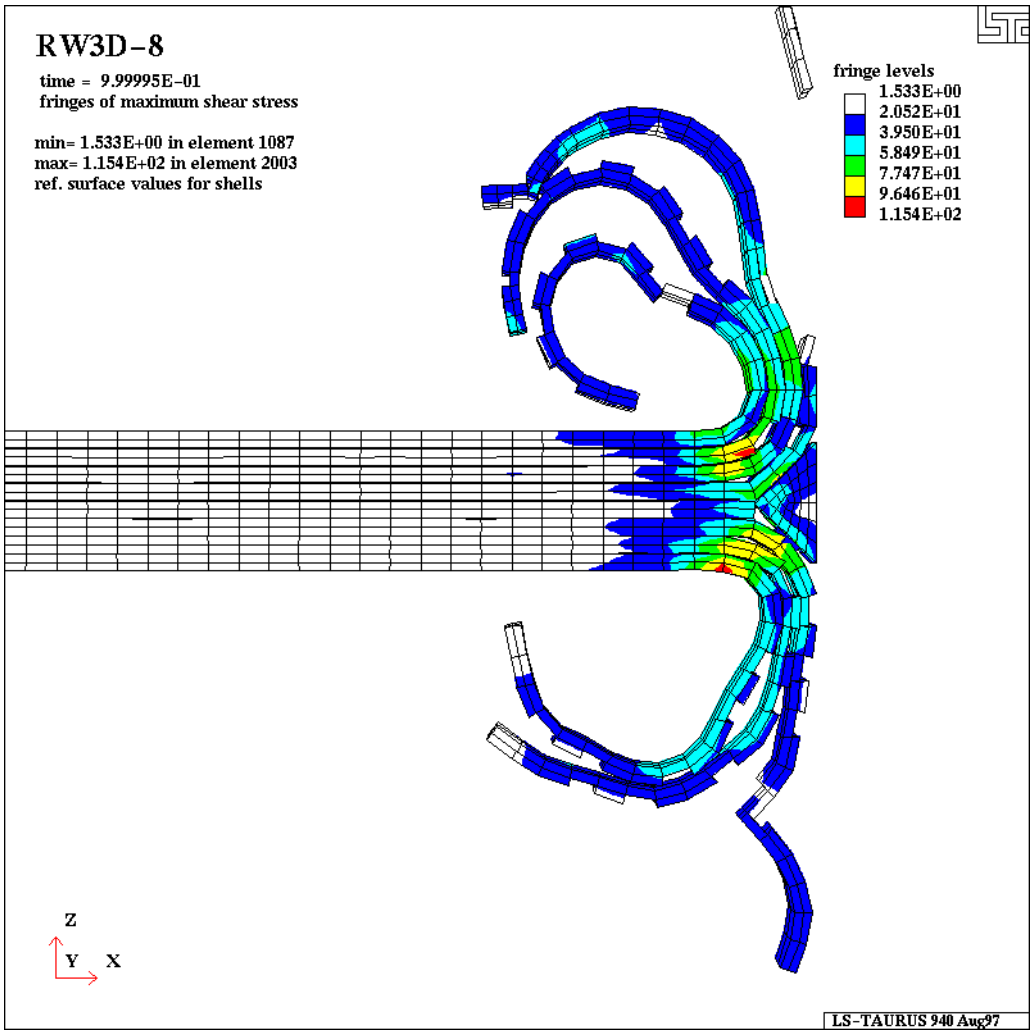

Figure 42: Shear stress at 1 ms for a damage dominated material

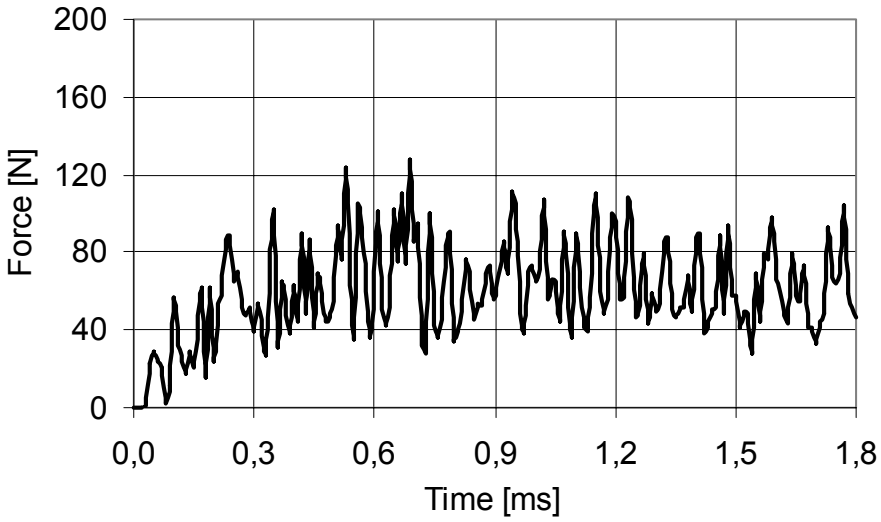

Figure 43: Force-time diagram for a damage dominated material

Having seen that the force transition distribution over wedge and fronds is mainly determined by strength and ultimate properties, the influence of these properties on the stress-strain diagram as well as on the sustained crush stress is discussed. Typical investigated stress-strain diagrams for the composite laminae can be seen in Figure 44. Parameters subject to this investigation are the strength R, the damage threshold p_D and the damage resistance s.

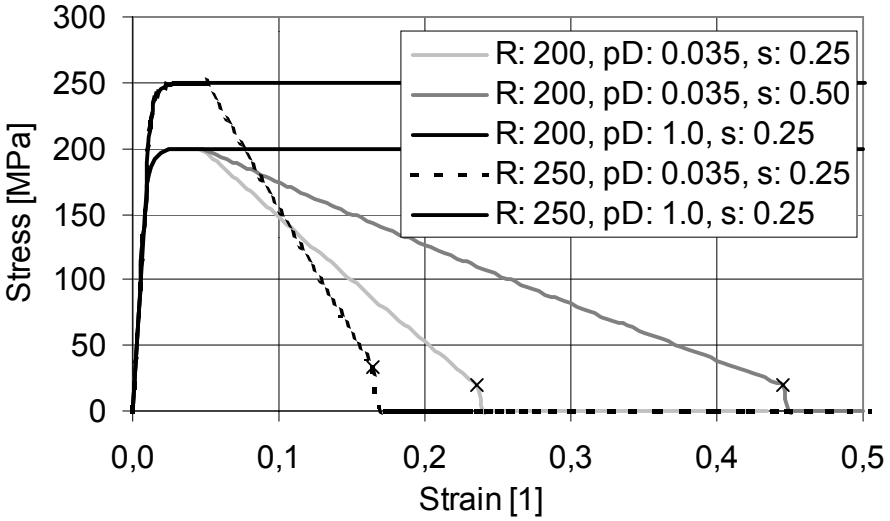

Figure 44: Stress-strain diagrams for different investigated composite lamina parameters (x denotes material failure)

Values for the damage threshold $p_D = 0.035$ represent the isotropic extrapolation of the actual experimental situation of GF/PET(A). Increased values of p_D delay the onset of damage, thus representing a more plastic behaviour. The damage resistance s determines the slope of softening in the stress-strain diagram. This is also a measure of ductility. When reaching a critical damage $D_c = 0.9$ the concerning element is eroded from the simulation. The actual governing maximum effective strain in the model is about 0.15. Material combinations with a damage onset or a critical damage larger than this strain show no eroded elements. The maximum strain limit is a result of the actual macroscopic bending radius, which depends on its turn on the actual stiffness σ/ε.

Experimental investigations on knitted GF/PET with different crystallization degrees show that the matrix crystallinity mainly influences the properties like ultimate strain and stress at ultimate strain. Both Young's modulus and strength vary within neglectable ranges relative to crush processes. The main parameter to consider this is

the damage resistance s. Smaller values for s, thus a stronger softening, represent a more crystalline state of the material.

The effect of PET crystallinity of K = 27.5 % respectively 52.4 % on the mechanical behaviour of the matrix laminae lies in different Young's moduli and ultimate failure strain (Figure 45). Especially this last parameter dominates the results of the numerical investigations of the matrix laminae, since the energy density is almost a linear function of the ultimate strain.

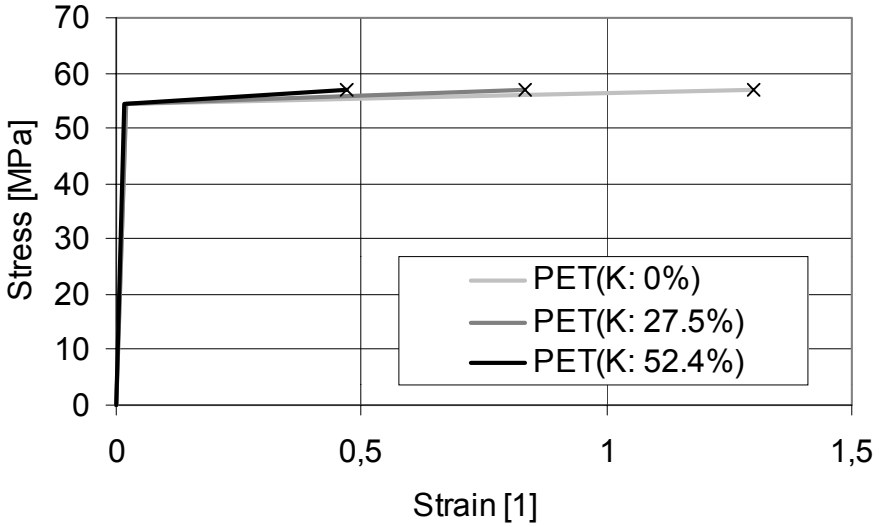

Figure 45: Stress-strain diagrams for PET matrix laminae with different crystallinities K (x denotes ultimate material failure)

Table 13 shows results of simulations with varying composite lamina properties and constant matrix lamina properties. Relative changes in absorbed energy equal those of the sustained crush stress, since the energy is determined from the force deflection diagram with a constant cross-sectional area for all simulations.

Consider the onset of damage p_D and the strength of the composite laminae. For increasing values of the strength with a constant value of $p_D = 1$ the mean sustained crush stress increases, while for $p_D = 0.035$ the mean sustained crush stress decreases. Apart from this difference, the 20 % difference in strength does not seem to come back in the crush response.

Table 13: Absolute and relative sustained crush stress and absorbed energy different composite lamina model properties

R_{cl}	p_D	s	σ_s	E_{tot}	σ_s'			E_{tot}'			Erosion
[MPa]	[1]	[1]	[MPa]	[J]	[1]			[1]			
200	0.035	0.25	28.1	1.278	1.00			1.00			Yes
200	0.035	0.50	34.6	1.574	1.23			1.23			Yes
200	1.0	0.25	40.9	1.861	1.46		1.00	1.46		1.00	No
250	0.035	0.25	25.0	1.136		1.00			1.00		Yes
250	1.0	0.25	43.3	1.970		1.73	1.06		1.73	1.06	No

Differences in composite lamina properties have an influence on the bending radius. This leads to a modified distribution of the force transition over fronds and wedge. Superposed with the leverage of the fronds, energy absorption characteristics alter non-linearly. The rise in strength is combined with a visible stronger softening in the numerical model, resulting in a smaller change of potential work of the material. Thus, the area under the stress-strain curvature – energy density - up to the governing strain determines the actual amount of absorbed energy. In these terms, the Young's modulus and strength have a limited contribution relative to post-failure characteristics like damage resistance and ultimate strain (Figure 44).

Shear deformation respectively delamination of the matrix in a mode II crack failure cause shear strains exceeding any physical realistic ultimate strain when following the relative displacement of the composite laminae. Simulations allowing the matrix interface to have an infinite ultimate strain fail to proceed by progressive crushing, acknowledging the existence of matrix rich layers between the stacked composite laminae.

A similar effect of the energy density distribution as observed for the composite laminae is also seen for the simulations with different matrix states (Table 14). However, these investigations of the matrix lamina with constant composite lamina properties can be related directly to the results. The reason for this is the complete erosion (and thus known absorbed energy) of the matrix interface, which is related to the known ultimate strain of 0.47 respectively 0.83 of the investigated PET states.

Table 14: Sustained crush stress and absorbed energy with different matrix lamina model properties

K(PET)	S(GF/PET)	E	σ_y	E_T	ε_u	$E'(\sigma,\varepsilon)$	σ_s	E_{tot}	σ_s'
[%]	[1]	[MPa]	[MPa]	[MPa]	[1]	[1]	[MPa]	[J]	[1]
27.5	0.50	2766	54.5	3.074	0.83	1.78	34.6	1.574	1.3
52.4	0.50	3748	54.5	5.489	0.47	1.0	26.7	1.214	1.0

The ratio of 1.78 to 1.0 for the specific energy absorption potential – i.e. area under the stress-strain diagram - between both matrix states is not directly reflected by the sustained crush stress. Knowing the energy absorption distribution between composite laminae and matrix laminae (Table 15), which is about 0.6 and 0.4 respectively, the same ratio of 1.3 to 1.0 as for the sustained crush stress is obtained. Here, the contribution of 2% for the wedge energy absorption is neglected.

Table 15: Absorbed energy and proportional distribution over the different materials; wedge (w), composite laminae (l) and matrix interface laminae (m)

R_l	p_D	s	σ_s	E_{tot}	E_w'	E_l'	E_m'
[MPa]	[1]	[1]	[MPa]	[J]	[1]	[1]	[1]
200	0.035	0.25	28.1	1.278	0.021	0.49	0.49
200	0.035	0.50	34.6	1.574	0.015	0.59	0.39
200	1.0	0.25	40.9	1.861	0.024	0.64	0.34
250	0.035	0.25	25.0	1.136	0.019	0.44	0.55
250	1.0	0.25	43.3	1.970	0.026	0.66	0.31

Results of simulations with variation of the frictional coefficients between separate laminae, laminae and wedge respectively impactor can be seen in Figure 46. The results are compared with the normalized sustained crush stress with a value of μ_i = 0.3 for all coefficients of friction as reference. Each marker demonstrates the influence of a change in one of the frictional coefficients, while the others remain constant.

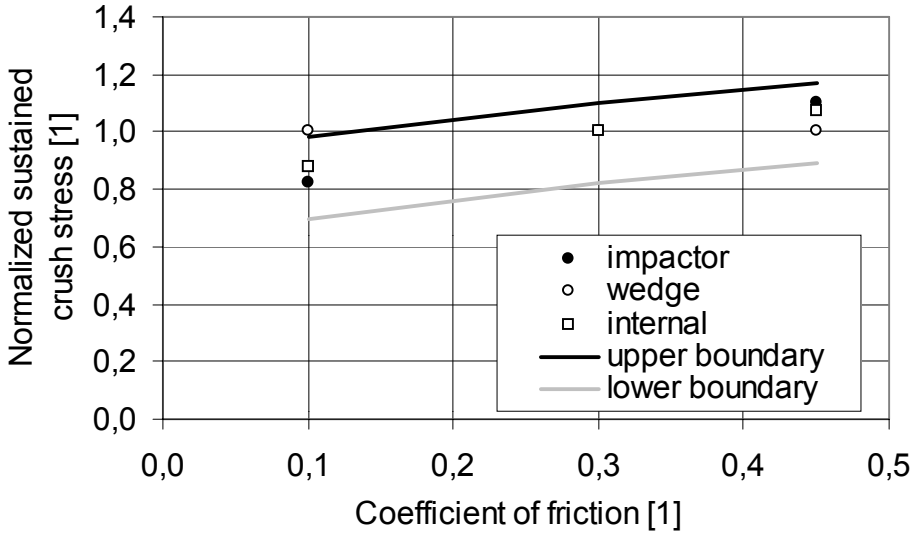

Figure 46: Normalized sustained crush stress response for different coefficients of friction for a ductile material state (pD: 1.0, s: 0.25, K:27.5 %)

Major differences in the magnitude of simultaneous present frictional combinations prevent progressive crushing. Increasing values of the friction between separate laminae and between laminae and the impactor have a positive effect on the sustained crush stress, with a maximum sensitivity of about 25 %. The sensitivity for changes in friction between wedge and laminae is neglectable. This can be explained by the used ductile material combination for this study. The post-failure behaviour of the fronds leads to a bending radius that minimizes the contact area between laminae and wedge and thus minimizes the influence of the coefficient of friction as well.

All simulations are evaluated for a constant impact velocity of v = 10 m/s. In reality the kinetic energy of the impactor mass is transferred to material deformation and thermal energy and the impactor velocity decreases (Figure 47). The strain rate and maximum strain rate are related to the impactor velocity via the geometry of the crush zone, and should thus decrease similarly.

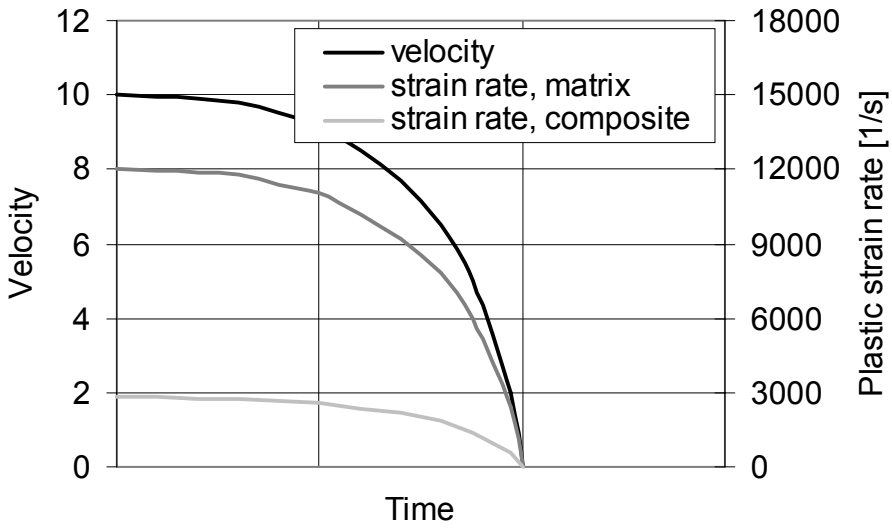

Figure 47: Impactor velocity and governing maximum plastic strain rates over arbitrary time

However, as the governing maximum strain rate decreases, the sustained crush stress remains constant during the mean crush phase. Another observed property is the logarithmic decrease of the sustained crush stress with increasing initial impactor velocity.

This is in contradiction with the higher values for the sustained crush stress for simulations with an increasing yield stress due to increasing strain rate effects. Thus another effect or effects apart from the strain rate, must be present. This typical behaviour is caused by the thermal properties of the material. The governing high strain rates allow a transformation of kinetic energy in thermal energy resulting in a more pronounced thermal softening. Some micrographs show air bubbles in the crush front area, which demonstrates that even for such a small time scale softening can occur. The non-isothermal processes occurring are adiabatic and frictional heating (Figure 48).

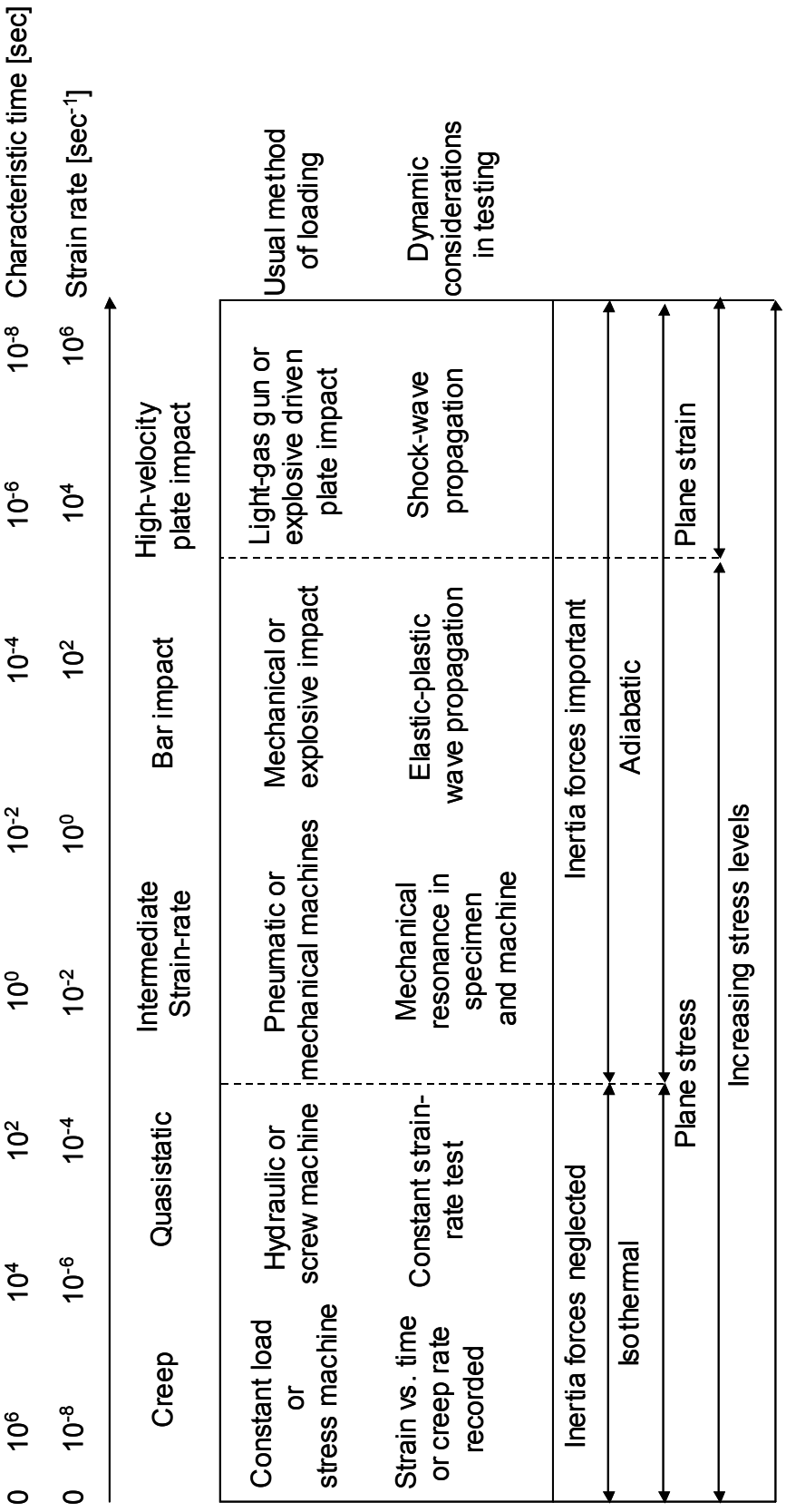

Figure 48: Aspects of testing under different test conditions [95]

4 A FE model for the simulation of crushing of thermoplastic composites

4.1 General considerations

4.1.1 The modelling approach

To describe the constitutive of law of a material usually three methods can be used [106]:

1. The microscopic approach
2. The thermodynamic approach
3. The functional approach

The microscopic approach stays at the non-homonogenized level and describes the mechanical behaviour of the structure at a microscopic level. The homogenization to macroscopic behaviour of the material is obtained by integration or averaging over a representative volume element. The heterogeneous and varying micro-geometric character of the investigated FRPs make this method too expensive to use in computations. For each state of fibre orientation and fibre distribution, even for a constant fibre-matrix combination, a new homogenization is necessary.

The thermodynamic approach uses macroscopic internal variables to describe the microscopic phenomena of a continuum. However, these variables have no direct correlation with experiments, which could mean that for one variable different types of tests need to be performed for each type of FRP.

The functional approach defines a material by characteristic functions in terms of macroscopic variables. These hereditary functions describe the relation between loading situation and material response of a representative volume element. Here, a model need not describe the material for all situations but can be different depending on the loading situation for which the model function and parameters can be determined from experiments. To do so, a classification of the material in internal geometry - fibre distribution, fibre orientation, matrix system, etc. - and type of response - fibre breakage, matrix yielding, lamina bending, etc. - for a specific loading situation - uniaxial tension, bending, progressive crushing, etc. - is needed.

The investigated knitted fabric and chopped GMT can be considered as quasi-isotropic with a certain degree of apparent stacked layers (Figure 1 & Figure 49).

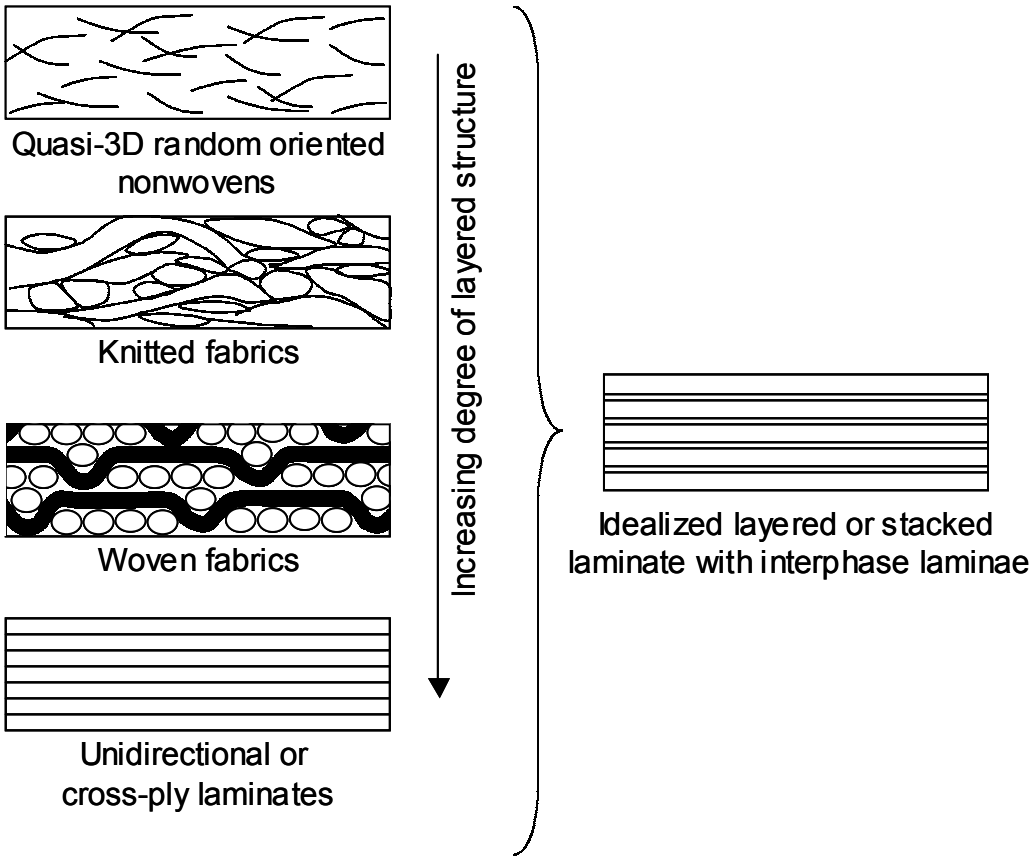

Figure 49: Schematic cross-sections of the layered structures of several types FRPs

The above figure also shows the increasing degree of the layered status for a laminate made from GMT up to unidirectional FRPs. All these types of FRPs are heterogeneous and can be idealized by a stacked laminate with the presence of matrix interphases. These interphases are a necessary part of the model, since they allow the material to response in the progressive crushing failure mode with lamina bending and transverse shear between the subsequent laminae.

The anisotropy factor of materials like knitted fabrics is relatively small compared to unidirectional fibre reinforced composites and is caused by a deviation from the idealized isotropic state. The matrix interphases have an isotropic character while the laminae are stated to be orthotropic.

Whereas for GMT the orthotropy comes from the fibre reorientation due to matrix flow during press forming, the orthotropy respectively orthorhombic symmetry for KFRPs comes from the shape of the knit [91]. An idealized knitted fabric has an equal number of repeating loops in course and wale direction per unit length. The size of one loop is determined by the knitting machine and defines the smallest representative volume element (Figure 50). A common loop size is 6 x 6 mm^2 with a lamina

thickness of 0.25 to 0.3 mm. It seems logical to assume a plane stress situation with this ratio between in-plane and thickness size, but the knowledge of the stacked nature and its influence on the failure behaviour shows the necessity of a more complex formulation.

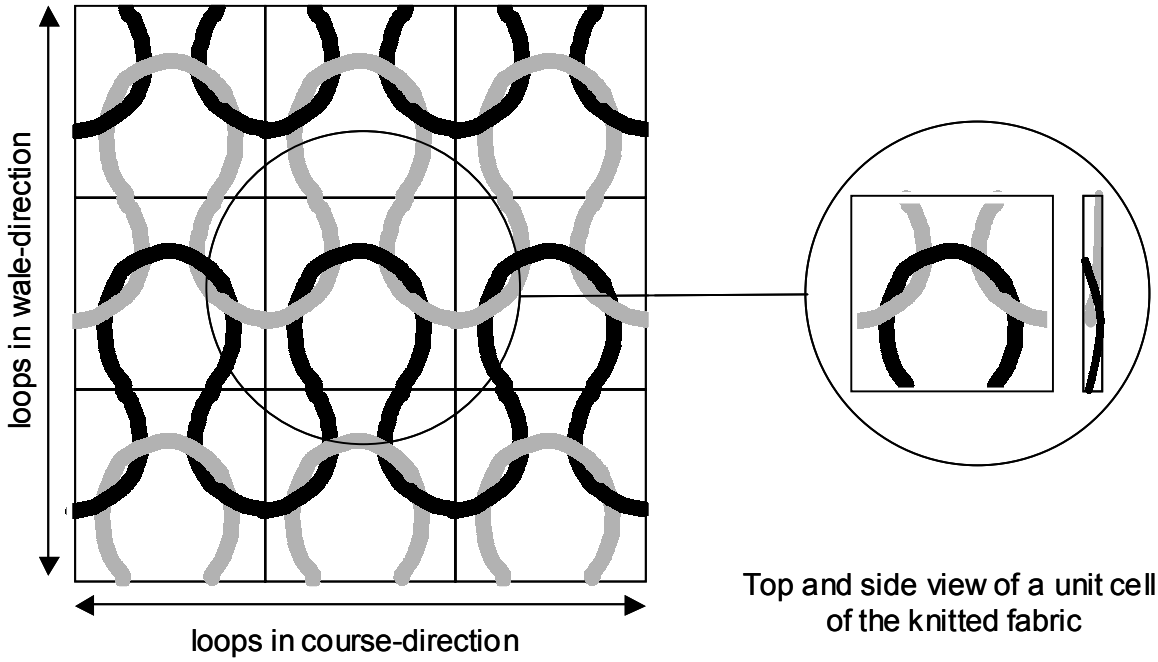

Figure 50: Definition of a 2D unit cell for a plane weft knitted fabric

A limitation for the formulation of a suitable model is the correlation between the geometry and the explicit loading situation resulting in progressive crushing. Progressive crushing can only occur for structures, which have a suitable initiator for crushing and a longitudinal axis along which crushing can occur. Therefore, an explicit identification of the loading situation is necessary to determine whether progressive crushing is the governing process or not. The such deduced material model is a phenomenological model with a priori information about the layered material structure, the behaviour during crush loading as well as a division on beforehand into crushing and non-crushing behaviour.

4.1.2 Material and/or numerical model ?

To geometrically model lamina bending mechanisms like transverse shear between laminae, friction and delamination correctly, it is necessary to use solid elements. This costs a large amount of computation time even when modelling simple structures.

Instead of the detailed – micromechanical - modelling of these mechanisms, one could also take into account their result on the mechanical and thermal behaviour and consider using shell elements despite the drawback concerning an accurate material deformation description. Especially the representation of the influence of delamination and internal friction is affected by this choice. An additional argument is the complicated determination of the mechanical properties of layered FRPs in thickness direction. The decision to use shell or solid elements has a major influence on the model response within the FE-simulation.

Figure 51 shows principle spatial discretization possibilities for the FE-modelling of progressive crushing. The most simple case is assuming a plane stress state as is usually done for thin walled structures (Figure 51 a).

However, the progressive crushing is dominated by transverse shear, which makes it necessary to extend this formulation with the terms for transverse shear σ_{23} and σ_{31} as is state-of-the-art in the available crashworthiness material models. A formulation for shell elements with the assumption that σ_3 is small or negligible without neglecting the transverse shear components in the failure model, seems to be a possible compromise.

Another possible representation is the so-called stacked shell model (Figure 51 c). Apart from the large number of elements – shell elements and beams or joints - , the determination of the properties of the shells and beams is unclear. Also the overlap of the beam cross-section with the shell thickness and the absence of σ_3 causes questions about the model accuracy.

Solid elements have the advantage of the availability of the complete stress tensor as well as an accurate density representation. Nevertheless, mechanisms during progressive crushing like delamination respectively crack opening are a result of the non-constant through the thickness properties within the laminate. The resulting central delamination for example can only be described by using several finite elements in laminate thickness direction (Figure 51 e). This and the fact that small solids with full integration are needed to describe bending properly, leads to considering computation times.

A solution for the modelling of the experimental governing deformation mode is to simplify the representation of the lamina bending mode by modelling only one frond instead of two (Figure 51 b & d). Due to the fact that the sustained crush stress for the lamina bending mode can be coupled to the experimental obtained transverse shear strength and the influence of the wedge can be neglected, this simplification seems to be admissible.

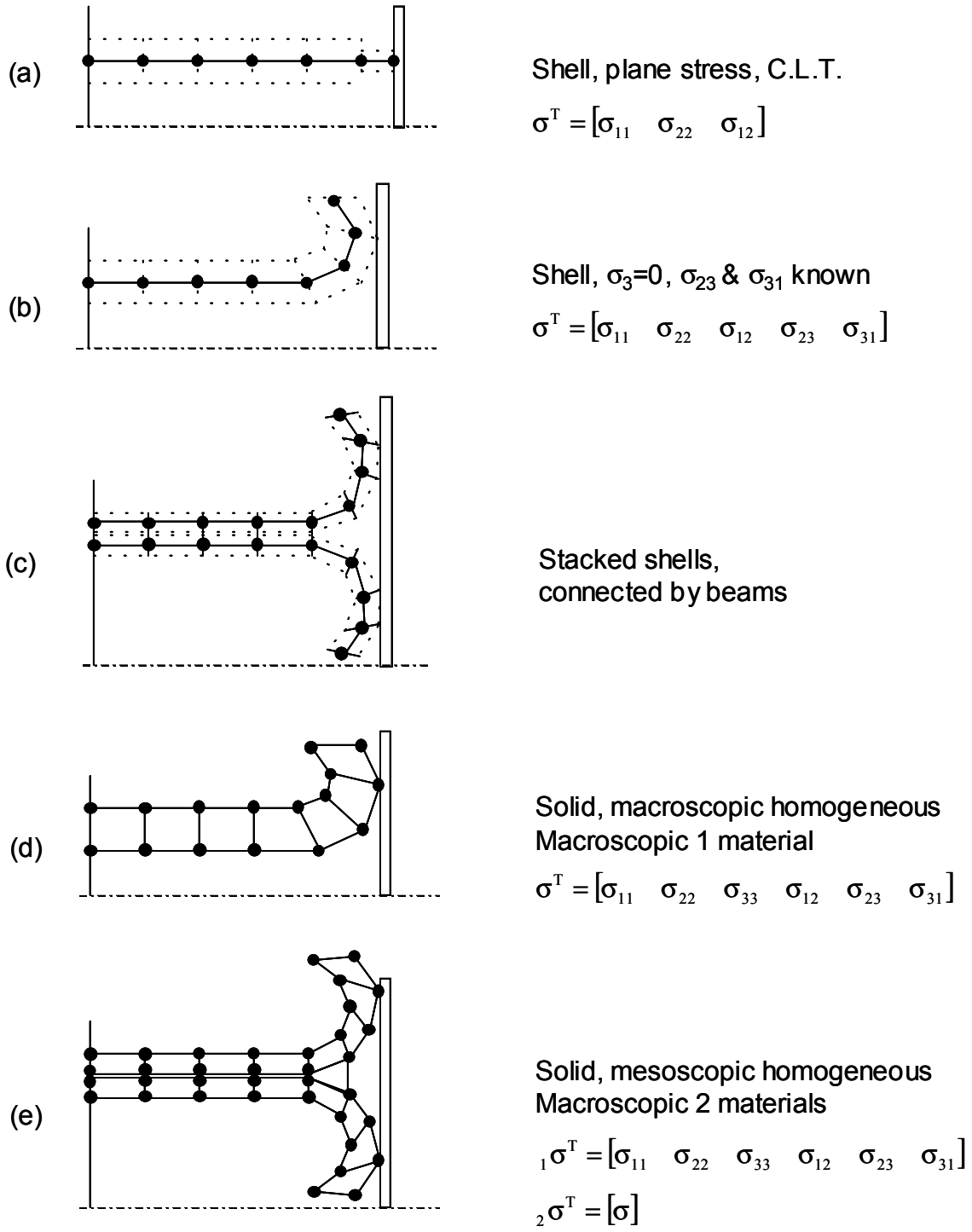

Figure 51: Spatial discretization possibilities in FE in case of progressive crushing

Other failure modes than lamina bending combined with transverse shear are not considered within the formulation of the model. The experimental and numerical investigations showed that for the progressive crushing of the laminate the bending

failure mode is dominated by transverse shear of subsequent laminae resulting in delamination. The thus arising non-linear strain distribution restricts the modelling to theories for laminated composites, which take into account this behaviour [54].
Similar to the Classical Laminate Theory, which takes into account the summation of the separate laminae, the material model is defined in the local or material coordinate system with the transformation between local and global coordinate system defined by

$$C_g = TC_l \tag{4.1}$$

with
C_g: Global lamina stiffness
C_l: Local lamina stiffness
T: Transformation matrix.
The stiffness matrix components of the laminate are then calculated by summation over the thickness:

$$C_{ij}^{L} = \frac{1}{t^{L}} \sum_{k=1}^{n} C_{ij}^{k} t^{k}, \; t^{L} = \sum_{k=1}^{n} t^{k} \tag{4.2}$$

with

C_{ij}^{L}: homogenized stiffness matrix components of the laminate L,

C_{ij}^{k}: stiffness matrix components of the k^{th} lamina,

t^{k}: thickness of k^{th} lamina,

n: number of laminae,

t^{k}, t^{L}: k^{th} lamina and total laminate thickness, respectively.

This approach allows describing the laminate stiffness behaviour with composite laminae and matrix laminae separately. Nonlinear transverse shear deformations can be incorporated into common shell and solid element theories by assuming that the mean transverse shear angle γ of a nonlinear shear deformation course equals the angle γ' for a macroscopic linear shear course (Figure 52). The so obtained assumed deformation state serves to calculate the stress situation in each lamina. This formulation also gives the basis for the relation between experimentally obtained

properties of the laminate $C_g^{L'}$ and the formulation for the properties of the laminae $C_{ij,1}^k$ and $C_{ij,2}^k$, e.g. [107].

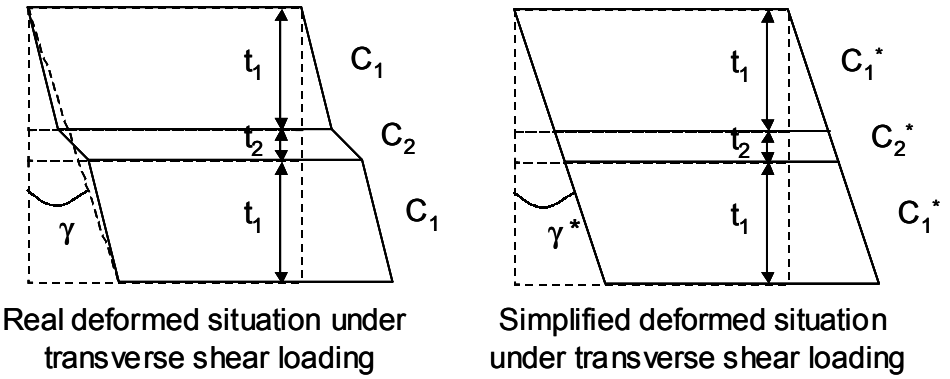

Figure 52: Modelling principle of the variable shear deformation; $|C_1| > |C_2|$, $t_1 > t_2$ and $\gamma = \gamma^*$

4.2 Basic formulation

4.2.1 The different states of the material model

As mentioned before, a material model for the description of progressive crushing should consist of two different phases. First, it should contain a basic formulation to take into account the stiffness and strength behaviour for the elastic state and non-crushing loading situations and second, a phase with special features to represent progressive crushing (Figure 53).

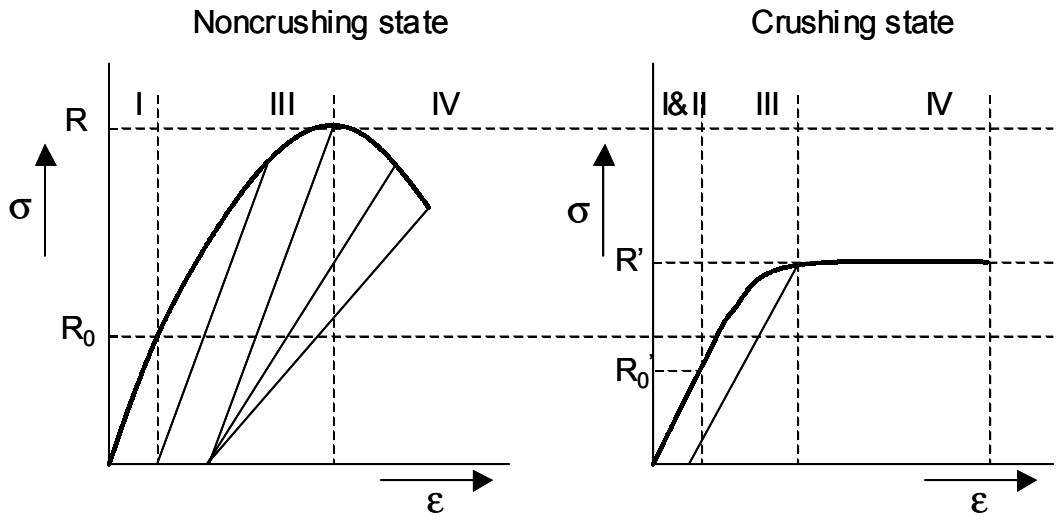

Figure 53: Stress-strain diagram for uniaxial loading (left) and a predamaged state in progressive crushing (right) with R_0 the initial yield stress, R the strength and R_0* and R* the respective softened values

As seen in Chapter 2, failure of KFRP due to uniaxial loading is based on accumulated damage by elastic and plastic matrix deformations, fibre-matrix interface failure and fibre respectively fibre bundle failure. Here, interface failure, e.g. fibre pull-out, is a mechanism with permanent deformation.

A constitutive law that can describe the result of these typical FRP failure mechanisms for noncrushing loading situations, is based on coupled plasticity and damage with the following phases (Figure 53 a):

I an orthotropic elastic part without permanent strains to represent reversible fibre and matrix deformations,

II softening of the predamaged laminate,

III an irreversible part with permanent strains, representing matrix plasticity, fibre-matrix interface failure and micro-cracks, and

IV an irreversible part, with fibre or fibre bundle failure leading to macroscale fracture.

A possible additional phase could be defined as unloading. The slope of unloading depends on the actual loading phase. In phase III with both matrix deformations and fibre-matrix interface failure the matrix part causes the plastic contribution. In phase IV only fibre pull-out and fibre failure occurs, which can be interpreted as a contribution to the damage. A fibre, which is pulled out of the matrix, is not able to retain its original state when unloaded and does not contribute to the plastic

deformation. Due to this fact the unloading slopes converge on a constant maximum of plastic strain.

The crushing state is characterized by the presence of a predamaged zone defined as phase II (Figure 53 b). This zone has the effect of scaling the relevant strengths and moduli from R_0 and R to R_0' and R'. The model post-failure behaviour is assumed to be constant and represent the sustained crush stress level, which can be interpreted as a continuous failure passing through the material. An ultimate failure phase in case of crushing, which has a numerical character is discussed in Chapter 4.3.4.

4.2.2 Modelling the noncrushing state

The model contains an orthotropic formulation of the elastic part. This serves to describe the orthotropic stiffness behaviour of stretched KFRPs. Furthermore, failure is represented by an anisotropic plastic damage law. The division into reversible and irreversible parts is realized by assuming that the strain tensor can be divided into an elastic and a plastic part

$$\varepsilon = \varepsilon_e + \varepsilon_p \tag{4.3}$$

with ε_e the elastic strain tensor and ε_p the plastic strain tensor. Similar as in the model originally proposed by Kachanov [49] anisotropic damage is introduced within the relationship between the effective stress $\hat{\sigma}$ and true stress σ with a damage operator M - similar to equation (3.7) -

$$\hat{\sigma} = M\sigma \tag{4.4}$$

The damage operator M consists of coefficients D_{ij} representing the accumulated damage in the normal and shear material directions of the orthotropic system. In this context, σ is defined for solid elements as

$$\sigma^T = [\sigma_{11} \quad \sigma_{22} \quad \sigma_{33} \quad \sigma_{12} \quad \sigma_{23} \quad \sigma_{31}] \tag{4.5}$$

and for shell elements as

$$\sigma^T = [\sigma_{11} \quad \sigma_{22} \quad \sigma_{12} \quad \sigma_{23} \quad \sigma_{31}] \tag{4.6}$$

The elastic domain is bounded by a yield function f defining the shape and size of the failure surface in stress space. This yield function f can be chosen similar to failure criterions typical for FRPs. However, the yield function respectively failure criterion should take at least into account the anisotropy in the strength behaviour by distinguishing between the different material directions – ij - as well as compression and tension - c,t -:

$$f_{ijc,t} = f(\sigma_{ijc,t}, R_{ijc,t}, D_{ijc,t}) \tag{4.7}$$

A typical shape of the failure surface $f_{iic,t}$ of the investigated knitted fabrics can be seen in Figure 54. The failure surface consists of subsurfaces defined for each quadrant separately. A description of the failure surface is included in paragraph 4.3.2.

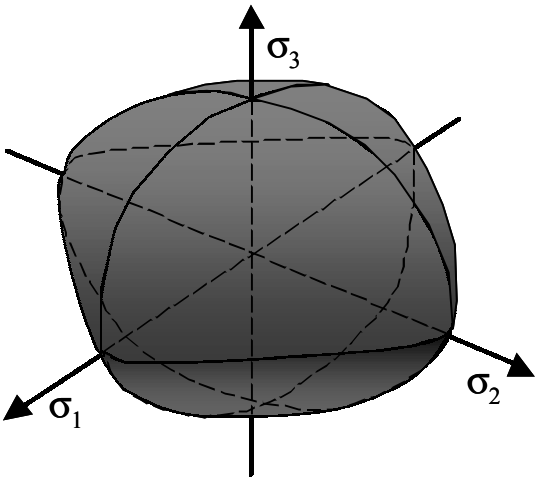

Figure 54: Failure surface $f_{iic,t}$ of knitted GF/PET

The evolution of damage ($D_{ijc,t}$) as well as the shape ($\sigma_{ijc,t}$) and size ($R_{ijc,t}$) of the failure surface $f_{ijc,t}$ determine the ultimate failure and are basically defined by the type of FRP. Investigations on prestretched GF/PET knitted fabrics show a relationship between the stiffnesses, strengths and the prestretching degrees λ_w/λ_c [16]. The prestretching degree, and thus stiffness and strength, are fixed in the manufacturing process and are assumed constant during loading. The actual modulus and strength for a certain prestretching degree can be determined experimentally and used for simulation

without implementing the microscopic relation between fibre distribution and mechanical behaviour, e.g. Figure 55.
However, the model should be able to describe the result of the pre-stretching on the anisotropy. Whereas the stiffness anisotropy is satisfied by the intrinsic orthotropic formulation, the damage evolution and shape of the yield surface need explicit parameters. Due to the structure of the knit an interaction between course and wale direction exists. This is acknowledged by experimental observations of fracture paths (Figure 56).

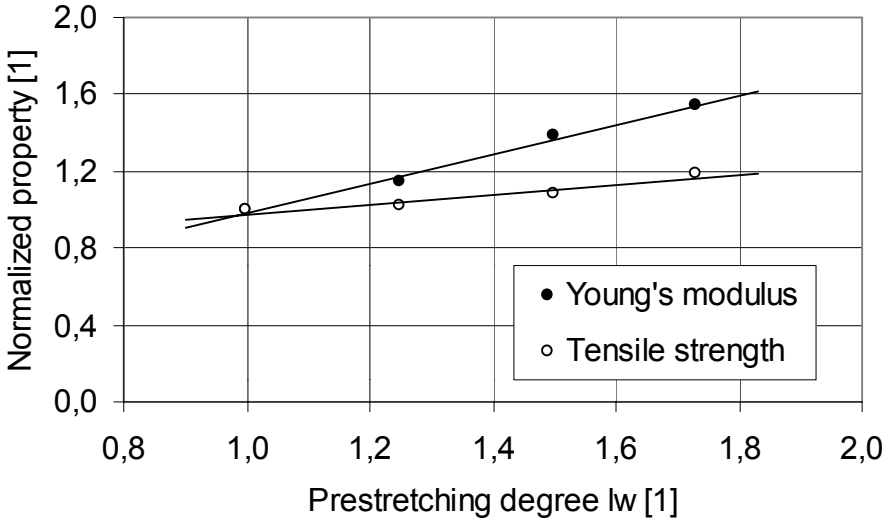

Figure 55: Relation between prestretching degree in wale direction λ_w and matching normalized strength and Young's modulus

The smooth loop geometry of the knit reinforcement offers guidance for a crack along the interface between the fibre bundle or loop and matrix. Typical fracture paths follow the heads, feet or sides of loops (Figure 56a,c). The cracks proceed wavingly resulting in damage in course direction for wale tensile loading and vice versa. Thus, uniaxial loading in one direction also influences the damage state in the other direction.

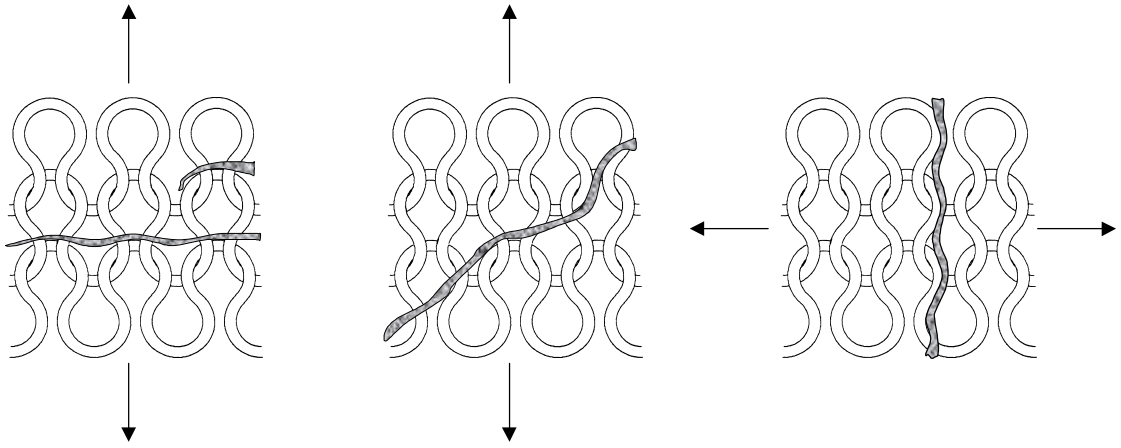

Figure 56: Fracture paths for tensile loading in wale (a,b) and course (c) direction

Depending on the degree of interaction between loops and subsequent laminae, the fracture path can cross several rows or columns of loops (Figure 56b). However, this is only seen for thin laminates, which are certainly heterogeneous, even for in-plane uniaxial loading. Though the orientation of the loops is three dimensional, the orientation in thickness direction is much smaller than in the 1-2-plane. Therefore, the coupling is limited to the course and wale direction respectively 1- and 2-direction while damage coupling between laminae is neglected.

Thus, the model is enhanced by introducing a definition of anisotropic damage, which describes coupled damage evolution in wale and course direction. Coupling is implemented by a proportionality factor α_{ii} in the anisotropic damage operator M. The proportionality factor α_{ii} describes the amount of this coupling with the assumption that wale and course show the same or similar failure behaviour. For simplicity, Ω is defined as a vector containing the components M_{ii} of the diagonal of M and reads as

$$\Omega = \begin{bmatrix} \frac{1}{(1-D_{11}-\alpha_{11}D_{22})} \\ \frac{1}{(1-D_{22}-\alpha_{22}D_{11})} \\ \frac{1}{1-D_{33}} \\ \frac{1}{1-D_{12}} \\ \frac{1}{1-D_{23}} \\ \frac{1}{1-D_{31}} \end{bmatrix} = \begin{bmatrix} \frac{1}{(1-D^{*}_{11})} \\ \frac{1}{(1-D^{*}_{22})} \\ \frac{1}{1-D_{33}} \\ \frac{1}{1-D_{12}} \\ \frac{1}{1-D_{23}} \\ \frac{1}{1-D_{31}} \end{bmatrix} \tag{4.8}$$

With the coupled damage coefficients defined as

$$1-D^{*}_{ii} = (1-D_{ii}-\alpha_{ii}D_{jj}) \tag{4.9}$$

For high pre-stretching degrees the anisotropy degree increases while the interaction tends to approach zero. In this case the proportionality factors α_{ii} also approaches zero and D_{ii} and D^{*}_{ii} are the same. Here, uniaxial tests are sufficient to determine D_{ij}, whereas for coupling biaxial tests or subsequent nondestructive uniaxial tests in wale and course directions are needed. The evolution of the damage depends on the sequence and magnitude of the governing failure mechanisms with an exact formulation depending on the specific material loading and unloading behaviour.

The reversible part of the model represents the elastic region without damage or plasticity, thus D = 0 or Ω = 1. The second and third part consist both of plastic and damage processes and cannot be so clearly divided as shown in Figure 53. Nevertheless, this seems to be a useful assumption.

The yield surface is represented by a failure criterion and has a major influence on the quantitative results for the noncrushing and crushing state. Formulations for appropriate failure surfaces are discussed in Chapter 4.3.

4.2.3 Modelling the crushing state

The experimental state of progressive crushing of a material is initiated by a trigger, which is a geometric measure to guarantee the progressiveness. A similar initiation has to be present in the FE-model as well. This is usually arranged in the form of a local

reduction in material thickness. Another possibility is introducing a flag denoting a softening state in a numerical trigger before loading. Figure 57 shows a sketch with the most important material phases during crushing.

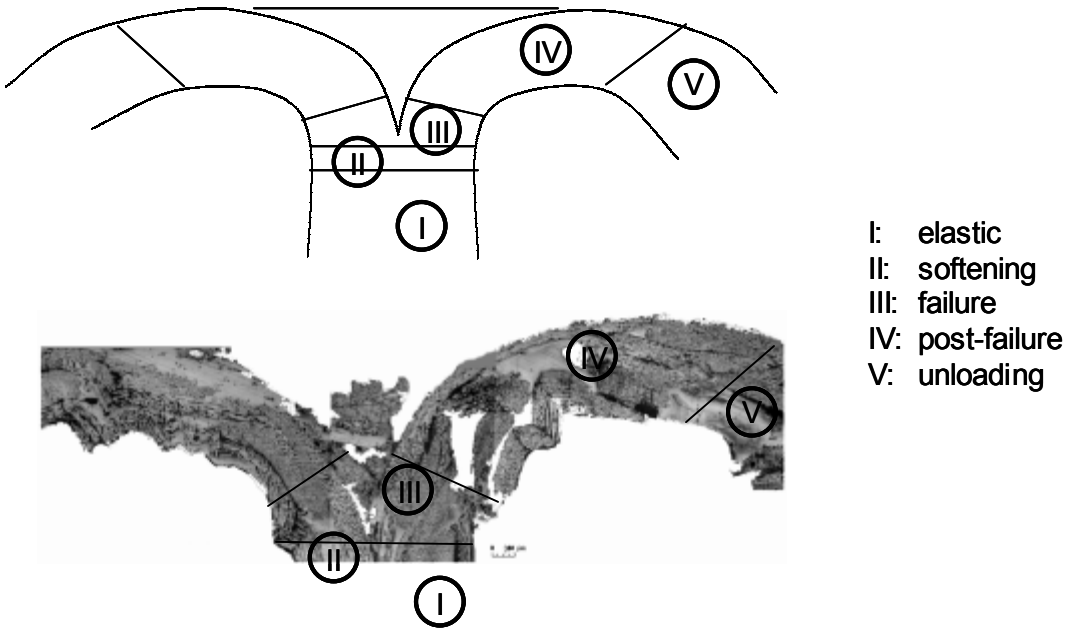

Figure 57: Different material loading phases during crushing

These phases are arranged in the order of the successive loading situations, i.e. an elastic region, a softening zone, a failure and post-failure zone and the unloading of damaged material respectively:

- Elastic

This region is exactly the same as the elastic noncrushing state with orthotropic elasticity and with the same yield limits.

- Softening

The softening zone is a zone in which a gradient from undamaged material of the elastic zone to damaged material of the failure zone governs the process. For thermoplastics this predamaging can be interpreted as a thermal softening due to temperature increases. Mechanisms causing this thermal activity are plastic deformation and friction within the crush zone. The transition between the elastic and failure zone is not likely to be infinitely steep but increases gradually. The softened or predamaging zone of the still elastic part near the crush zone is bounded in size with a characteristic length. This length is among others determined by the height of the temperature increase in the crash zone as well as the thermal conductivity and specific heat capacity of the TPC.

- Failure

The failure zone is the real crush zone in which failure of the matrix interphases is initiated leading to delamination. This is the location of the maximum material loading with the highest strain rates. Due to frictional effects between impactor and material, the loading state is one of superposed compression and transverse shear. The compressive state is more or less distributed evenly over the laminate, while transverse shear mainly occurs within the matrix interphases. The dominating failure is transverse shear, thus enabling a relative sliding between the laminae.

- Post-failure

The post-failure region is an extension of the failure region in which the governing failure mechanisms continue on a relative constant level due to the approximately constant bending radius. This zone has a function of load transition between impactor and the failure zone.

- Unloading

After concluding the contact with the impactor, the laminae unload. The amount of permanent strain determines the view of the deformed state of the damaged laminae and acknowledges the existence of a plastic process.

In terms of a homogenized FE-model the above material states lead to a description for the model of which the transverse shear behaviour is presented graphically in Figure 58.

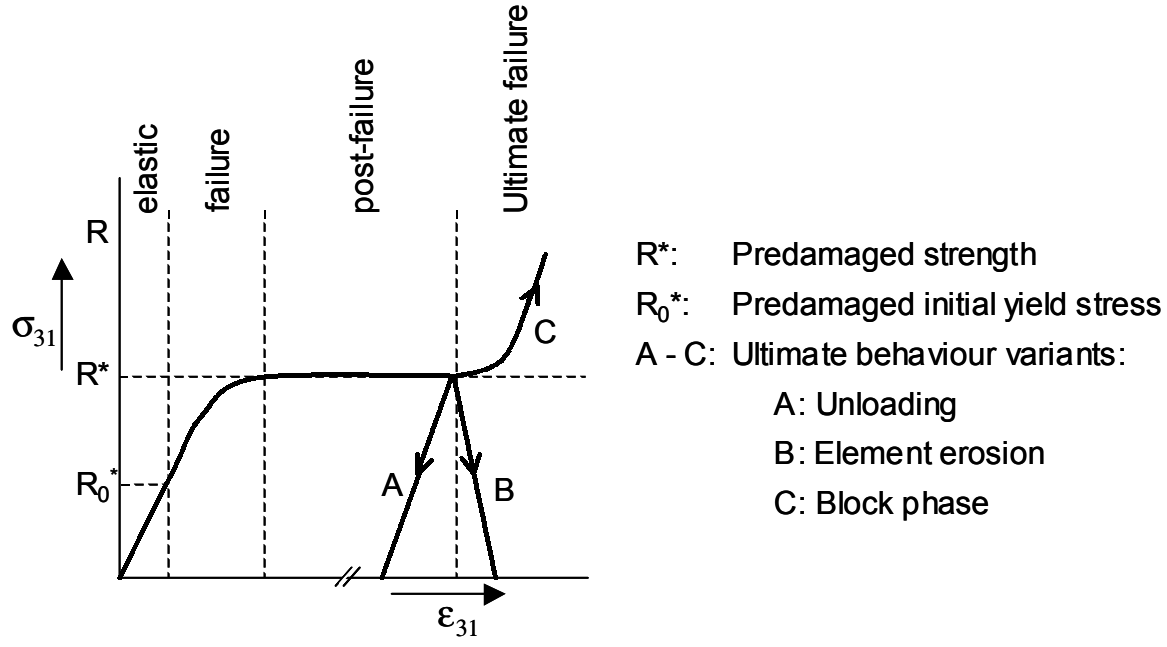

Figure 58: Transverse shear behaviour of the softened crushing state with different ultimate behaviour variants

Both the original yield stress R_0 and the maximum stress R are scaled to R_0* and R* respectively. Theoretically, the scaling factor for both parameters can be different, but this would complicate the model considerably without major consequences for the result of only simulation. Mechanisms, material behaviour and properties influencing the scaling are discussed in Chapter 4.3.3. The effects of size of the predamaging zone and the ultimate behaviour depend on the numerical implementation and are discussed in chapter 4.3.3.

4.3 Modelling the failure behaviour

4.3.1 Choice of an appropriate failure criterion

With the introduction and development of FRP-materials, several models for the description of their elastic and strength behaviour have been proposed. Since no verified failure criterions for the dynamic strength behaviour of FRPs exist, applicability of static criterions with certain modifications for dynamic strengths is assumed.

Over the years many of these failure criteria have been formulated and discussed in literature [73],[74],[75],[76],[77],[78]. A representative choice of criteria with basic properties is summarized in Table 16. Most of the developed failure criteria are designed for unidirectional (UD) or layered multidirectional (MD) FRP.

Table 16: Survey of failure criteria determining type and application potential [77]

Criterion		Mode	Interaction term		Use
		Distinction	Analytic	Experimental	
Maximum stress/strain	[75],[77]	+	-	-	UD
Tsai-Hill, Hoffman	[79],[80]	-	+	-	UD
Tsai-Wu	[81]	-	-	+	UD
Hashin-Rotem	[82]	+	-	-	UD
Chang Chang, Hashin	[83]	+	-	-	UD
Truncated maximum strain	[84],[85]	+	-	-	MD
Cuntze, Puck	[88]-[90]	+	-	+	UD

Some of these failure criteria are based on formulations in the stress space [79],[80],[81],[82],[83], strain space [84],[85] or strain-energy space [86]. The transformation between stress or strain space does not change the principal character of a failure criterion, nor the physical or eventually non-physical basis. A recent significant development for UD-FRP is the formulation of failure criterions based on the description of the loading situation on distinct fracture planes [87],[88],[89],[90]. In the following, selected examples of widely used failure criteria are presented. The discussed criteria represent the groups of maximum stress/strain criteria, Hill-type criteria, quadratic criteria with failure mode distinction and tensor polynomial criteria.
In principle, all these criteria describe the beginning of failure and not the failure process with large deformations.
The maximum stress criterion is non-interactive and considers the maximum tensile and compressive stress components of the local material axes, see Equation (4.10). Due to its simplicity this criterion is widely used, but contains neither information of off-axis strengths nor has any physical relation with the material. However, due to the fact that unequal strengths on the principle material axes are covered, it is an effective criterion for uniaxial load situations in these directions.

$$\begin{aligned} -R_{11c} \le \sigma_{11} \le R_{11t} \\ -R_{22c} \le \sigma_{22} \le R_{22t} \\ -R_{33c} \le \sigma_{33} \le R_{33t} \\ |\sigma_{12}| \le R_{12} \\ |\sigma_{23}| \le R_{23} \\ |\sigma_{31}| \le R_{31} \end{aligned} \tag{4.10}$$

A criterion for the description of the yielding of ductile metals (!) with an anisotropic failure surface was proposed by Hill [79] and is based on the generalization of the distortional energy criterion of von Mises. In the proposed form tensile and compressive strengths are assumed to be equal. The basic criterion is of a quadratic form with the coefficients F, G and H characteristic values for the normal strengths and L, M and N for the shear strengths:

$$\begin{aligned} 2f(\sigma_{ij}) = F(\sigma_{22}-\sigma_{33})^2 + G(\sigma_{33}-\sigma_{11})^2 + H(\sigma_{11}-\sigma_{22})^2 + \\ + 2L\sigma_{23}^2 + 2M\sigma_{31}^2 + 2N\sigma_{12}^2 = 1 \end{aligned} \tag{4.11}$$

Based on the questionable assumption that an analogy exists between plastic yielding of anisotropic metals and failure of fibre reinforced polymers a lot of modifications leaded to a number of clones, e.g. [81],[80]. By dividing the stress space in quadrants, unequal strengths can be represented by different strength parameters for each quadrant. The resulting failure surface represents an ellipsoid respectively an ellipsoid section centered at the origin. In the original formulation, the ellipsoid is rotated allowing higher off-axis stresses than the strength values on the principal axes. This effect can partially be suppressed by superposing this criterion with the maximum stress criterion and thereby truncating the failure envelope with flat planes perpendicular to the material axes.
A typical representative of a quadratic failure criterion with mode distinction is the Hashin failure criterion, of which a modification by Chang and Chang is implemented in a material model for the simulation of composites, i.e. [50]. This criterion distinguishes between the following failure modes:

Fibre tension failure (Mode I):

$$\frac{\sigma_{11}^2}{R_{11t}^2}+\frac{\sigma_{12}^2+\sigma_{31}^2}{R_{12}^2}=R \tag{4.12}$$

Fibre compression failure (Mode II) :

$$\sigma_{11}=-R_{11c} \tag{4.13}$$

Matrix tension failure (Mode III):

$$\frac{(\sigma_{22}+\sigma_{33})^2}{R_{22t}^2}+\frac{\sigma_{12}^2+\sigma_{31}^2}{R_{12}^2}+\frac{\sigma_{23}^2-\sigma_{22}\sigma_{33}}{R_{23}^2}=R \tag{4.14}$$

Matrix compression failure (Mode IV):

$$\left(\frac{R_{22c}^2}{4R_{12}^2}-1\right)\frac{\sigma_{22}+\sigma_{33}}{R_{22c}}+\frac{(\sigma_{22}+\sigma_{33})^2}{4R_{23}^2}+\frac{(\sigma_{23}^2-\sigma_{22}\sigma_{33})}{R_{23}^2}+\frac{\sigma_{12}^2+\sigma_{31}^2}{R_{12}^2}=R \tag{4.15}$$

The basic idea to define a failure criterion for each governing failure mode limits this criterion to materials, for which such defined modes exist respectively are known, i.e. unidirectional reinforced composites only.
Tensor polynomial are best represented by the Tsai-Wu failure criterion [81], which is generally defined in contracted notation (i,j=1,2,…,6) as

$$F_i\sigma_i + F_{ij}\sigma_i\sigma_j = R \tag{4.16}$$

Here, the F_i and F_{ij} are strength tensors composed of the different strengths along the principal material axes. A reduction of equation (4.16) by assuming transverse isotropic laminates and plane stress gives:

$$\begin{aligned}&\sigma_{11}\left(\frac{1}{R_{11t}}-\frac{1}{R_{11c}}\right)+\sigma_{22}\left(\frac{1}{R_{22t}}-\frac{1}{R_{22c}}\right)+\frac{\sigma_{11}^2}{R_{11t}R_{11c}}+\frac{\sigma_{22}^2}{R_{22t}R_{22c}}-\\&-C\frac{\sigma_{11}\sigma_{22}}{2\sqrt{R_{11t}R_{11c}R_{22t}R_{22c}}}+\frac{\sigma_{12}^2}{R_{12}^2}=R\end{aligned} \tag{4.17}$$

Tensor polynomial criterions are best-fit curvatures through strength values on the principle material axes. Since these fits have no physical correlation with the material, certain choices for the interaction coefficient C may cause unwanted rotations or elongations of the ellipsoid. Some of the rotational positions lead to values for the off-axis stresses, which are higher than the strength in the principle material axes (Figure 59). A known effect is that a decrease in transverse tensile strength would lead to an increase of the biaxial compressive strength. These kinds of problems exist for all interactive quadratic and tensor polynomial failure criteria and are discussed in detail by reference [74].

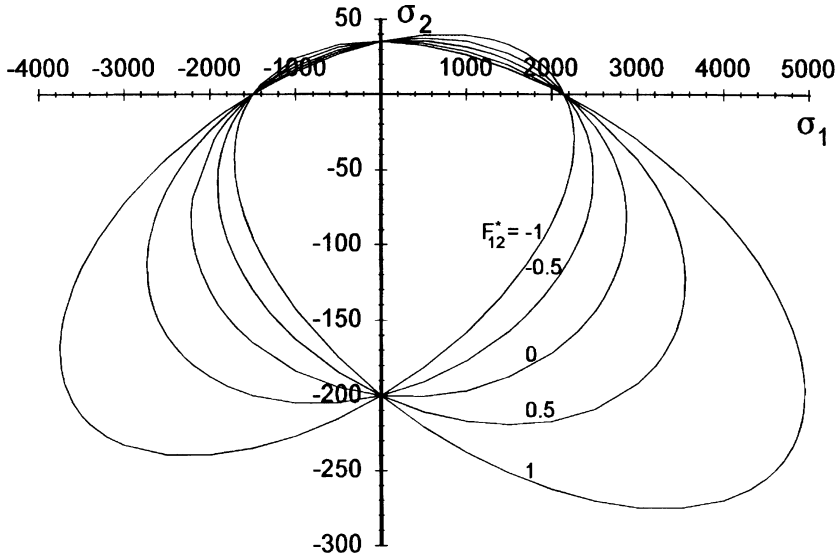

Figure 59: Influence of the interaction coefficient F_{12} on the failure surface in the σ_1-σ_2-plane [77]

At this point, the choice for an appropriate formulation of a failure criterion reduces to two possibilities. First, the fact that the orthotropic model is based on the extension of isotropic materials, leads to the conclusion to use a criterion, which is also generalized to orthotropy respectively anisotropy. Such a criterion would be similar to Hill's theory, which is based on failure by a single mechanism. However, failure of FRPs – independent of the anisotropy - is certainly not based on the same single mechanism, but on several different mechanisms.

Second, the limited availability of material strength parameters prefers phenomenological criteria, which are best-fit curvatures through the available data, i.e. the unidirectional strengths on the main material axes. In order to prevent non-physical properties of the failure surfaces, a priori material information must be implemented or estimated.

The failure behaviour of the investigated materials or material class of quasi-isotropic thermoplastic composites, determines basic features of the failure criterion. The criterion should take into account different values for compressive, tensile and shear strengths and distinguish between the main material axes. Furthermore, results of tensile tests on knitted fabrics show a strength anisotropy, which insignificantly deviates from an elliptic surface formulation (Figure 60). This anisotropic behaviour increases with increasing fibre orientation due to pre-stretching, which the failure criterion should also be able to describe.

In extension to the formulation of a model with a priori distinguishing between the loading situation noncrushing respectively crushing, a similar differentiation between the crushing failure modes can be made with a failure criterion for each failure mode.

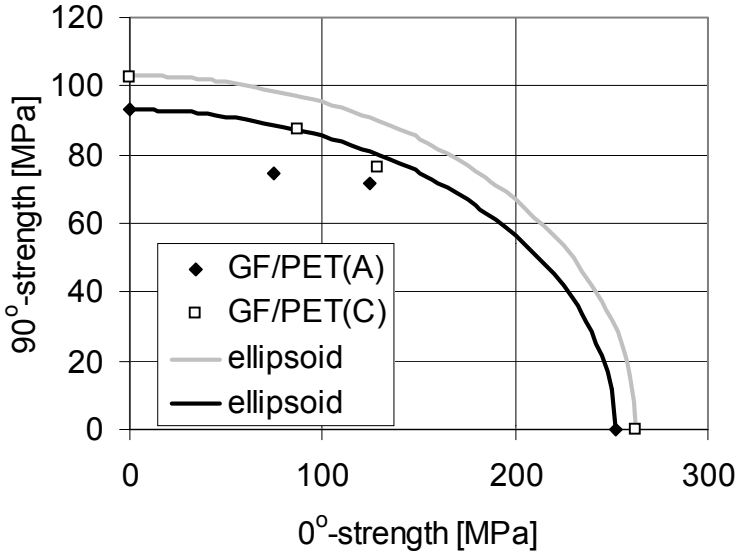

Figure 60: Strength anisotropy of the investigated knitted fabrics with ellipsoidal estimations for the σ_1-σ_2-plane

4.3.2 A failure criterion for layered quasi-isotropic TPCs

Both the experimental and the numerical investigations show that the heterogeneous character of the material during crushing cannot be ignored, since the non-linear shear behaviour caused by the matrix interphases dominates the failure mechanism. Within the layered formulation of shell or solid element both mesoscopic material phases are treated separately. Similarly, a different failure criterion for matrix laminae and mesoscopic composite laminae is proposed:

- The matrix interphase, which is an unreinforced thermoplastic polymer, fails by yielding. Here, the analogy to Hill's theory for anisotropic yielding seems to be sufficient, since the failure mechanism of unreinforced TPs – shear yielding - are similar to those of ductile metals [105]. This criterion holds for the noncrushing state as well as the crushing.
- For the composite laminae a non-interactive criterion with variable exponent is chosen. With this choice the crushing and noncrushing state can be described with the same basic criterion, stating that the softening in crushing only influences on the size of the surface, not influence the shape.

To formulate the criterion for the composite laminae, the relevant stress components during progressive crushing have to be identified. As discussed before, progressive crushing only initiates if certain boundary conditions apply. The structural buckling strength must be higher than the crush strength and the structure must have a longitudinal axis along which crushing proceeds. For the investigated materials this means that the structure usually has a tubular cross-section with axial, radial and transverse normal and shear stresses (Figure 61).

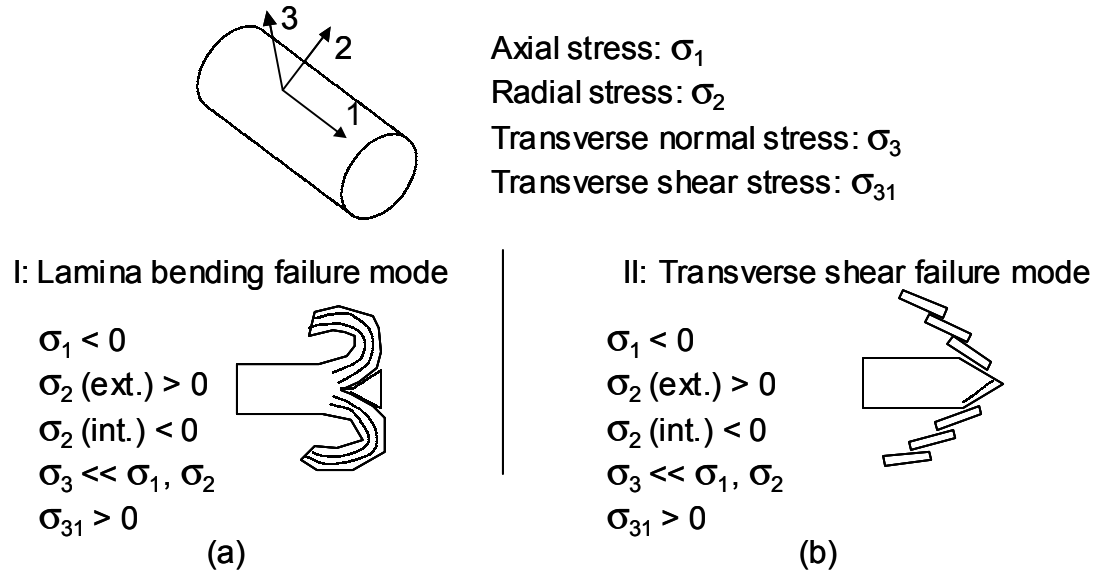

Figure 61: Loading situation during progressive crushing with (a) lamina bending failure mode and (b) transverse shear failure mode (ext.: external frond, int. internal frond)

Knitted fabrics fail in a combined lamina bending and transverse shear stress failure mode with the main point on lamina bending. The delaminated layers have transverse cracks, which do not fully cross the layer due to the resistance of the meshed loops. A best curve fit through the relevant uniaxial strengths to describe the failure surface for the lamina bending mode can be written as follows:

$$f_I = \frac{\sigma_{11}^m}{R_{11c}^m} + \frac{\sigma_{22}^m}{R_{22c,t}^m} + \frac{\sigma_{33}^m}{R_{33}^m} + \frac{\sigma_{31}^n}{R_{31}^n} \qquad (4.18)$$

Here, the normal strengths R_{33t} and R_{33c} are assumed to be equal in tension and compression. In conformity with the governing loading situation the axial, radial,

transverse and shear stresses are represented. Both the axial and radial stress state remain in the elastic region. Due to the shear deformation and delamination of the matrix laminae the transverse normal stresses R_{33} in the subsequent lamina are small and their contribution is not discussed further.

The question of how to describe the deviation from the ellipsoidal failure surface is solved by the introduction of the variable exponent. The exponent of the usual ellipsoid can be replaced by a variable m for normal stresses respectively n for shear stresses. In the case of plane stress a value for the exponent m = 2 would give the elliptic surface. Smaller values of m deform the surface to the origin of the σ_1-σ_2-plane while increasing values of m deform the surface to a rectangular shape with smooth edges (Figure 62).

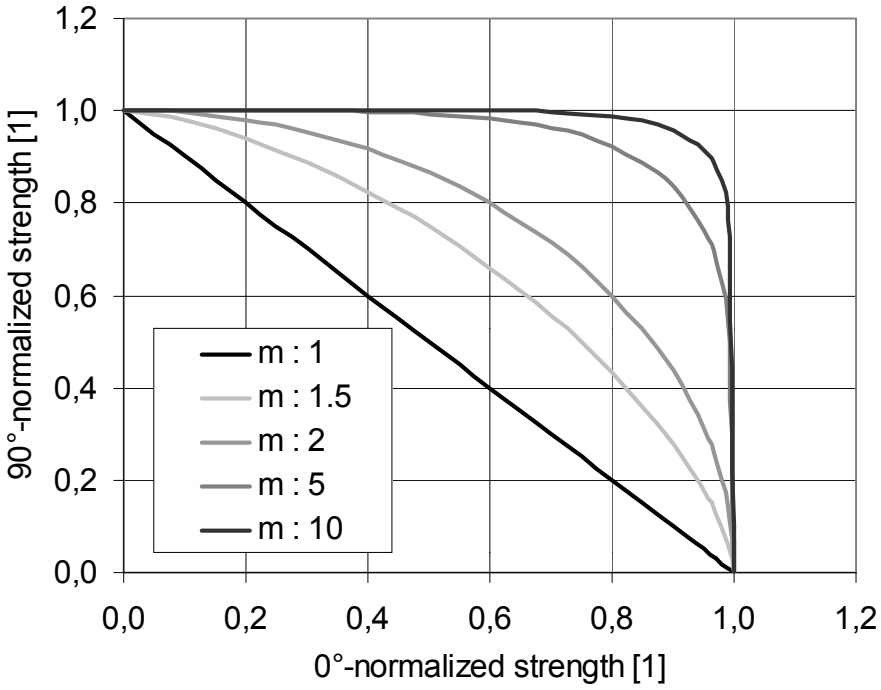

Figure 62: Strength anisotropy in 1st quadrant of the normalized σ_1-σ_2-plane

In progressive crushing other loading situations do not occur and need not to be considered. Another topic is the orientation of the stacked laminae. The above criterion implies an identical local and global coordinate system. For the isotropic state of the material this is irrelevant, but a criterion for quasi-isotropic materials with unequal orientations for the local and global axes should also contain the transverse shear

strength σ_{23} (Equation (4.19)). In case the main lamina orientation is along the longitudinal axis, this shear strength $\sigma_{23} = 0$ and equation (4.19) turns to (4.18).

$$f_I = \frac{\sigma_{11}^m}{R_{11c}^m} + \frac{\sigma_{22}^m}{R_{22t}^m} + \frac{\sigma_{33}^m}{R_{33}^m} + \frac{\sigma_{31}^n}{R_{31}^n} + \frac{\sigma_{23}^n}{R_{23}^n} \tag{4.19}$$

For the noncrushing state, a supplementary division into quadrants is necessary to take into account the correct strengths for each quadrant. Here, uniaxial transverse tension or compression failure ($R_{33c,t}$) is assumed not to occur before transverse shear failure R_{31} or R_{23} and is therefore not considered in the following examples. In addition, transverse shear failure does not occur under biaxial tension. This results in a failure criterion for the noncrushing state as follows:

$$f_{tt} = \frac{\sigma_{11}^m}{R_{11t}^m} + \frac{\sigma_{22}^m}{R_{22t}^m} + \frac{\sigma_{12}^n}{R_{12}^n} \tag{4.20}$$

$$f_{cc} = \frac{\sigma_{11}^m}{R_{11c}^m} + \frac{\sigma_{22}^m}{R_{22c}^m} + \frac{\sigma_{31}^n}{R_{31}^n} + \frac{\sigma_{23}^n}{R_{23}^n} \tag{4.21}$$

$$f_{tc} = \frac{\sigma_{11}^m}{R_{11t}^m} + \frac{\sigma_{22}^m}{R_{22c}^m} + \frac{\sigma_{12}^n}{R_{12}^n} \tag{4.22}$$

$$f_{ct} = \frac{\sigma_{11}^m}{R_{11c}^m} + \frac{\sigma_{22}^m}{R_{22t}^m} + \frac{\sigma_{12}^n}{R_{12}^n} \tag{4.23}$$

The acronyms cc, tt, tc, ct indicate the compression-compression, tension-tension, tension-compression and compression-tension quadrant, respectively. Theoretically, the coefficients of the exponents could be different for each quadrant, but due to material symmetry the coefficients for the failure surfaces f_{tc} and f_{ct} are chosen equal and slightly smaller than those of f_{tt}, e.g. for the investigated knitted GF/PET(A) these parameters can be determined as $(m,n)_{tc} = (m,n)_{ct} = 1.2$, $(m,n)_{tt} = 1.5$ and $(m,n)_{cc} = 2$. The normalized failure surface with these values in the σ_1-σ_2-plane is demonstrated in Figure 63.

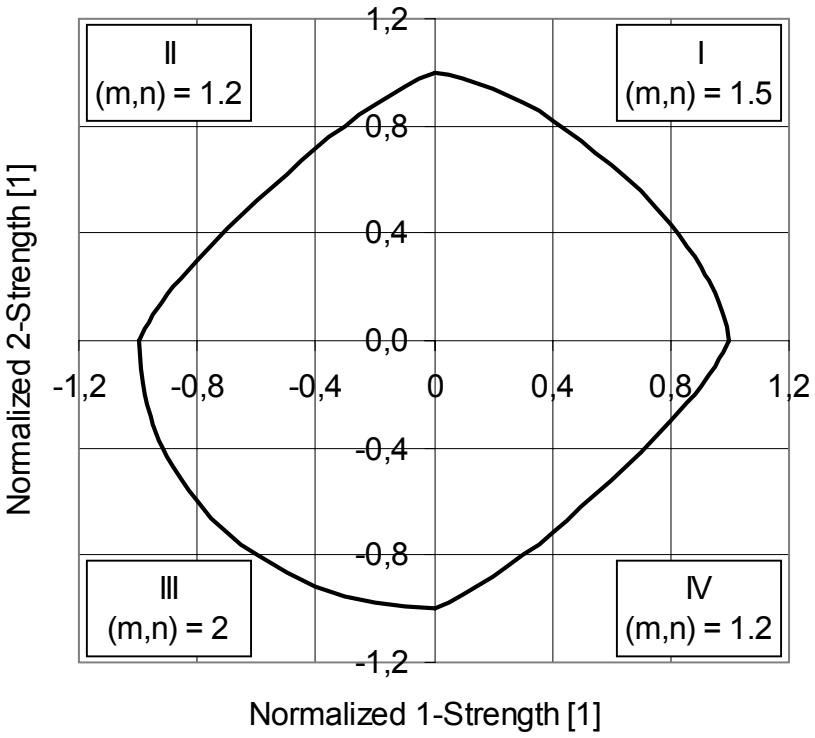

Figure 63: Normalized failure surface in the σ_{11}-σ_{22}-plane for the investigated knitted GF/PET(A)

4.3.3 Scaling effects for progressive crushing

Preceding the crush front is a thermal softening zone, which weakens the boundary of the material in the elastic region and allows the progressive nature of the crushing. The gradient is localized to a small material volume of which the size is bounded by the amount of adiabatic and frictional heating, the thermal conductivity λ and the specific heat c_p of the respective material.

This mechanism could be described with a nonlocal similar formulation. The basic idea in a nonlocal continuum is that the stress at a point in the body is dependent on the strains of neighbouring points in addition to the strain at the point [104]. Here, the stress at a point is dependent on the thermal properties, or the effects on the mechanical properties, in the neighbouring points and the characteristic distance from the heating zone.

The crush front model is the simplest form of a nonlocal model with the distance determined by one finite element along the longitudinal axis, e.g. [50]. The

compressive strength of the material of this one element is softened by a constant factor to a level, which should represent the sustained crush stress.

For the mesoscopic model the predamaged zone is assumed constant through the laminate thickness. The determination of the size of this softening zone is thus limited to the determination of a characteristic length l_T of the softening zone in crush direction. Due to the fact that adiabatic heating is a localized process and the short time to conduct heat – fractions of milliseconds – l_T is assumed to be bounded to a very small material region directly near the crush zone.

In fact, the influence of the actual magnitude of l_T is neglectable, since the presence not the size of softening zone enables the progressive nature of the crushing while the amount of softening determines the crush response.

Due to the fact that usual mesh sizes are larger than l_T, the thermal or softening gradient is chosen as a constant softening factor by scaling the transverse shear yield stress and strength of the mesoscopic phases by R_{31}^{0*}/R_{31}^{0} and R_{31}^{*}/R_{31} - or R_{23}^{0*}/R_{23}^{0} and R_{23}^{*}/R_{23} depending on the crush direction – respectively. The thus enlargened difference between in-plane properties and transverse shear properties force the material to fail in the desired lamina bending mode.

In simulation, the magnitude of softening respectively the value of R_{31}^{*L} determines the constant level for the crush response. R_{31}^{L} is the quasi-static experimentally determined transverse shear strength of the laminate, which is related to the sustained crush stress via the initial impact velocity v_0 (Figure 64). The experimental investigations show a linear connection between the mean sustained crush stress and the logarithmic initial impact velocity with a decrease in sustained crush stress for increasing test velocities. This effect is observed for several thermoplastic composites with each TPC having a different slope.

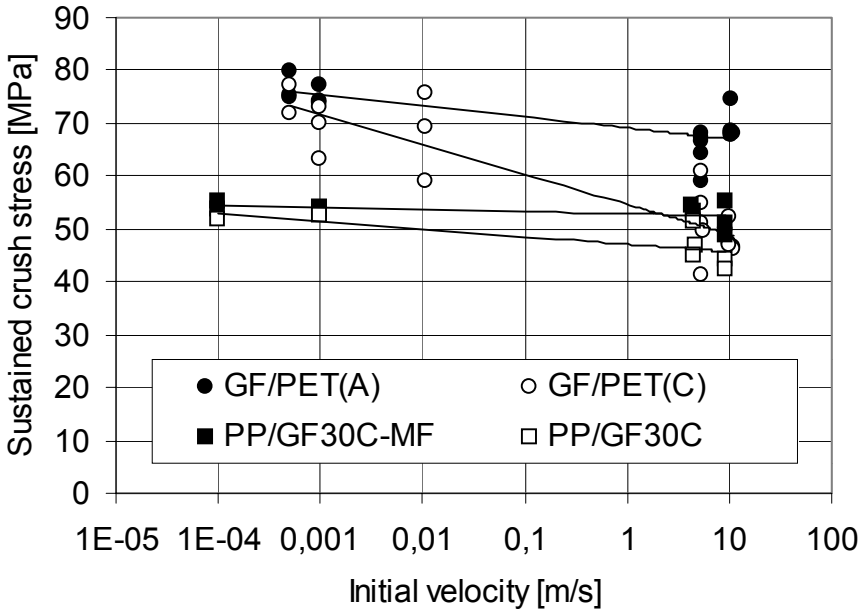

Figure 64: Sustained crush stress vs. initial impact velocity

The sustained crush stress is also approximately constant during crushing while the actual impactor velocity decreases to zero. The numerical investigations however, show a direct connection between the actual impactor velocity and the governing strain rate. Thus, with decreasing velocity, the sustained crush stress also decreases with a non-constant strain rate during crushing (Chapter 3.3.1).

These observations indicate the presence of opposite effects, namely thermal softening and strain rate effects as well as the non-constant contribution of matrix phase and mesoscopic composite phase. For unreinforced polymers the softening and rate effects are known and can be quantified within the formulation of the stress [105]:

$$\sigma = \sigma(\varepsilon, \dot{\varepsilon}, T) \tag{4.24}$$

The determination of the behaviour of the mesoscopic composite phase is not unequivocal. In addition, the strength relation of both mesoscopic phases R^m and R^l with the laminate behaviour R^L_{31} is needed to quantify the scaling effects due to strain rate, adiabatic heating and frictional heating. The macroscopic strain rate and temperature behaviour of the laminate can and should be measured to obtain the macroscopic material parameters. By combining the material behaviour of polymer phase and laminate, the mesoscopic properties can be determined in a mixed

numerical-experimental way. A numerical representative volume element with stacked polymer and composite laminae is loaded and compared with the experimental obtained laminate behaviour. Starting from a first estimate for the mesoscopic composite properties, the final properties are iteratively calculated (Figure 65).

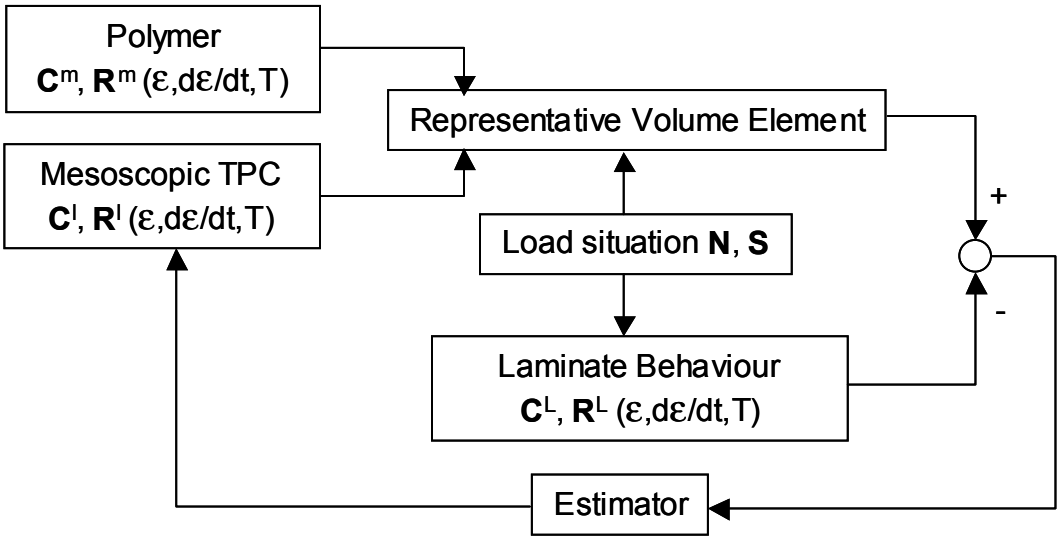

Figure 65: Determination of the mesoscopic composite lamina properties with the sets of stiffness and strength parameters $\mathbf{C}^l$ and $\mathbf{R}^l$

Since the strain rate and temperature behaviour of most unreinforced thermoplastics is known, a description for the mesoscopic composite transverse shear strength R_{31}^{*l} or for the laminate shear strength R_{31}^{*L} is needed. If one of both is known, the other can be estimated by the above mentioned estimation method. A formulation to take into account the different effects between R_{31} and R_{31}^{*} reads as

$$R_{31}^{*L} = R_{31}^{L}\left\{1+\dot{E}(\dot{\varepsilon},\dot{\varepsilon}_0)+\dot{T}(\Delta T^{p},\Delta T^{\mu})\right\} \tag{4.25}$$

Here, $\dot{E}$ is a function taking into account the rate dependency and $\dot{T}$ describes the temperature dependent material behaviour. The course of the strain rate part $\dot{E}$ is sufficiently described with a Johnson-Cook formulation as obtained in the impact shear perforation test (see also Chapter 2.4.2):

$$\dot{E} = c\ln\left(\frac{\dot{\varepsilon}}{\dot{\varepsilon}_0}\right) \tag{4.26}$$

In performing quasistatic direct shear tests at elevated temperatures, the thermomechanical behaviour of R_{31}^{L} can be obtained. This leaves the question of the height of the temperature increase $\dot{T}$ respectively the determination thereof as subparameter of the transverse shear strength. Referring to the assumptions for the predamaged zone, one could also assume that the temperature increase is the same for matrix and composite laminae. This would be sufficient if the crushing is governed by the same mechanisms. In addition to the heating as a result of plastic deformation, heating as a result of friction between crack surfaces occurs. The shear deformation of the matrix can be interpreted as adiabatic shearing, which has a localizing effect. Thus, also here separate treatment on a mesoscopic scale is necessary. The temperature rise due to plastic deformation ΔT^p can be estimated by [106], [108]:

$$\Delta T^p = \frac{W^p}{\rho c_p} = \frac{\sigma \varepsilon^p}{\rho c_p} \tag{4.27}$$

In equation (4.27) W^p stands for the amount of plastic work done per unit volume, ρ for the density and c_p for the material specific heat capacity. The magnitude of this heating is very different for the unreinforced and reinforced thermoplastic phase. Whereas failure of the reinforced phase is dominated by damage and fracture processes, the matrix interphases fail mainly by plastic deformation. Therefore, the temperature rise due to plastic work can be different in both phases.
Table 17 shows temperature rises of 4.1 ºC for elastic ideal-plastic PET per strain increment of 0.1, respectively 53.4 ºC up to the actual ultimate strain, whereas for the GF/PET (Table 18) the rise is estimated to be only 2.6 ºC. This last value is comparably small, because the plastic strain up to ultimate failure is only about 0.05 and can be neglected in the mesoscopic composite formulation.

Table 17: Thermal properties and temperature rise due to plastic work of PET and GF/PET

	σ_y	ε^p	ρ	c_p	dT/0.1	ε^u	$\Delta T^p(\varepsilon^u)$
	[MPa]	**[1]**	**[kg/dm^3]**	**[kJ/(kgK)]**	**[K/1]**	**[1]**	**[K]**
PET	55	0.1	1.34	1	4.1	1.3	53.4

Table 18: Thermal properties and temperature rise due to plastic work of GF/PET

	R_{31}	ε^p	ρ(GF)	c_p(GF)	ϕ_v	c_p(L)	$\Delta T^p(\varepsilon^u)$
	[MPa]	**[1]**	**[kg/dm³]**	**[kJ/(kgK)]**	**[1]**	**[kJ/(kgK)]**	**[K]**
GF/PET	90	0.05	2.54	0.84	0.5	0.9	2.6

The temperature rise due to friction ΔT^{μ} can be estimated by [106]:

$$\Delta T^{\mu} = \frac{2}{\sqrt{\pi}} \frac{\mu}{\sqrt{\lambda \rho c_p}} \sigma_N v \sqrt{t} \tag{4.28}$$

Here, λ is the thermal conductivity, ρ the density, c_p the specific heat, μ the coefficient of friction, σ_N the contact stress, v the relative contact velocity and t the contact time. Unfortunately, both the coefficient of friction μ and the specific heat c_p are functions of the temperature. Nevertheless, to obtain an order of magnitude relative to the reference state T_0 a first estimate is done without influences of velocity and temperature on μ and c_p. Within a FE-model both the contact time and the contact velocity are known. Here, the contact duration between two laminae is derived from the geometric shape of the crush zone of the FE-model from Chapter 3.3.1. With equation (4.28) and the contact stresses coming from the numerical simulation, the temperature rise ΔT^{μ} can be calculated for different values of $v\sqrt{t}$ (Figure 66).

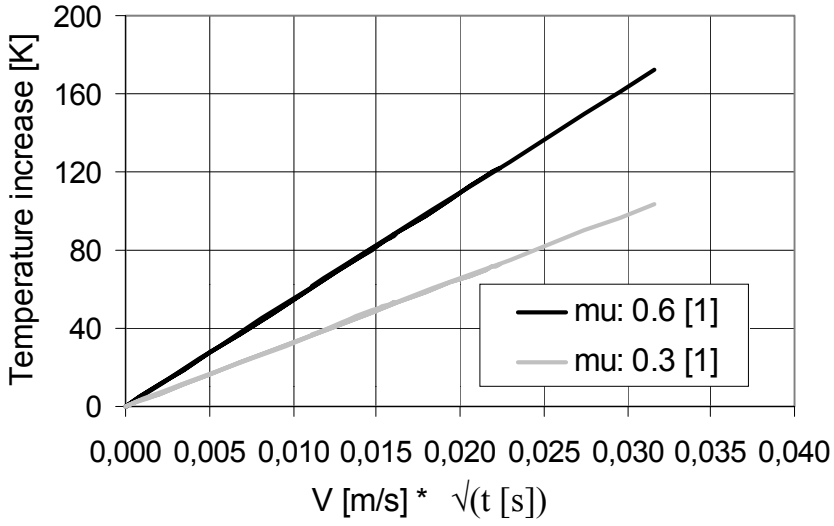

Figure 66: Temperature rise due to frictional effects

Concerning the numerical simulation it is known that the contact duration at the constant impact velocity v = 10 m/s is about 0.1 ms. As discussed in the results of the numerical simulation, the impactor is decelerated and the actual velocity decreases nonlinearly to zero, which leads to a longer contact time. For the product velocity and time however, the non-linear decrease means a smaller sensitivity for changes of the velocity during crushing.

4.3.4 Modelling numerical ultimate failure

Progressive crushing is a continuous process of crack growth and plastic deformation along the longitudinal axis of a crash element. The spatial discretization of the finite element method causes some discontinuities. This is especially seen for large deformations of the plane stress variant. For large element deformations the time step size becomes very small. To put a limit on the time step size, an additional phase – ultimate failure - is included in the model. A 2D FE-model of the crushing of a beam with only movement in the x,y-plane demonstrates the effects of abrupt element erosion within the ultimate phase. Boundary conditions and results are shown in Figure 67 and Figure 68. The used material model is the LS-DYNA 950 “laminated composite model”.

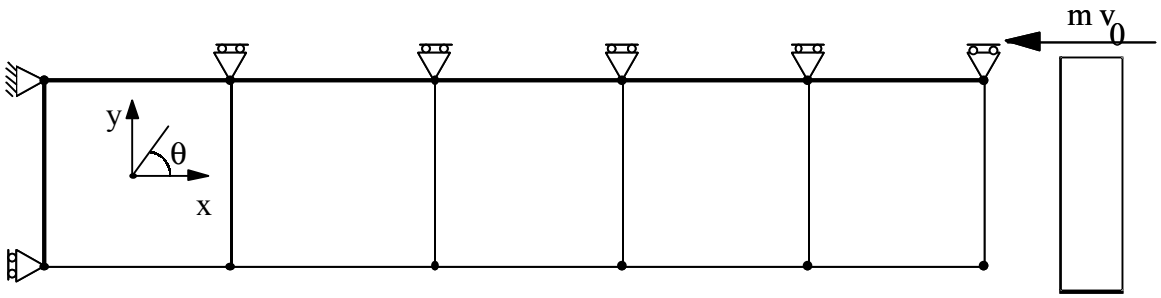

Figure 67: 2D FE-model of crushing a beam with 5 elements

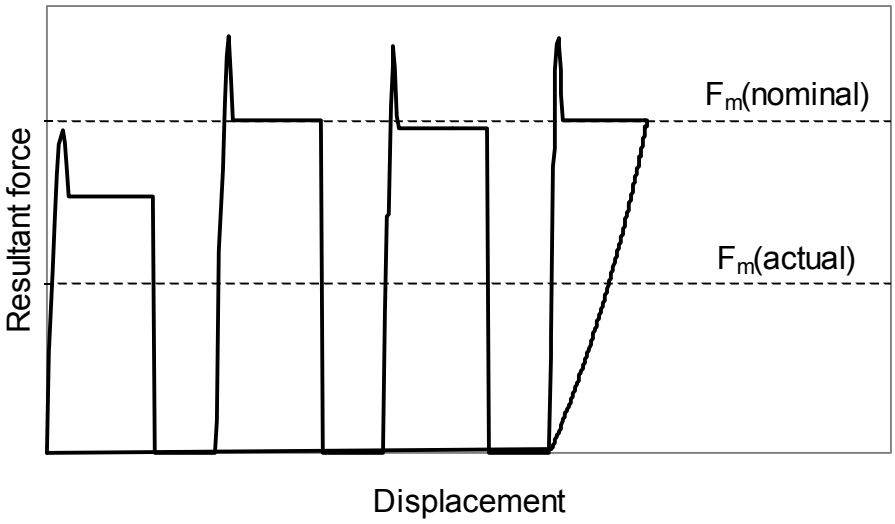

Figure 68: Force-displacement diagram with element erosion

The first element of the beam is modelled with a smaller wall thickness to represent a trigger. This induces a controlled failure of finite elements from the impactor side. Each finite element is eroded from the simulation at a predefined value of the failure strain. With a perfect parallel mesh geometry relative to the impactor mass this results in a typical block wise force-deflection diagram (Figure 68).

The actual numerical resultant mean force is too low, since it is obtained from the integrated results including the zero force level regions. Also for smaller mesh sizes, paved non-parallel meshes or complex structures this effect is apparent though not directly visible. The nominal crush force can principally not (!) be achieved with such material models containing element erosion, which disturbs the force transition between impactor and material. The mesh size does not influence the magnitude of the actual resultant force nor eliminates eventually apparent shock waves due to the repeated impacts on new rows of finite elements [32]. Element erosion should be prevented to sustain contact between impactor and material and thus have a reaction force.

A possibility to solve the above problem is the introduction of a compressive block phase or a material switch to rigid material behaviour. Combined with the scaling of the compressive strength to the height of the transverse shear strength during crushing $R_{31}{}^{L}$ the correct level of progressive crushing is obtained. Though this is an artificial method, the result of the simulation is correct even for coarse meshes with large finite elements.

For element formulations including the mesoscopic set-up with composite and matrix interphase laminae, such a phase is not necessary. Here, softening due to damage in the separate composite laminae and thermal softening in the matrix interphase laminae are mechanisms which extend the ultimate strain of the material beyond the maximum governing strain during crushing. As seen in evaluating the crushing mechanism, a material element passes through the crush zone and returns from the impactor after which it is unloaded with a certain amount of remaining plastic deformation. For a finite element this means that it is loaded in shear and bending and does not compress to such small sizes that need numerical intervention to limit the computation time.

5 Conclusions

Experimental investigations

- The energy absorption capability of the investigated knitted fabric GF/PET is positioned between random oriented composites like SMC and GMT and oriented composites like woven fabrics. However, the difference between mat reinforced TPC and KFRP is small. The energy absorption potential of KFRP can be further increased by using welding instead of riveting. The structure of the knitted fabrics is better suited for this joining method better than other reinforcements.
- The chosen geometry of the crash element shows a good potential to determine and compare the energy absorption behaviour of composites with thermoplastic matrix systems. At the same time this type of crash element allows phenomenological investigations for constitutive modelling for the prediction of the crashworthiness of composites, which fail in progressive crushing.
- The governing mechanisms during progressive crushing are lamina bending and transverse shear superposed with strain rate effects and thermal activity due to friction. The strain rate and temperature effects have an opposite influence of a magnitude, which depends on reinforcement and polymer type. The transverse shear mode demonstrated the domination effect of the inherent stacked or layered nature of the materials.
- Dynamic perforation tests on a Split-Hopkinson-Pressure-Bar showed the resemblance of the perforation strength with the transverse shear strength for crushing. This allows the rate and temperature dependency of the transverse shear strength to be characterized with simple coupon tests.

Numerical investigations

- The governing failure mode – lamina bending and transverse shear – only establishes due to the existence of matrix interplies. Simulations with equal properties for all layers fail to proceed in this mode.
- The potential of the mesoscopic model is limited to qualitative information on the laminae behaviour since the available material models cannot describe the anisotropic and thermal behaviour of TPCs properly. However, the obtained

strain rate and strain rate distribution give a good indication that the local strain rates are far higher than generally expected and explain the thermal increase.

- The absence of the possibility to model a predamaged zone leads to the necessity to model the complete elastic region as predamaged, which prevents the investigation of influence this zone.
- In general, the force response of the mesoscopic model is lower than the experimentally obtained values. This is caused by the idealization of the non-flat knitted fabric laminae into flat laminae as well as the neglecting of the strain rate and thermal effects on the behaviour of different mesoscopic phases. These effects all influence the leverage of the modelled laminae, which has a large influence on the absolute resultant crush force.

FE - Material model

- The complex anisotropic, rate and temperature dependent heterogeneous behaviour of thermoplastic composites cause such different material responses for different loadings, that the material behaviour can only be expressed in material models, which are formulated to describe only certain applications and load situations. For static applications where only small deformations occur, the Classical Laminate Theory would be sufficient. In general, totally different possible functional models are needed to describe e.g. fatigue behaviour or crashworthiness.
- The material model to simulate progressive crushing consists of numerical features and material properties due to the influence of the spatial discretization and homogenization in FE. It is a compromise between computation time and material model efficiency. To model structures in a realistic way solid elements would be necessary but these cost too much computational effort, while shell elements reduce the computation time and the model accuracy. However, this results in an increased experimental effort to determine mechanical behaviour and material parameters.
- The material model to describe progressive crushing is limited to materials that fail in lamina bending and transverse shear and have an inherent stacked configuration. These failure modes can only occur when certain additional boundary conditions like an appropriate geometry for progressive crushing are also present.

- The results of simulation depend largely on the description of the failure surface of the material in question. Even for KFRP the variation of possible failure surfaces is so large, that a description of sub-surfaces for each relevant quadrant is necessary to reduce the complexity of the model. Even with the model proposed in Chapter 4, a large amount of tests is necessary to determine polymer properties as well as composite properties since the heterogeneity of the material dominates the crushing behaviour.

6 Summary

This thesis examines the behaviour of inherent layered thermoplastic composites (TPCs) by performing experimental and numerical investigations. The objective of these investigations is to identify and quantify the failure and energy absorption mechanisms of layered quasi-isotropic thermoplastic composites, and translate this knowledge into properties and behaviour of a material model, which us capable of predicting the crashworthiness in transient analyses.

Representatives for this class of materials are un- or medium-stretched plain knitted fabrics and glass mat reinforced thermoplastics (GMT). The investigations on weft knitted glass fibre (GF) reinforced poly(ethylene-terephthalate) (PET) were performed as part of a research project to characterize its processing and behaviour [2]. Experiments on GMT and chopped GMT were also performed for comparison with the knitted reinforcement and to confirm the observed behaviour of the knitted fabric.

Special attention is paid to the influence of the specimen geometry on the results, since crash characteristics largely depend on the geometry of the tested specimen. A circular double hat profile is defined with which it is possible to obtain the geometrical influence. This particular geometry also has advantages concerning energy absorption capability as well as manufacturability for thermoplastic composites. Impact and perforation tests were performed to investigate the damage propagation and characterize the ductility of the investigated materials.

The investigated TPCs fail in a laminate bending mode with transverse shearing between laminae and partially traversing shear cracks in each lamina. By coupling the governing failure mode to crash characteristics like sustained crush stress, indications of relations between material parameters and quantitative energy absorption behaviour could be obtained.

Numerical investigations were performed with an explicit finite element code for the simulation of 3D large deformations. The model consists of a mesoscopic representation distinguishing between matrix interphase laminae or interplies and mesoscopic composite laminae. The model geometry illustrates the simplified cross-section of a longitudinal cut through the specimen. The influence of frictional effects between impactor and material as well as between laminae is quantified. Also the governing local strain rate, energy and stress-strain distribution over the different mesoscopic phases are obtained. Owing to this, the model could demonstrate and

partially explain the different effects caused by the heterogeneous character of the laminate. Even for a quasi-isotropic and homogeneous materials like chopped GMT the inherent matrix interplies due to the manufacturing process, dominate the onset of the governing crushing mode.

Based on the results of the performed experimental and numerical investigations, a phenomenological model with a-priori information on the inherent material behaviour is proposed. Due to the fact that the crash behaviour is dominated by the heterogeneous character of the material, the model also treats the different material phases separately.

A basic method for the determination of the mesoscopic material properties is briefly discussed. For the description of the behaviour of a thermoplastic matrix during crushing, a strain rate and temperature dependent plasticity law should be sufficient. To model the behaviour of the composite laminae, a coupled plastic damage law is proposed. Such a model is able to describe both plastic behaviour of the matrix as well as softening caused by matrix-fibre interface failure and fibre cracks. The model differentiates between two loading situations leading to either crushing or non-crushing failure. This division enables the explicit modelling of the material during crushing taking into account the specific material state as well as the geometry necessary to generate the load situation, which leads to progressive crushing.

7 References

7.1 Literature

[1] Spencer, D.J.: Knitting Technology, 2nd Ed. Pergamon Press Oxford, 1989

[2] Brite Euram 7290, Protailtherm (Property Tailoring and Net Shape Proceeding of Structures from Textile Preforms with Thermoplastic Matrices), March 1999

[3] Mayer, J.: Gestricke aus Kohlenstoffasern für biokompatible Verbundwerkstoffe, dargestellt an einer homoelastischen Osteosyntheseplatte. Dissertation ETH Nr. 10487, ETH Zürich, 1994

[4] Tan, P., Tong, L., Steven,G.P.: Modelling for prediction the mechanical properties of textile composites – A review. *Composites Part A*, 28A, (1997) pp. 903-922

[5] Ramakrishna, S., Hamada, H., Kotaki, M., Wu, W.L., Inoda, M., Maekawa, Z.: Future of knitted fabric reinforced polymer composites. *Proceedings of the 3rd Japan International SAMPE Symposium*, Dec. 7-10 (1993) pp. 312-317

[6] Gommers, B., Verpoest, I., van Houtte, P.: Modelling the elastic properties of knitted-fabric-reinforced composites. *Composites Science and Technology*, Vol. 56 (1996) pp. 685-694

[7] Gommers, B., Verpoest, I., van Houtte, P.: Analysis of knitted fabric reinforced composites: Part I. Fibre orientation distribution. *Composites Part A*, 29A (1998) pp. 1579-1588

[8] Gommers, B., Verpoest, I., van Houtte, P.: Analysis of knitted fabric reinforced composites: Part II. Stiffness and strength. *Composites Part A*, 29A (1998) pp. 1589-1601

[9] Ramakrishna, S.: Analysis and Modelling of Plane Knitted Fabric Reinforced Composites, *Journal of Composite Materials*, Vol. 31 (1997) No. 1, pp. 52-70

[10] Ramakrishna, S.: Characterization and Modelling of the Tensile Properties of Plane Weft-Knit Fabric-Reinforced Composites, *Composites Science and Technology*, Vol. 57 (1997) pp. 1-22

[11] Ramakrishna, S., Maekawa, Z., Cuong, N.K.: Analytical methods for prediction of tensile properties of plane knitted fabric reinforced composites. *Advanced Composite Materials*, Vol. 6 (1997) No. 2, pp. 123-151

[12] Ruan, X., Chou, T-W.: Failure Behavior of Knitted Fabric Composites. *Journal of Composite Materials*, Vol. 32 (1998) No. 3, pp. 198-222

[13] Ramakrishna, S., Hull, D.: Tensile behaviour of knitted carbon-fibre-fabric/epoxy laminates-Part II: Prediction of tensile properties. *Composites Science and Technology*, Vol. 50 (1994) pp. 249-258

[14] Huysmans, G., Gommers, B., Verpoest, I.: Mechanical properties of (2D) warp knitted fabric composites: An experimental and numerical investigation. SAMPE 99, Basel (1996) pp. 97-108

[15] Ruan, X., Chou, T-W.: Experimental and theoretical studies of the elastic behaviour of knitted-fabric reinforced composites. *Composites Science and Technology*, Vol. 56 (1996) pp. 1391-1403

[16] Putnoki, I., Moos, E., Karger-Kocsis: Mechanical performance of stretched knitted fabric glass fibre reinforced poly(ethylene terephthalate) composites produced from commingled yarn. *Plastics, Rubber and Composites Processing and Applications*, Vol. 28 (1999) No. 1, pp. 40-46.

[17] Karger-Kocsis, J., Czigany, T., Mayer, J.: Fracture behaviour and damage growth in knitted carbon fibre fabric reinforced polyethylmethacrylate. *Plastics, Rubber and Composites Processing and Applications*, Vol. 25 (1996) No. 3, pp. 109-114.

[18] Czigany, T., Ostgathe, M., Karger-Kocsis, J.: Damage Development in GF/PET Composite Sheets with Different Fabric Architecture Produced of a Commingled Yarn. *Journal of Reinforced Plastics and Composites*, Vol.17 (1998) No. 3, pp. 251-267

[19] Karger-Kocsis J., Czigány, Gaál J., Osrgathe M.: Stiffness and strength anisotropy in the tensile response of weft knitted fabric-reinforced PEEK- and PET-composites. *Adv. Compos. Letters*, 5 (1996) pp. 71-75.

[20] Karger-Kocsis, J., Czigany, T.: Effects of interphase on the fracture and failure behaviour of knitted fabric reinforced composites produced from commingled GF/PP yarn. *Composites Part A*, 29A (1998) pp. 1319-1330

[21] Rudd, C.D., Owen, M.J., Middleton, V.: Mechanical properties of weft knit glass fibre/polyester laminates. *Composites Science and Technology,* 39 (1990) pp. 261-277

[22] Chou, S., Wu, C.J.: A study of the physical properties of epoxy resin composites reinforvced with knitted glass fiber fabrics. *Journal of Reinforced Plastics and Composites*, Vol.11 (1992) November, pp. 1239-1250

[23] Chou, S., Chen, H.-C., Lai, C.-C.: The fatigue properties of weft-knit fabric reinforced epoxy resin composites. *Composites Science and Technology*, 45 (1992) November, pp. 283-291

[24] Mayer J., Ruffieux K., Tognini R., Ha S-W, Wintermantel E.: Knitted carbon fiber reinforced thermoplastics; influence of structural parameters on manufacturing techniques and mechanical properties. *Proc. Int. Symp. on Adv. Mat. For Lightweight Struct.*, Noordwijk, Netherlands, 1994.

[25] Ramakrishna, S., Hull, D.: Tensile behaviour of knitted carbon-fibre-fabric/epoxy laminates-Part I: Experimental. *Composites Science and Technology*, Vol. 50 (1994) pp. 237-247

[26] Gommers, B., Verpoest, I..: Tensile behaviour of knitted fabric reinforced composites. *Proceedings of ICCM-10*, Whistler, B.C., Canada, August 1995, IV –309-316

[27] Gommers, B., Wang, T.K., Verpoest, I..: Mechanical properties of warp knitted fabric reinforced composites. *40th International SAMPE Symposium*, May 8-11 (1995) pp. 966-976

[28] Wu, W.-L., Kotaki, M., Fujita, A.: Mechanical properties of warp-knitted, fabric-reinforced composites. *Journal of reinforced plastics and composites*, Vol. 12 (1993) pp. 1096-1110

[29] Ramakrishna, S., Hull, D.: Energy absorption capability of epoxy composite tubes with knitted carbon fibre fabric reinforcement. *Composites Science and Technology*, Vol. 49 (1993) pp. 349-356

[30] Ramakrishna, S.: Energy absorption characteristics of knitted fabric reinforced epoxy composite tubes. *Journal of Reinforced Plastics and Composites*, Vol. 14 (1995) pp. 1121-1141

[31] Huisman, M.R.S., Maier, M.: Investigation on the Crash Behaviour of Knitted Glass Fibre Reinforced Poly(ethylene-terephthalate) Structures. *International Journal of Crashworthiness*, Vol.5 (2000) No.1, pp. 79-88

[32] Huisman, M.R.S., Maier, M.: Modellierung des Crash-Verhaltens von gestrickeverstärkten Thermoplasten. 16. CADFEM USERS' MEETING, Bad Neuenahr-Ahrweiler, 7.-9. Oktober 1998, 2-28 ff.

[33] Huisman, M.R.S., Maier, M.: Materialmodellierung von gestrickeverstärkten Thermoplasten unter Stoßbelastung. IVW-Kolloquium ´98, Kaiserslautern, 20.-21. Oktober 1998

[34] Hull, D.: A Unified Approach to Progressive Crushing of Fibre-Reinforced Composite Tubes, *Composites Science and Technology* 40 (1991) pp. 377-421

[35] Farley, G.L., Jones, R.M.: Prediction of the energy-absorption capability of composite tubes, *Journal of Composite Materials*, Vol. 26 (1992) No. 3, pp. 388-404

[36] Farley,G.L., Jones, R.M.: Crushing characteristics of continuous fiber-reinforced composite tubes, *Journal of Composite Materials*, Vol. 26 (1992) No. 1, pp. 37-50

[37] Kindervater, C.M., Georgi, H.: Composite strength and energy absorption as an aspect of structural crash resistance. In: structural crashworthiness and failure, Ed.: Jones, N., Wierzbicki, T., elsevier applied science, London and New York, 1993

[38] Kerth, S., Himmel N., Maier, M.: Rechnergestützte Bauteilprüfung. *Kunststoffe* 84 (1994) 12, pp. 1702-1704

[39] Thornton, P.H., Harwood, J.J, Beardmore, P.: Fibre-reinforced Plastic Composites for Energy Absorption Purposes. *Composites Science and Technology,* 24 (1985) pp. 275-298

[40] Farley, G.L., Energy Absorption of Composite Materials. *Journal of Composite Materials*, Vol. 17 (1983) May, pp. 267-279

[41] Mamalis, A.G., Robinson, M., Manolakos, D.E., Demosthenous, G.A., Ioannidis, M.B., Carruthers, J.: Crashworthy capability of composite material structures. *Composite Structures* 37 (1997) pp. 109-134

[42] Mamalis, A.G., Manolakos, D.E., Demosthenous, G.A., Ioannidis, M.B.: Crashworthiness of Composite Thin-Walled Structural Components. Technomic Publication Lancaster 1998

[43] Fairfull, A.H., Hull, D.: Energy Absorption of polymer matrix Composite Structures: Frictional Effects. In: Structural failure; 2nd International Symposium on Structural Crashworthiness, Cambridge, MA, June 6-8, 1988, pp. 255-279

[44] Zienkiewicz, O.C., Taylor, R.L.: The Finite Element Method, Volume 1. Basic Formulation and Linear Problems, 4th Edition, London: McGraw-Hill Book Company 1991

[45] Zienkiewicz, O.C., Taylor, R.L.: The Finite Element Method, Volume 2. Solid and Fluid Mechanics Dynamics and Non-linearity, 4th Edition, London: McGraw-Hill Book Company 1991

[46] Bathe, K.-J.: Finite-Elemente-Methoden. Berlin. Springer Verlag 1990

[47] Hallquist, J.O.: LS-Dyna Theoretical Manual. May 1998

[48] Matzenmiller A., Lubliner J., Taylor R.L.: A constitutive model for anisotropic damage in fiber-composites. *Mechanics of Materials* 20 (1995) pp. 125-152

[49] Kachanov L.M.: Introduction to continuum damage mechanics. Dordrecht. Martinus Nijhof (1985)

[50] Maier, M.: Experimentelle Untersuchung und numerische Simulation des Crashverhaltens von Faserverbundwerkstoffen. D386, Dissertation Universität Kaiserslautern 1990

[51] Maier, M.: Entwicklung integrierter Automobilteile aus Faserverbundwerkstoffen. BMFT-Bericht 03M1021-A9 (1991)

[52] Maier, M., Matzenmiller, A., Rust, W., Schweizerhof, K.: Energy Absorption with Composite Crash Elements in Frontal Crash – An Analysis with LS-DYNA3D. 26. ISATA, Aachen, Germany, 13-17 September 1993

[53] Hamada, H., Ramakrishna, S.: A FEM Method for Prediction of Energy Absorption Capability of Crashworthy Polymer Composite Materials. *Journal of Reinforced Plastics and Composites* Vol. 16 (1997) No. 3, pp. 226-242

[54] Schweizerhof, K., Weimar, K., Münz, Th., Rottner, Th.: Crashworthiness Analysis with Enhanced Composite material Models in LS-DYNA – Merits and Limits. 16. CADFEM USERS' MEETING, Bad Neuenahr-Ahrweiler, 7.-9. Oktober 1998, 2-29 ff.

[55] Schweizerhof, K., Münz, Th., Weimar, K., Rottner, Th.: Improving and testing the composite materials in LS-DYNA for crash problems – a critical survey. Rep. No. CRASHURV 2-1, 2/98, EC Project, CADFEM GmbH Grafing (1998)

[56] Thoma, K., Vinckier, D.: Numerical Simulation of a High Velocity Impact on Fiber Reinforced Materials. IMPACT IV, SMiRT Post-Conference Seminar, Bundesanstalt fuer Materialforschung und –Pruefung, Berlin, Germany, August 23-24, 1993

[57] Vinckier, D.: A Numerical Model for the Impact and Penetration of Thermoplastic Woven Fabric Composites. Third International Conference on Composite Engineering; New Orleans, July 21-26, 1996

[58] Haug, E., Fort, O., Tramecon, A.: Numerical Crashworthiness Simulation of Automotive Structures and Components Made of Continuous Fiber Reinforced Composite and Sandwich Assemblies. SAE Int. Congress and Exposition, Detroit, Michigan, February 25 – March 1, 1991 (910152)

[59] Johnson, A.F., Kohlgrueber, D.: Modelling the Crash Response of Composite Structures. J. Phy. IV France 7, Colloque C3 (1997) pp. 981-986

[60] Deletombe, E., Delsart, D., Fabis, J., Johnson, A.F.: Enhanced composite material law for energy absorption modelling of anti-crash components in aeronautics. IJCRASH ’98, 9-11 September, Dearborn, USA (1998) pp. 432-443

[61] Sigalas, I., Kumosa, M., Hull, D.: Trigger mechanisms in Energy-Absorbing Glass Cloth/Epoxy Tubes, *Composite Science and Technology*, Vol. 40 (1991), pp. 265-287

[62] Haug, E., Jamjian, M.: Numerical simulation of the impact resistance of composite structures. In: Analysis and Modelling of Composite Materials. Ed. Bull, J. Chapter 8 (1996) pp. 185-246

[63] Oberbach, K.: Saechtling. Kunststoff Taschenbuch. 26. Ausgabe, Carl Hanser Verlag München, 1995

[64] Mathot, V.B.F.: Calorimetry and Thermal Analysis of Polymers. Hanser Publishers, Munich 1994

[65] Dittmar, H., Groen, J., Mooijman, F., Peterson, C.: Schnittfaserlaminate – eine Weiterentwicklung des Werkstoffes GMT, Chopped Fibre Laminates – Latest GMT Developments. AVK-Tagung Baden-Baden, Oktober 1999, B4, pp. 1-15

[66] Mouzakis, D.E.: Application of the essential work of fracture method for ductile polymer systems. Dissertation D386, University of Kaiserslautern, Mensch und Buch Verlag Berlin 1999

[67] Billington, E.W., Brissenden, C.: Dynamic Stress-Strain Curves for Various Plastics and Fibre-Reinforced Plastics. *J. Phys. D: Appl.Phys.*, Vol. 4 (1971) pp. 272-286

[68] Klepaczko, J.R.: An experimental technique for shear testing at high and very high strain rates, the case of mild steel. *Int. J. Impact Engng.*, Vol. 15 (1998) pp. 25ff

[69] Klepaczko, J.R.: Remarks on Impact Shearing. *J. Mech. Phys. Solids*, Vol. 46 (1998) No. 10, pp. 2139-2153

[70] Stellbrink, K.K.U.: Micromechanics of composites. Hanser Publishers Munich 1996

[71] N.N.: Eastman EASTAPAK PET datasheet 1999

[72] Kaw, A.K.: Mechanics of Composite Materials. CRC Press Boca Raton 1997

[73] Tsai, S.W.: A Survey of Macroscopic Failure Criteria for Composite Materials. Journal of Reinforced Plastics and Components. Vol. 3 (1984) January, pp. 40-62

[74] Hart-Smith, L.J.: The role of biaxial stresses in discriminating between meaningful and illusory composite failure theories. Composite Structures, Vol.25 (1993) pp. 3-20

[75] Chandler, H.D., Campbell, I.M.D., Stone, M.A.: An assessment of failure criteria for fibre-reinforced composite laminates. *Int. J. Fatigue*, Vol. 17 (1995) No. 7, pp. 513-518

[76] Becker, W.: Experimentelle und mathematische Untersuchung von Stoßbelastungen auf beliebige Faserverbundbauteile. Dissertation Universität Kaiserslautern, Shaker Verlag Aachen 1995

[77] Thom, H.: A review of the biaxial strength of fibre-reinforced plastics. *Composites Part A* (1998) **29A**, pp. 869-886

[78] Harris, B.: Failure Criteria in Fibre-Reinforced-Polymer Composites. Special Issue *Composites Science and Technology,* Vol.58 (1998) pp. x-y

[79] Hill, R.: A theory of the yielding and plastic flow of anistropic metals. Proceeding of the Royal Society, london, Series A, PRSLA, Vol. 193 (1948) pp.281-297

[80] Hoffman, O.: The Brittle Strength of Orthotropic Materials. *Journal of Composite Materials*, Vol. 1 (1967) pp.200-206

[81] Tsai, S.W., Wu, E.M.: A General Theory of Strength for Anisotropic Materials. *Journal of Composites Materials*, Vol. 5 (1971) January, pp. 58-80

[82] Hashin, Z.: Failure criteria for unidirectional fiber composites. *Journal of Applied Mechanics*, Vol. 47 (1980) June, pp. 329-334

[83] Chang, F.K., Chang, K.Y.: A progressive damage model for laminated composites containing stress concentrations. *Journal of Composites Materials*, Vol. 21 (1987) September, pp. 834-855

[84] Hart-Smith, L.J.: The Truncated Maximum Strain Composite Failure Model. *Composites*, Vol. 24 (1993) No. 7, pp. 587-591

[85] Hart-Smith, L.J.: Predictions of the Original and Truncated Maximum-Strain Failure Models for Certain Fibrous Composites Laminates. *Compos. Sci. Technol.*, Vol. 58 (1998) No. 7, pp. 1151-1178

[86] Wolfe, W.E., Butalia, T.S.: A Strain-Energy Based Failure Criterion For Non-Linear Analysis of Composite Laminates Subjected to Biaxial Loading. *Compos. Sci. Technol.*, Vol. 58 (1998) No. 7, pp. 1107-1124

[87] Kroll, L., Hufenbach, W.: A Physically Based Failure Criterion for Laminated Composites. *Mechanics of Composite Materials*, Vol. 35 (1999) No. 4, pp. 413-422

[88] Puck, A.: Festigkeitsanalyse von Faser-Matrix-Laminaten: Modelle fuer die Praxis. Carl Hanser Verlag Muenchen Wien 1996

[89] Puck, A., Schuermann, H.: Failure Analysis of FRP Laminates by Means of Physically Based Phenomenological Models. *Compos. Sci. Technol*. Vol. 58 (1998) No. 7, pp. 1045-1067

[90] Cuntze, R.G.: Progressive Failure of 3D-stressed Laminates: Multiple Nonlinearity Treated by the Failure Mode Concept (FMC). DURACOSYS‘99, June 15 (1999) pp.1-5

[91] Ward, I.M.: Mechanical Properties of Solid Polymers, John Wiley & Sons Chichester, Second Edition 1983

[92] Jones R.M.: Mechanics of Composite Materials. Hemisphere Publishing Corporation New York 1975

[93] Lemaitre, J.: A course on damage mechanics, Springer Verlag Berlin, 1992

[94] Berstad, T., Hopperstad, O.S., Lademo, O.-G., Malo, K.A.: Computational Model of Ductile Damage and Fracture in Shell Analysis. In: 2nd European LS-DYNA Users Conference, Gothenborg, Sweden, June 14&15 (1999), pp. A-37 – A-A44

[95] Lindholm, U.S. in R.F. Bunshah (Ed.), *Techniques in Metals Research*, Vol.5, part 1, Interscience, New York 1971

[96] Ostgathe, M.: Zur Serienfertigung gewebeverstärkter Halbzeuge für die Umformung. Dissertation Universiät Kaiserslautern, Fortschr.-Ber. VDI Reihe 2 Nr. 440, VDI Verlag Düsseldorf 1997

[97] Mayer, C.: Prozeßanalyse und Modellbildung zur Herstellung gewebeverstärkter, thermoplastischer Halbzeuge. Dissertation Universität Kaiserslautern 2000

[98] Van Krevelen, D.W.: Properties of polymers. Their correlation with chemical structure; their numerical estimation and prediction from addititve group contributions. Elsevier Science Publishers Amsterdam 1990

[99] Mark, J.E.: Physical Properties of Polymers Handbook. AIP Press Woodbury, New York 1996

[100] Vigny, M., Aubert, A., Hiver, J.M., Aboulfaraj, M., G'Sell, C.: Constitutive Viscoplastic Behaviour of Amorphous PET During Plane-Strain Tensile Stretching. *Polymer Engineering and Science*, Vol. 39 (1999) pp. 2366-2376

[101] Luethi, B., Reber,R., Janczak-Rusch, J., Rohr, L., Mayer, J.: Wintermantel, E.: Characterization of the GF/PET interface in knitted composites by means of the push-out technique. In: *Recent Advancement of Interfacial Material Science on Composite Materials '97, Tokio 1997*

[102] Luethi B., Reber R., Mayer J., Wintermantel E., Janczak-Rusch J., Rohr L.: An energy based analytical push-out model applied to characterize the interfacial properties of knitted glass fiber reinforced PET. *Composites Part A*, 29A (1998) pp. 1552-1562

[103] Dehn, A., Huisman, M.R.S., Maier, M.: Effects of temperature upon the crash behaviour of thermoplastic composites. *International Crashworthiness Conference,* IJCrash '98, Dearborn, Michigan, USA, 9-11 September (1998) pp. 480-487

[104] Kennedy, T.C., Nahan, M.F.: A simple nonlocal damage model for predicting failure of notched laminates. *Composite Structures,* 35 (1996) pp. 229-236

[105] Brostow, Corneliussen: Failure of Plastics, Hanser Publishers 1986

[106] Lemaitre, J., Chaboche, J.-L.: Mechanics of solid materials, Cambridge University Press, 1990

[107] Puppo, A.H., Evensen, H.A.: Interlaminar Shear in Laminated Composites under Generalized Plane Stress. Journal of Composite Materials. (1970) April, pp. 204-220

[108] Walley, S.M., Field, J.E.: Strain rate sensitivity of polymers in compression from low to high rates. DYMAT Journal, Vol.1 (1994) No. 3, September, pp. 211-227

[109] Zukas, J.A.: Impact dynamics, Wiley & Sons New York, 1990

7.2 Guided practical and diploma theses

[110] Wernicke, Ph.: Experimentelle Untersuchungen zur Energieabsorption von Rohren aus kohlenstoffaserverstaerktem Epoxidharz. IVW-Bericht 97-028, 1997

[111] Schulz, S.: Experimentelle Untersuchungen zum Crashverhalten von Rohren aus glasfaserverstaerktem Epoxidharz. IVW-Bericht 97-029, 1997

8 Appendix

8.1 Material abbreviations

Table 19: Investigated thermoplastic FRPs, SMC and aluminium crash elements

Material	Matrix	Fibre type	Fibre orientation
GF/PET(C)-KF	PET(K=52.4 %)	E-glass	Plain weft knit
SMC	Thermoset, UP	E-glass	Random chopped fibres
GMT C30	PP	E-glass	Random chopped mat
AlMg3 F23	Aluminium	-	-
GMT C30MF	PP + Mineral	E-glass	Random chopped mat
GF/PET(A)-KF	PET(K=27.5 %)	E-glass	Plain weft knit
AF/PA6-WF	PA6	Aramide	Plain weave
GF/PA12-WF	PA12	E-glass	Crowfoot 1/3
GF/PC-WF	PC	E-glass	Crowfoot 1/3
CF/PA12-WF	PA12	Carbon	Twill weave

8.2 Axial crash tests

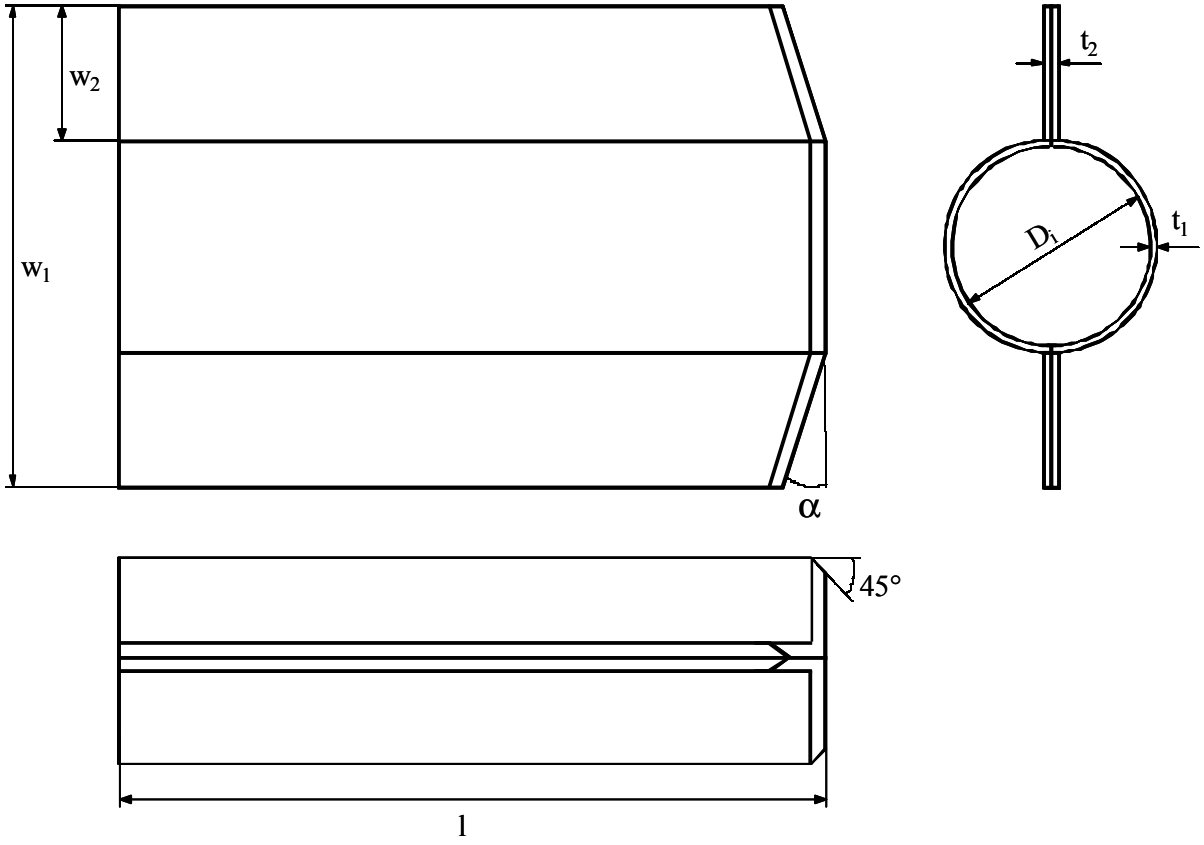

Figure 69: Geometry of a circular double hat profile

Table 20: Notation of geometrical properties

Crash element width	w_1
Flange width	w_2
Crash element length	l
Thickness of tubular part	t_1
Thickness of flanges	t_2
Crash element internal diameter	D_i
Flange inclination	α

Table 21: Notation and test series for GF/PET

Series (n = 5)	Trigger α [°]	Flange width w_2 [mm]	Joining method	Test velocity v [m/s]	PET state	Test temperature T [° C]
A	0	30	Rivet	5.5	A	RT
B	10	30	Rivet	5.5	A	RT
C	20	30	Rivet	5.5	A	RT
D	0	30	Rivet	0.0005	A	RT
E	10	30	Rivet	0.0005	A	RT
F	20	30	Rivet	0.0005	A	RT
G	10	30	Adhesive	5.5	A	RT
H	10	15	Weld	5.5	A	RT
I	10	30	Adhesive	0.0005	A	RT
J	10	15	Weld	0.0005	A	RT
K	10	20	Rivet	11	A	RT
L	10	20	Rivet	0.0005	C	RT
M	10	20	Rivet	5.5	C	RT
N	10	20	Rivet	11	C	RT
O	10	20	Rivet	11	A	RT
P	10	20	Rivet	5.5	A	RT
Q	10	20	Rivet	11	A	-30°
R	10	20	Rivet	11	A	0°
S	10	20	Rivet	11	A	50°
T	10	20	Rivet	11	A	90°
U	10	20	Rivet	5.5	A	RT
V	10	15	Rivet	5.5	A	RT

Table 22: Geometric characteristics of GF/PET crash elements

Series (n = 5)	Mass m [g]	Length l [mm]	Width w_1 [mm]	w_2 [mm]	Thickness t_1 [mm]	t_2 [mm]	Diameter D_i [mm]	Area A [mm^2]
A	210,67	150,48	117,64	30,88	2,60	4,52	50,06	709,10
B	209,96	150,72	117,77	30,96	2,42	4,47	50,18	676,49
C	207,04	150,54	117,74	31,51	2,50	4,51	50,04	696,65
D	209,07	150,40	117,80	31,55	2,47	4,45	50,12	688,70
E	210,11	150,68	116,00	29,94	2,25	4,50	50,26	640,43
F	206,24	150,32	117,68	31,63	2,49	4,42	50,13	691,01
G	186,08	144,44	117,50	30,14	2,27	5,95	51,85	744,51
H	134,07	137,36	88,26	15,84	2,34	3,92	50,04	509,04
I	184,51	145,08	117,36	30,08	2,34	5,47	51,51	724,79
J	137,93	140,75	87,95	15,95	2,34	3,86	50,08	507,92
K	180,81	149,96	98,48	20,44	2,22	4,51	50,24	550,03
L	180,02	149,83	98,35	20,25	2,18	4,44	50,25	537,80
M	179,53	150,02	98,08	20,36	2,21	4,45	50,32	545,71
N	178,92	149,10	98,58	20,36	2,20	4,45	50,42	544,69
O	180,78	149,82	98,28	20,12	2,25	4,61	50,34	557,05
Q	178,21	149,86	98,30	20,12	2,20	4,52	50,36	544,97
R	179,84	150,10	98,44	20,36	2,21	4,55	50,36	550,08
S	179,56	149,90	98,50	20,32	2,22	4,58	50,20	551,53
T	180,02	149,74	98,26	20,18	2,23	4,52	50,32	550,38
U	184,01	150,16	97,54	21,37	2,48	4,48	50,14	601,27
V	169,56	150,05	87,76	16,55	2,49	4,54	50,03	560,90
WA	235,63	150,23	117,00	29,87	2,58	5,25	50,00	740,14
WB	240,08	150,27	117,27	29,93	2,65	5,32	50,00	756,39

Table 23: Test conditions and measured properties of GF/PET crash elements

Series (n = 5)	Impactor Mass M [kg]	Impact Velocity v_0 [m/s]	Kin. Energy E_{kin} [kJ]	Max. Displ. l_{max} [mm]	Max Force (SAE 1000) F_{max} [kN]	Mean Force (SAE 1000) F_m [kN]	Abs. Energy E_{abs} [kJ]
A	180,12	5,40	2,62	61,10	71,49	42,78	2,62
B	180,12	5,41	2,63	61,92	59,17	42,08	2,61
C	180,12	5,35	2,58	59,70	60,42	42,87	2,56
D	0,00	0,00	0,00	74,90	66,06	43,75	3,28
E	0,00	0,00	0,00	74,92	67,53	45,20	3,39
F	0,00	0,00	0,00	74,90	61,80	42,80	3,21
G	180,12	5,36	2,59	56,83	60,50	45,13	2,57
H	180,12	5,40	2,63	67,31	46,39	38,34	2,59
I	0,00	0,00	0,00	74,89	63,51	42,10	3,15
J	0,00	0,00	0,00	74,91	59,79	49,17	3,68
K	45,37	10,76	2,62	66,74	51,75	38,13	2,55
L	0,00	0,00	0,00	64,89	55,78	36,27	2,35
M	180,12	5,42	2,65	92,58	44,16	28,12	2,57
N	45,37	10,33	2,42	88,99	41,96	26,01	2,31
O	45,41	11,37	2,98	74,35	54,48	37,70	2,81
Q	45,41	10,88	2,69	76,97	51,50	33,64	2,59
R	45,41	10,88	2,69	72,91	50,25	35,35	2,58
S	45,41	10,92	2,71	71,90	51,35	36,57	2,62
T	45,41	10,85	2,67	83,27	42,19	31,23	2,61
U	180,12	5,43	2,66	67,38	53,79	39,07	2,64
V	180,12	5,39	2,61	66,02	50,59	39,12	2,59
WA	180,12	7,48	5,05	78,40	83,33	63,06	4,95
WB	180,12	5,42	2,65	42,59	87,16	61,05	2,61

Table 24: Crash characteristics of GF/PET crash elements

Series (n = 5)	Spec. Abs. Energy E_s [J/g]	Sust. Crush Stress σ_s [MPa]	Load Uniformity L.U. [-]	Stroke Efficiency S_e [%]
A	30,65	60,40	1,67	60,06
B	30,30	62,29	1,41	71,38
C	31,26	61,55	1,41	71,15
D	31,46	63,50	1,51	66,23
E	32,39	70,57	1,49	67,01
F	31,20	61,95	1,44	69,38
G	35,16	60,67	1,34	74,93
H	39,37	75,36	1,21	82,98
I	33,13	58,18	1,51	66,34
J	50,18	96,81	1,22	82,24
K	31,70	69,34	1,36	73,93
L	30,18	67,41	1,54	65,26
M	23,53	51,55	1,57	63,66
N	21,73	47,74	1,61	62,21
O	31,32	67,71	1,45	69,38
Q	28,34	61,71	1,53	65,53
R	29,56	64,26	1,42	70,62
S	30,58	66,35	1,40	71,29
T	26,05	56,76	1,35	74,40
U	31,95	65,05	1,38	72,86
V	34,71	69,75	1,29	77,60
WA	40,30	85,22	1,32	76,18
WB	38,45	80,71	1,43	70,59

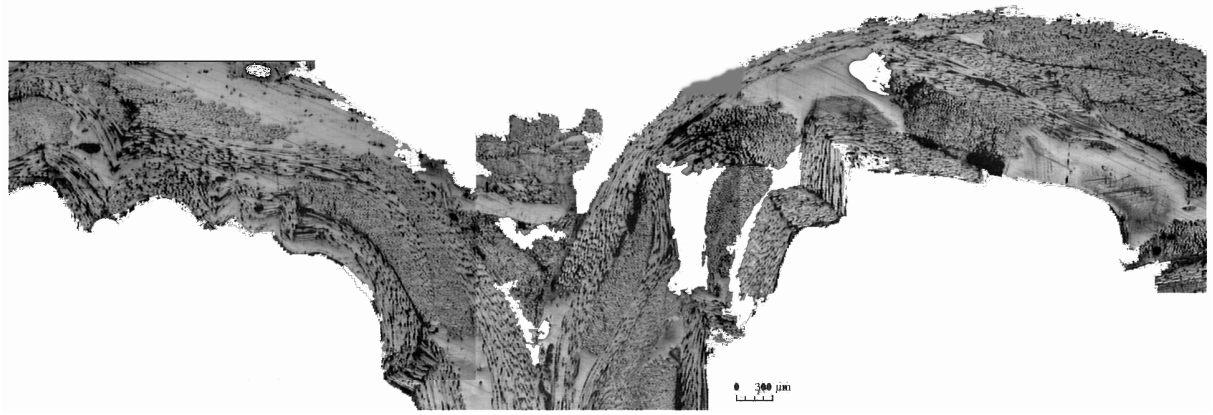

Figure 70: Micro-photograph of the crushed zone of GF/PET(A)

Figure 71: Micro-photograph of the crush zone of GF/PET(C)

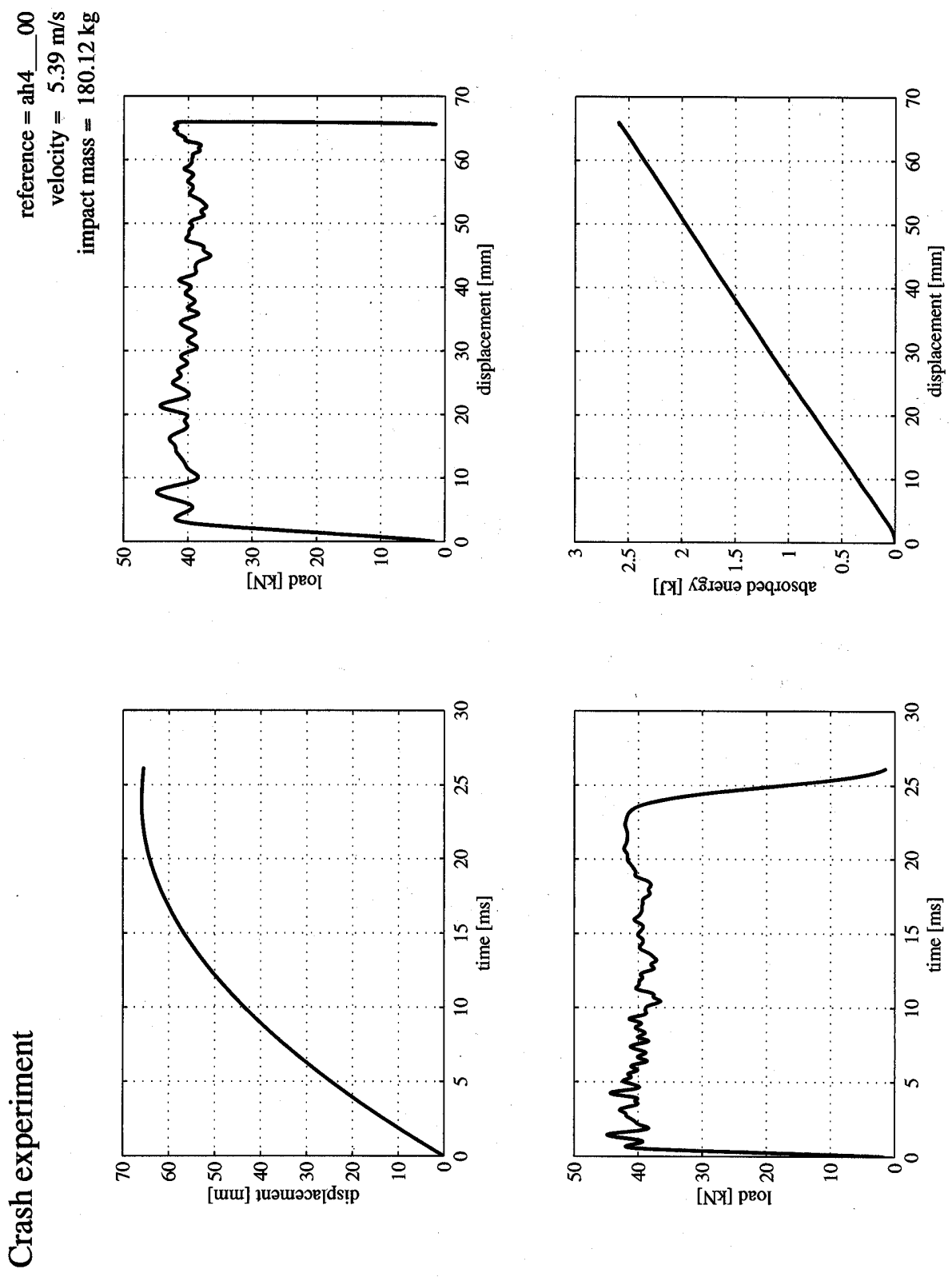

Figure 72: Example of a diagram of a crash test on GF/PET(A) (Series H)

Table 25: Geometric characteristics of GMT crash elements

Series (n= 3-4)	Mass m [g]	Length l [mm]	Width w_1 [mm]	Width w_2 [mm]	Thickness t_1 [mm]	Thickness t_2 [mm]	Diameter D_{out} [mm]	Area A [mm^2]
A	206,9	133,9	96,6	11,9	6,4	4,3	64,3	1373,1
B	208,4	133,9	96,5	12,0	6,3	4,2	64,2	1358,7
C	130,2	133,5	96,4	6,9	3,8	3,2	58,4	809,2
D	130,6	135,0	96,7	6,6	3,7	3,1	58,2	791,5
E	195,1	133,3	96,8	11,2	6,0	4,5	62,7	1235,5
F	193,7	134,6	96,4	11,1	5,9	4,4	62,6	1218,5
G	113,4	134,2	95,7	5,7	3,2	3,1	56,7	650,3
H	113,1	133,4	96,2	5,8	3,1	3,1	56,9	673,6
I	247,9	133,7	95,9	13,2	6,8	4,8	64,8	1420,3
J	247,7	133,2	95,9	13,2	6,8	4,6	64,8	1418,3
K	149,9	132,5	95,3	7,3	3,9	3,3	58,6	826,8
L	150,3	133,9	95,4	7,2	3,9	3,3	58,5	821,4

Table 26: Test conditions and measured properties of GMT crash elements

Series (n= 3-4)	Impactor Mass M [kg]	Impact Velocity v_0 [m/s]	Kin. Energy E_{kin} [J]	Max. Displ. l_{max} [mm]	Max Force (SAE 1000) F_{max} [kN]	Mean Force F_m [kN]	Abs. Energy E_{abs} [J]
A	216,3	4,1	1805,9	29,8	80,29	59,44	1729,4
B	86,2	9,4	3796,8	56,0	80,40	64,74	3593,5
C	216,3	4,2	1897,7	45,7	50,60	40,61	1816,7
D	51,8	9,7	2459,3	65,7	45,81	36,97	2397,9
E	216,3	4,6	2278,0	41,6	67,31	54,51	2234,8
F	86,2	9,2	3659,6	70,5	64,04	50,49	3534,9
G	216,3	4,5	2203,0	69,6	39,68	31,04	2130,9
H	51,8	9,1	2141,6	72,7	37,30	29,18	2109,2
I	216,3	4,4	2084,9	31,5	79,48	64,72	1999,6
J	86,2	9,2	3670,8	54,3	78,62	65,77	3543,0
K	216,3	4,4	2099,6	45,1	54,35	44,61	1988,7
L	51,8	9,1	2124,5	49,4	52,59	42,39	2070,0

Table 27: Crash characteristics of GMT crash elements

Specimen series (n = 3-4)			F_m	E_s	σ_s
Notation	Material	v_0 [m/s]	[kN]	[J/g]	[MPa]
A	PP/GF30R	4,1	59.45 ± 3.02	37.70 ± 1.42	43.29 ± 2.20
B	PP/GF30R	9,4	64.74 ± 0.73	41.18 ± 0.89	47.65 ± 0.84
C	PP/GF30R	4,2	40.61 ± 3.11	41.09 ± 3.32	50.20 ± 4.17
D	PP/GF30R	9,7	36.97 ± 2.28	37.91 ± 1.81	46.72 ± 3.10
E	PP/GF30C	4,6	54.51 ± 0.34	36.74 ± 0.01	44.12 ± 0.24
F	PP/GF30C	9,2	50.49 ± 1.18	34.88 ± 1.04	41.45 ± 1.17
G	PP/GF30C	4,5	31.04 ± 2.78	36.44 ± 3.22	47.70 ± 3.49
H	PP/GF30C	9,1	29.18 ± 0.15	34.24 ± 0.82	43.34 ± 1.33
I	PP/GF30C_MF	4,4	64.72 ± 2.15	34.27 ± 0.92	45.57 ± 1.52
J	PP/GF30C_MF	9,2	65.77 ± 1.54	35.08 ± 0.91	46.37 ± 1.09
K	PP/GF30C_MF	4,4	44.61 ± 0.59	39.03 ± 0.38	53.96 ± 0.79
L	PP/GF30C_MF	9,1	42.39 ± 1.73	37.37 ± 1.19	51.66 ± 3.29

8.3 Perforation and impact assemblies

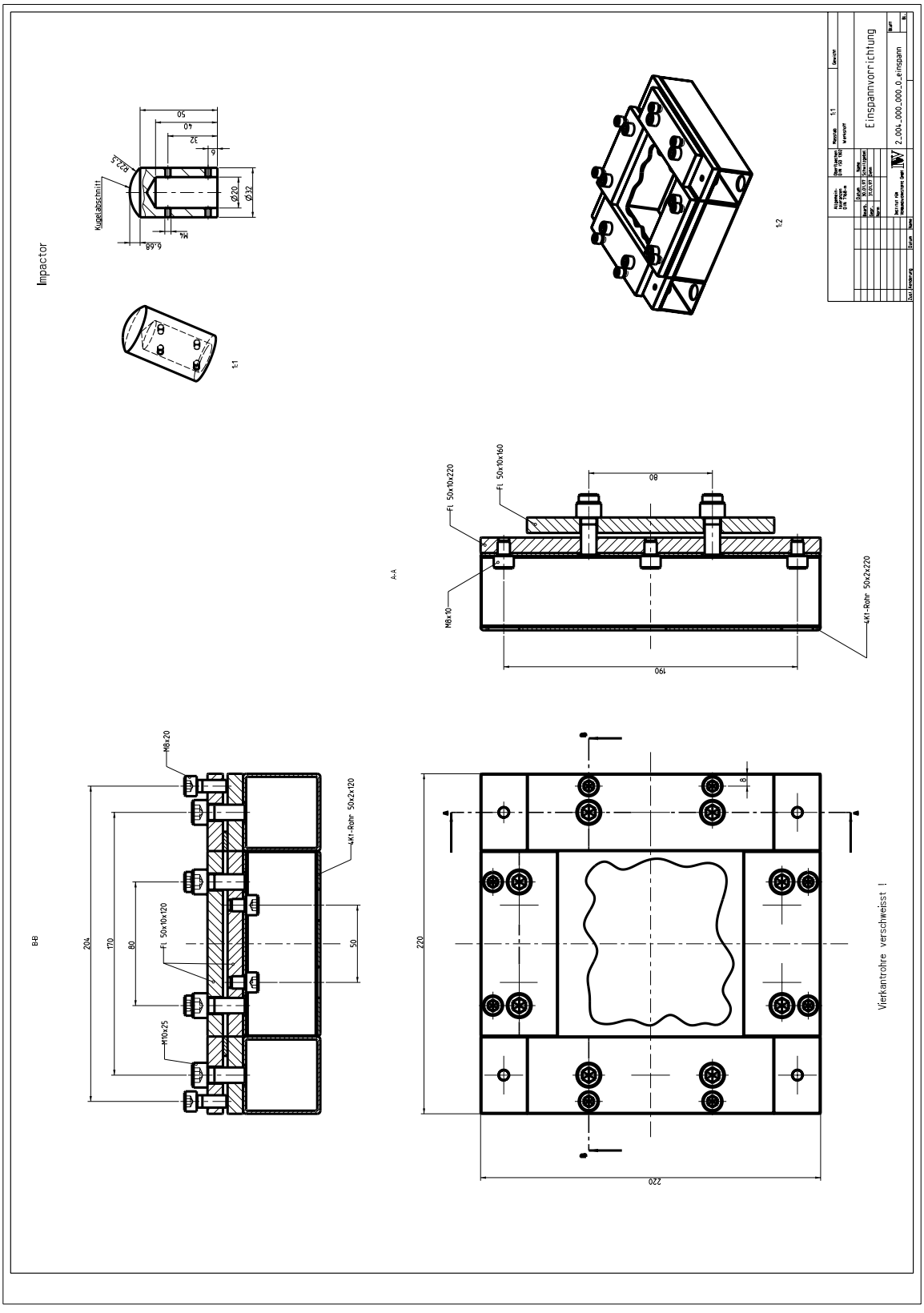

Figure 73: Perforation assembly for flat plate impact tests

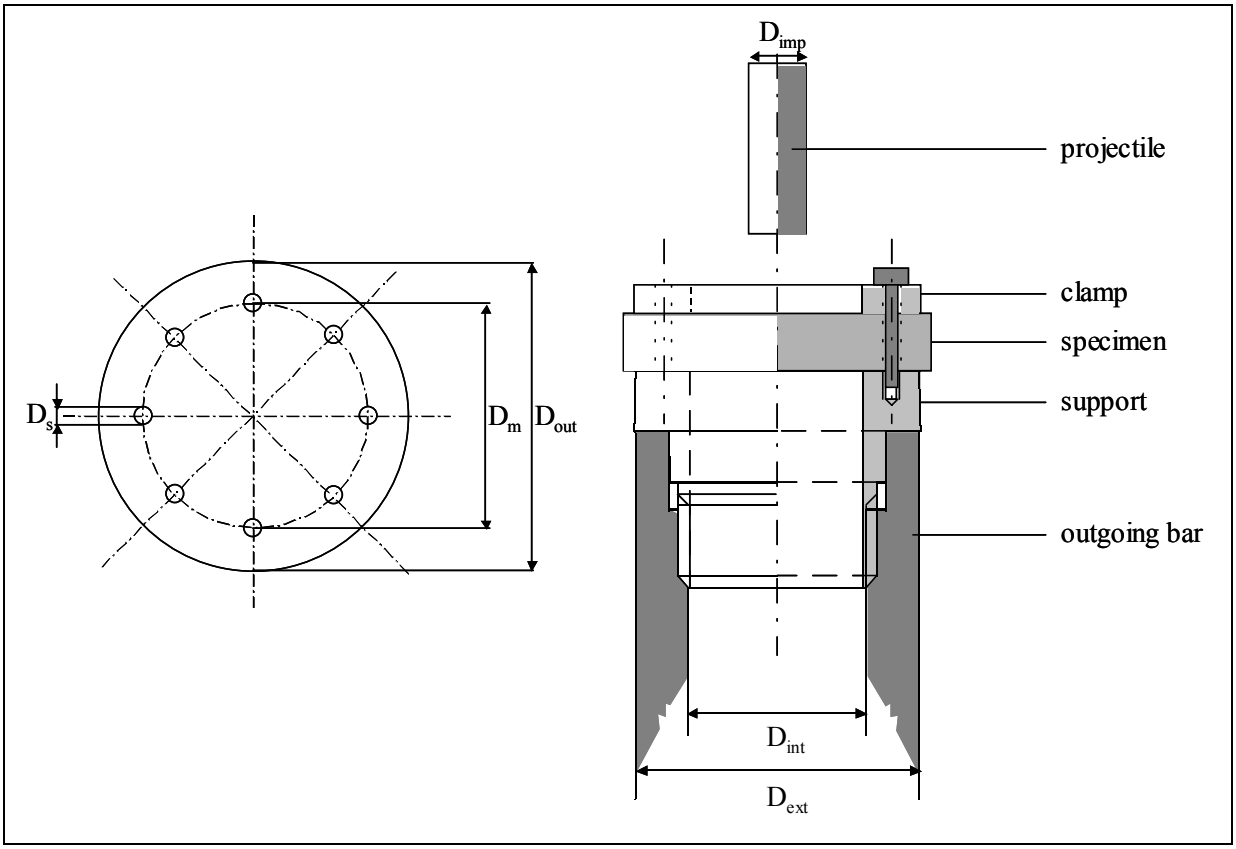

Figure 74: Perforation impact testing with specimen (left) and perforation assembly (right) (D_s = 3.3 mm, D_m = 45 mm, D_{out} = 50 mm, D_{imp} = ∅10 mm, D_{int} = 11 mm or 40 mm)

8.4 Mechanical properties of GF/PET and GMT

Table 28: Elastic and strength constants for knitted GF/PET

Elastic constants:			**Exp. data**	**Isotropic extrapolation**
Prestretching ratio:	λ_w/λ_c	1/1	1.58/0.71	1/1
Loop density ratio:	ρ_w/ρ_c	mm^{-1}/mm^{-1}	0.143/0.2	0.167/0.167
Crystallinity of PET:	K	%	27.5	27.5
Young's modulus:	E_{11}	MPa	20855	15600
	E_{22}	MPa	11694	
Poisson's ratio:	ν_{12}	1	0.389	0.30
	ν_{21}	1	0.227	
Shear modulus:	G_{12}	MPa	5100	6000
Strength constants:				
Tensile strength:	R_{1t}	MPa	222	200
	R_{2t}	MPa	83	
	R_{3t}	MPa	57	
Compressive strength:	R_{1c}	MPa	330	200
	R_{2c}	MPa	251	
Shear strength:	R_{12}	MPa	50	120
	R_{23}	MPa	90	
	R_{31}	MPa	120	
Engineering strain at strength:				
Strain at tensile strength:	$\varepsilon(R_{1t})$	1	0.0175	0.025
	$\varepsilon(R_{2t})$	1	0.020	
Strain at compressive strength:	$\varepsilon(R_{1c})$	1	0.05	
	$\varepsilon(R_{2c})$	1	0.05	
Engineering strain at break:				
Strain at ultimate tension:	ε_{1tu}	1	0.025	0.06
	ε_{2tu}	1	0.030	

Table 29: Elastic and strength constants for GMT

			PP/GF30CMF	PP/GF30C	PP/GF30R
Elastic constants:					
Young's modulus:	E	MPa	7070	4940	5030
Poisson's ratio:	ν	1	0.34	0.34	0.34
Shear modulus:	G	MPa	2638	1843	1877
Strength constants:					
Tensile strength:	R_t	MPa	131	73	70
Compressive strength:	R_c	MPa	141	88	100
Post-comp. strength level:	R_{pc}	MPa	~48	~49	~54
Shear strength:	R_s	MPa	65	36.5	35
Transverse shear strength:	R_{ts}	MPa	45.5	40.5	45.0
Engineering strain at break:					
Strain at ultimate tension:	ε_{tu}	1	0.0265	0.022	0.020

Table 30: Influence of flow direction on anistropy of GMT

	Modulus [MPa]				**Strength [MPa]**				**Glass mat orientation**	
				Mean				Mean	Modulus	Strength
Orientation	0	0/90	90	0/90	0	0/90	90	0/90	0 : 90	0 : 90
PP/GF30C	6340	4940	3080	4710	98	73	44	71	2,1	2,2
PP/GF30R	5460	5030	4170	4815	80	70	52	66	1,3	1,5
PP/GF30CMF	8610	7070	5380	6995	172	131	84	128	1,6	2,0